

The Divergent Evolution of Earth and Venus

Thesis by
Joseph Ghilarducci O'Rourke

In Partial Fulfillment of the Requirements for the
degree of
Doctor of Philosophy

The logo for the California Institute of Technology (Caltech), featuring the word "Caltech" in a bold, orange, sans-serif font.

CALIFORNIA INSTITUTE OF TECHNOLOGY
Pasadena, California

2017
Defended December 1, 2016

© 2017

Joseph Ghilarducci O'Rourke
ORCID: 0000-0002-1180-996X

All rights reserved

ACKNOWLEDGEMENTS

If you need to divert an asteroid, it's best to nuke it while far from Earth. By the same logic, I owe the most gratitude to people who influenced me early on my scientific path. Thanks first and foremost to my parents, William O'Rourke and Teresa Ghilarducci, who indoctrinated me into the signs and shibboleths of academia from an early age. They gave me incredible freedom while gently guiding me to pursue interests that, in retrospect, would best serve me in the long term. Mad props to longtime John Adams High School biology teacher Nevin Longenecker for tapping me to carry on the coveted direct-methanol fuel cell project, along with all the students who joined the competition to get the most Nevin-isms printed in the local newspaper. I am so glad for the years I spent in Boy Scout Troop 555, which taught me self-resilience and the meaning of service leadership (and how to not die in a snowdrift and the rudiments of wilderness pursuit and evasion).

My exemplary experiences in the Department of Geology & Geophysics at Yale University allowed me to apply to graduate school without a second of hesitation. Kanani Lee was an awesome mentor for a hapless but enthusiastic freshman who gave me an exciting, engaging project while making me feel involved in a larger enterprise. She also suggested that I ask a professor named David Stevenson for a summer project after my sophomore year, which turned out to be an excellent idea. Later, I started working with Jun Korenaga, who always impresses me with his blend of creativity and intense rigor. Kanani and Jun have also been very kind to never mention the time I ruined their joint field trip by hitting the wrong thing with a sledgehammer. John Wettlaufer was courageous enough to turn over half his lab to a group of undergraduates planning serious shenanigans. We designed a fluid mechanics experiment that we successfully performed during a parabolic flight out of NASA Johnson Space Center. I literally cannot write enough (my fingers would fall off) to express my appreciation and admiration for everyone involved in this effort and similar campaigns that were a central focus of my undergraduate life.

Too many people to name have improved my time at Caltech. Briefly, I'd like to thank my first generation of officemates (like Da Yang, Meg Rosenburg, and Ke Zhang) for providing an environment conducive to academic progress. Credit goes to the newer additions (Elizabeth Bailey, Nancy Thomas, Siteng Fan, and Ana Lobo) for turning on the lights and making me feel old. Bow down, mortals, to the Captains Planets (Henry Ngo, Danielle Piskorz, Mike Wong, and Pan Lu)—the best

cohort ever. The Caltech/JPL flying club (aka AACIT) has been a huge highlight here—thanks to my instructors and mentors Russell Thomas and David Werntz. Another superlative experience was participating in Joe Kirschvink’s expedition to James Ross Island, Antarctica alongside tons of stellar folks like Jennifer Buz, Sarah Slotznick, and Roger Fu. Speaking of people who put up with me, thanks to the members of Ruddock house for letting me serve as your resident associate for the last few years and to my co-RA, Victoria Chernow. Neither myself nor Coach Sandra Marbut realized that taking a half marathon class would spark an abiding passion for running, but it really did. On that note, thanks to Officer Hernandez of Caltech Security for rescuing me after I blacked out on a training run and also a few weeks later when I drove one of Housing’s carts into a deceptively deep ditch.

Returning to academics, I am thankful for my plethora of collaborators who span myriad projects. I would like to thank David Smith and everyone else at the National Research Council’s Space Studies Board for an amazing internship. I am grateful to Heather Knutson for mentoring me on my first research projects at Caltech and, along with Jennifer Jackson, providing a wide variety of scientific and career advice. Bethany Ehlmann, Suzanne Smrekar, and Louis Moresi have helped me turn a few side projects involving Venus into a real research trajectory. My advisor, David Stevenson, possess creativity, commitment to science, and wide-ranging knowledge that are deservedly legend. Watching people at conferences assume that I am an expert in many fields simply because I am his student is consistently amusing. I feel very fortunate that he let me take on some of his great ideas while also granting me space to pursue various side interests. Additionally, I would like to thank our department’s administrative staff (including Margaret Carlos, Ulrika Terrones, Irma Black, and Bronagh Glaser) who have probably done more for me than I realize. Finally, I beg forgiveness from everyone who I have not mentioned individually. You have influenced me more than you know.

ABSTRACT

Venus and Earth are similar in terms of size and bulk composition, yet their surface conditions are radically different. Earth has hosted plate tectonics and a global magnetic field for billions of years, sustaining water oceans and allowing life to flourish. A thick atmosphere chiefly composed of carbon dioxide, in contrast, drives a greenhouse effect on Venus that would instantly reduce any terrestrial organism to ash. In this thesis, I present several contributions to the debate raging over whether Venus and Earth resembled each other in the past or if unique circumstances placed these celestial siblings on divergent paths from the start. First, I introduce a new process—precipitation of magnesium-rich minerals—that explains the apparent longevity of Earth’s dynamo given plausible assumptions about how the core and mantle lose heat. This mechanism relies on high-temperature equilibration in the aftermath of giant impacts, meaning that Earth’s violent birth enabled its clement present. The lack of a magnetic field thus indicates that Venus escaped savage bombardment or simply that sluggish mantle convection insulates the core. My analyses of the size and spatial distributions of impact craters suggest that volcanism proceeds planet-wide at gradual rates rather than as catastrophic resurfacing events, which supports a uniformitarian view of Venus. Modeling of enigmatic features called coronae on Venus also sheds light on the properties of the crust and lithosphere that yield a stagnant lid rather than plate tectonics. Finally, I present a thermal history for Venus that is consistent with these and other available constraints. Various uncertainties in my models highlight the pressing need to gather more data relevant to Earth’s deep interior and from the most Earth-like planet in our solar system.

PUBLISHED CONTENT AND CONTRIBUTIONS

- O'Rourke, J. G. and J. Korenaga (2015). "Thermal evolution of Venus with argon degassing". *Icarus* 260, pp. 128–140. DOI: 10.1016/j.icarus.2015.07.009. J.G.O. participated in the conception of the project, performed the calculations, and drafted the manuscript.
- O'Rourke, J. G., J. Korenaga, and D. J. Stevenson (2017). "Thermal evolution of Earth with magnesium precipitation in the core". *Earth and Planetary Science Letters* 458, pp. 263–272. DOI: 10.1016/j.epsl.2016.10.057. J.G.O. conceived the project with input from co-authors, performed the calculations, and drafted the manuscript.
- O'Rourke, J. G. and D. J. Stevenson (2016). "Powering Earth's dynamo with magnesium precipitation from the core". *Nature* 529.7586, pp. 387–389. DOI: 10.1038/nature16495. J.G.O. conceived part of the analysis, performed the calculations, and drafted the manuscript.
- O'Rourke, J. G., A. S. Wolf, and B. L. Ehlmann (2014). "Venus: Interpreting the spatial distribution of volcanically modified craters". *Geophysical Research Letters* 41.23, pp. 8252–8260. DOI: 10.1002/2014GL062121. J.G.O. conceived the project with input from co-authors, performed the calculations, and drafted the manuscript.

TABLE OF CONTENTS

Acknowledgements	iii
Abstract	v
Published Content and Contributions	vi
Table of Contents	vii
List of Illustrations	ix
List of Tables	x
Chapter I: Introduction	1
Chapter II: Powering Earth's dynamo with magnesium precipitation from the core	3
2.1 Abstract	3
2.2 Methods and results	3
2.3 Detailed Methods	10
Chapter III: Thermal evolution of Earth with magnesium precipitation in the core	17
3.1 Abstract	17
3.2 Introduction	17
3.3 Theoretical formulation	20
3.4 Results	27
3.5 Discussion	33
3.6 Conclusions	35
Chapter IV: Interpreting the spatial distribution of volcanically modified craters on Venus	37
4.1 Abstract	37
4.2 Introduction	37
4.3 Crater classifications and size-frequency distributions	40
4.4 Quantifying randomness of spatial distributions	42
4.5 Modeling localized, thin flows on Venus	43
4.6 Shield volcanoes and clustering of embayed craters	47
4.7 Discussion	48
4.8 Conclusions	49
Chapter V: Signatures of lithospheric flexure in stereo topography at coronae on Venus	51
5.1 Abstract	51
5.2 Introduction	51
5.3 Methods	54
5.4 Results	60
5.5 Discussion	73
5.6 Conclusions	75
Chapter VI: Thermal evolution of Venus with argon degassing	77

6.1 Abstract	77
6.2 Introduction	77
6.3 Quantifying argon degassing	81
6.4 Theoretical formulation	84
6.5 Numerical models	91
6.6 Results	93
6.7 Discussion	99
6.8 Conclusions	103
Bibliography	104

LIST OF ILLUSTRATIONS

<i>Number</i>	<i>Page</i>
2.1 Composition of Earth's core and mantle immediately after accretion from models of silicate–metal equilibrium	6
2.2 Estimates of mass precipitated from the cooling core	7
2.3 Representative calculation of precipitate composition	8
2.4 Thermochemical evolution of the core for various rates of precipita- tion and entropy production associated with ohmic dissipation	9
2.5 Additional results from models of Earth's core–mantle differentiation	12
2.6 Posterior probability densities for parameters in the two-stage model of Earth's core–mantle differentiation	13
3.1 Cartoon of Earth's thermal structure assumed in these simulations . .	21
3.2 Representative simulation of the thermal evolution of Earth	28
3.3 Entropy production for various precipitation rates	29
3.4 Influence of the mantle cooling rate	30
3.5 Sensitivity tests for various parameters	31
4.1 Map of impact craters on Venus	41
4.2 Statistical analysis of the spatial distribution of various populations of impact craters	43
4.3 Simplified models of volcanic resurfacing events	46
5.1 Study area with stereo topography	54
5.2 Representative images of coronae	62
5.3 Representative topographic profiles and best-fit models	63
5.4 Topographic profiles with GTDR data	66
5.5 Mechanical thicknesses and surface heat flows for all coronae	70
5.6 Elastic thickness versus diameter and classification	72
6.1 Amount of argon-40 outgassing from Venus	83
6.2 Cartoon of Venus' thermal structure assumed in these simulations . .	85
6.3 Representative simulation of the thermal evolution of Venus	94
6.4 Sensitivity analyses for the thermal evolution of Venus	96

LIST OF TABLES

<i>Number</i>		<i>Page</i>
2.1	Parameters with uncertainties used in models of Earth's differentiation	11
3.1	Parameters tracked during simulations of Earth's thermal evolution . . .	22
3.2	Constants held fixed in simulations of Earth's thermal evolution . . .	22
5.1	Best-fit parameters from Cartesian and axisymmetric flexure models .	61
5.2	Occurrence rates of flexure in various sub-groups	68
5.3	Properties of every coronae with flexure	69
6.1	Parameters used in models of Venus' thermal evolution	92
6.2	Principal component analysis of simulation output	99

Chapter 1

INTRODUCTION

Since time immemorial, people have heralded Venus as the morning star. Although scientists are generally fond of Latin terms, the properly translated “Lucifer” has fallen rather far out of favor. Anyone seeking public support for expensive missions of celestial exploration should probably avoid accusations of devil-worship. Association with the adversary from modern Christian tradition is undeniably apt, however, as no rocky planet in our solar system has a surface so hellish. Despite receiving roughly four times less solar insolation than Mercury, the closest planet to the Sun, surface temperatures on Venus are more than three hundred kelvin hotter on average because of the greenhouse effect produced by its thick, carbon dioxide atmosphere. No water-based creature could survive, and even humanity’s hardest spacecraft only transmit from the surface for a few hours before perishing. At present, it is unknown when and why the evolution of Venus and Earth diverged. Life emerged on Earth shortly after its accretion—perhaps Venus once inhabited a state of grace as well. Our ignorance about these twin worlds belies any claim of understanding the general factors that govern the habitability of rocky planets.

In my thesis, I tell stories compatible with available observations that explain the most glaring differences between Venus and Earth. For instance, the rock record reveals that Earth’s global magnetic field has persisted for over 3.4 billion years, driven by vigorous convection in outer, liquid portion of the iron-rich core. But no comparable magnetism has ever been detected at Venus. Simple theory elucidates why dynamos are perhaps rare within terrestrial planets but ubiquitous within gas and ice giant planets and stars. That is, thermal conduction in iron alloys is borderline capable of accommodating the estimated heat flows out of their cores without provoking conductive fluid motions. Over the past several years, theoretical calculations and experiments at appropriately extreme conditions revised estimates of the thermal conductivity of Earth’s core (and thus the putative core of Venus) sharply upwards. This implies that the rate at which the core is currently losing heat to the mantle, estimated with seismology and mineral physics, would not drive convection absent a source of chemical buoyancy. At present, the release of light elements like oxygen and silicon from the inner core suffices, but the age of the inner core is estimated as billions of years less than the global magnetic field.

Chapter 2 introduces the idea that the precipitation of magnesium-rich minerals may serve as an alternate source of chemical buoyancy to drive convection in early epochs. Conventional models assume negligible magnesium content in the core based on the low solubility of magnesium in iron at ambient conditions. But previously published theory and later experiments in diamond-anvil cells suggest that a few weight percent of magnesium may partition into the core in the high-temperature aftermath of giant impacts like the one that presumably formed the Moon. Subsequent cooling quickly saturates the core in magnesium and other light elements, causing precipitation that releases a huge amount of gravitational energy. Thermal modeling in Chapter 3 shows in detail that sufficient entropy production is available for the dynamo even if cooling rates are not much different in the past than at present. Additionally, the nucleation of the inner core may not produce a dramatic increase in field intensity as preserved in paleomagnetic samples.

In the following chapters, I turn to the question of how Venus loses heat absent plate tectonics. Sluggish cooling could kill a dynamo even if Venus also suffered giant impacts and thus partitioned a comparable inventory of magnesium into its core. High rates of heat loss, in contrast, would provide evidence that the cores of Venus and Earth have different compositions and/or structures, thus proving that the formation of these celestial cousins involved fundamentally distinct processes. Ultimately, planetary magnetic fields are chaotic, non-linear phenomena worthy of study in their own right. But their impact on issues that are removed from Maxwell's equations at first glance remains my primary interest. Information about the internal structure of Venus is utterly absent at present, so I focus for now on how the mantle is losing heat to the surface.

Chapters 4 and 5 both rely on interpretations of a newly available dataset containing stereo topography for $\sim 20\%$ of the surface. Previous work claimed that post-impact volcanism has modified many more impact craters than commonly believed. My analyses indicate that their size and spatial distributions are most consistent with localized volcanism occurring at gradual rates, militating against supposed catastrophic resurfacing. Low values of elastic thickness at coronae on Venus imply that heat flows are anomalously high at these features or perhaps the rheology of the lithosphere is different than the common assumptions appropriate to dry diabase. Likewise, thermal evolution models in Chapter 6 demonstrate that continuous evolution in the stagnant-lid regime of mantle convection is also consistent with the constraints on crustal chemistry and atmospheric abundance of argon-40.

*Chapter 2***POWERING EARTH'S DYNAMO WITH MAGNESIUM
PRECIPITATION FROM THE CORE****2.1 Abstract**

Earth's global magnetic field arises from vigorous convection within the liquid outer core. Palaeomagnetic evidence reveals that the geodynamo has operated for at least 3.4 billion years (Tarduno, Cottrell, Watkeys, et al., 2010), which places constraints on Earth's formation and evolution. Available power sources in standard models include compositional convection (driven by the solidifying inner core's expulsion of light elements), thermal convection (from slow cooling), and perhaps heat from the decay of radioactive isotopes. However, recent first-principles calculations (Koker et al., 2012; Pozzo et al., 2012) and diamond-anvil cell experiments (Gomi et al., 2013; Seagle et al., 2013) indicate that the thermal conductivity of iron is two or three times larger than typically assumed in these models. This presents a problem: a large increase in the conductive heat flux along the adiabat (due to the higher conductivity of iron) implies that the inner core is young (less than one billion years old), but thermal convection and radiogenic heating alone may not have been able to sustain the geodynamo during earlier epochs (Gomi et al., 2013). Here we show that the precipitation of magnesium-bearing minerals from the core could have served as an alternative power source. Equilibration at high temperatures in the aftermath of giant impacts allows a small amount of magnesium (one or two weight per cent) to partition into the core while still producing the observed abundances of siderophile elements in the mantle and avoiding an excess of silicon and oxygen in the core. The transport of magnesium as oxide or silicate from the cooling core to underneath the mantle is an order of magnitude more efficient per unit mass as a source of buoyancy than inner-core growth. We therefore conclude that Earth's dynamo would survive throughout geologic time (from at least 3.4 billion years ago to the present) even if core radiogenic heating were minimal and core cooling were slow.

2.2 Methods and results

Earth differentiated into a silicate mantle and an iron-rich core during its formation in the approximately 100 million years following the initial collapse of the solar nebula. Scores of collisions between planetary embryos ranging from Moon- to

Mars-sized accompanied by an influx of smaller planetesimals characterized the last stage of accretion (Chambers, 2004; Oghihara et al., 2007). In one view of core formation, impacting embryos disaggregate in a deep magma ocean that overlies a mostly solid region (Wade and Wood, 2005; Wood et al., 2006; Rubie, Frost, et al., 2011; Siebert et al., 2013; Rubie, Jacobson, et al., 2015). Metal sinks into a pond at the base of the magma ocean and equilibrates at the ambient pressure and temperature near the peridotite liquidus. As a consequence, the mantle becomes depleted in siderophile elements. Metallic diapirs quickly sink to the core–mantle boundary (CMB) without further equilibration, although percolation through the lower mantle has also been suggested (Shi et al., 2013). One issue with this view is that the concentration of light elements in core material should increase over time as pressure and temperature increase. Without vigorous mixing, a stable compositional stratification would develop below the CMB (Helfrich, 2014), which could prevent the initialization of a convective dynamo. The Moon-forming giant impact and possibly earlier, less energetic ones may recover the homogeneity of the core. Giant impacts are also important because they can heat parts of Earth to around 10,000 K, possibly even causing complete melting (Canup, 2008; Canup, 2012; Āuk and Stewart, 2012). Portions of the cores of large impactors should emulsify down to short (centimetres) length scales in the superheated mantle (Dahl and Stevenson, 2010), permitting some metal–silicate equilibration at temperatures far above the peridotite liquidus.

The density of the core today, inferred from seismology, is about 10% less than the expected value for a pure iron/nickel (Fe/Ni) alloy at the high temperatures and pressures of Earth’s deep interior (Poirier, 1994). Identifying the light element(s) responsible for this deficit has remained a central problem for decades. Despite being the fourth most abundant element in Earth by mass, magnesium (Mg) has been correctly rejected as a major contributor to the density deficit of the core in favour of elements like S, Si, O, C, and H, since Mg (as an oxide or silicate) and metallic Fe are almost immiscible under ambient conditions (Poirier, 1994).

However, the complete absence of Mg from the core is a thermodynamic impossibility because of entropic effects. New first-principles calculations indicate that the saturation limit of MgO in Fe is below 0.1 mol% at 3,000 K and 50 GPa, but reaches 1 mol% at 4,200 K and increases rapidly thereafter (Wahl and Militzer, 2015). Partitioning studies in diamond- anvil cells likewise indicate that Mg is not present above the detection limit after equilibration below 3,000 K. But Mg abun-

dances approaching 1 mol% are observed in experiments reaching 3,000 K to 5,000 K (Takafuji et al., 2005; Fischer et al., 2015). Spurious signals from the surrounding silicate are a complicating factor in these experiments, given the small sample sizes (Fischer et al., 2015). Still, all available data are consistent with the solubility of Mg in the Fe-rich metal exhibiting an exponential (Arrhenius) dependence on temperature. The low solubility also necessarily implies a strong dependence of that solubility on temperature.

Here we demonstrate that the composition of the mantle is consistent with core–mantle differentiation partially occurring at temperatures that permit substantial Mg partitioning. We consider two simple models of Earth’s accretion, assuming that Earth is comprised of 12 major (Fe, Si, and O), lithophile (Mg, Al, and Ca), and siderophile (Ni, Co, Cr, V, Nb, and Ta) elements. First, we test a conventional, single-stage model with equilibration temperatures near the peridotite liquidus at mid-mantle depths. Second, we develop a two-stage model with some material equilibrating at temperatures above 5,000 K. To calculate the composition of Earth’s core and mantle, we adopt parameterizations of partition coefficients (the metal-to-silicate ratio of elemental concentrations) as functions of pressure, temperature, and bulk composition from the most recent and comprehensive data sets (Rubie, Jacobson, et al., 2015; Fischer et al., 2015). We compare the predictions of our models to the estimated composition of the primitive mantle and the core mass fraction (Palme and O’Neill, 2013).

A Markov chain Monte Carlo analysis quantifies the distribution of model parameters that match the available data. This technique explores the effects of varying all variables within their plausible uncertainties, with tens of orders of magnitude more computational efficiency than a simple grid search of the high-dimensional parameter space. The median chi-squared values are 8.3 and 8.6 for the single- and two-stage models, respectively, indicating that both models can provide good fits to the data. Figure 2.1 shows that our two-stage model reproduces the observed elemental abundances in the primitive mantle. That is, the peaks of the probability density functions are all within 0.83σ of the estimated mean values. The median result of this model is that ~ 5 wt% of Earth equilibrates at $\sim 6,000$ K, although the equilibration of up to ~ 20 wt% at 8,000 K is permissible if other parameters are suitably adjusted. Mirroring previous studies, our single-stage model suggests a best-fit equilibration pressure of 57 ± 9 GPa, corresponding to $3,500 \pm 250$ K. Without partial equilibration at higher temperatures, less than 0.5 wt% Mg is

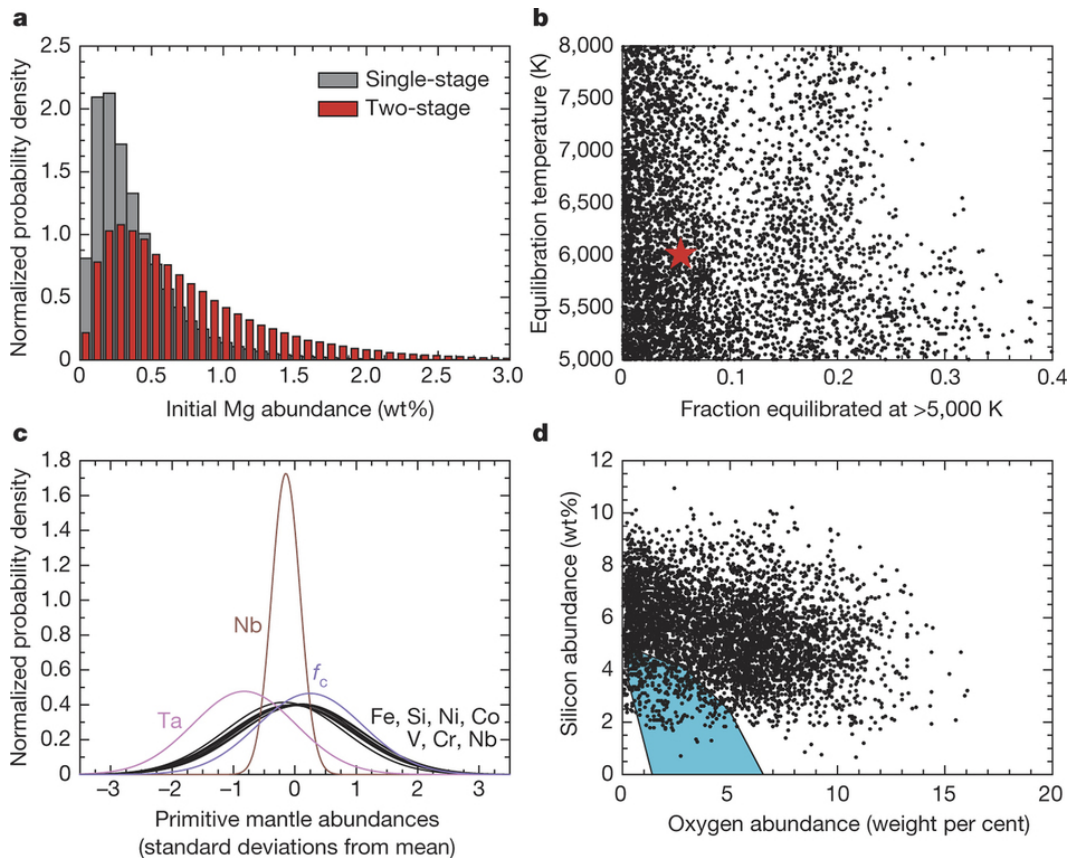


Figure 2.1: a, Initial abundance of Mg in the core from both models. b–d, From the two-stage model: fraction of material (red star is the mean result) equilibrated in the aftermath of giant impacts (b), posterior probability densities for elemental abundances in the primitive mantle (Palme and O’Neill, 2013) and the core mass fraction, f_c (c), and the initial abundances of Si and O in the core compared to those permitted (blue region) by present-day seismological observations (Badro, Côté, et al., 2014) (d). Black dots are random draws from the posterior distributions.

expected to enter the core. The two-stage model, however, permits initial Mg abundances ranging from ~ 0.5 wt% to 2 wt%.

Other light elements also enter the core as temperatures of equilibration increase. Figure 2.1 illustrates that siderophile elements alone do not tightly constrain the initial abundances of Si and O in the core, especially since calculating partitioning behaviour above 5,000 K necessitates extrapolating the available experimental data (Fischer et al., 2015). Some two-stage simulations yield compositions within the 1σ range of estimated values for the present-day core based on seismology and mineral physics (Badro, Côté, et al., 2014). But our models seem to ‘prefer’ slightly higher initial abundances of light elements. Precipitation caused by rapidly decreasing Mg

solubility in the cooling core can lower the abundances of Si and, especially, O to their modern values.

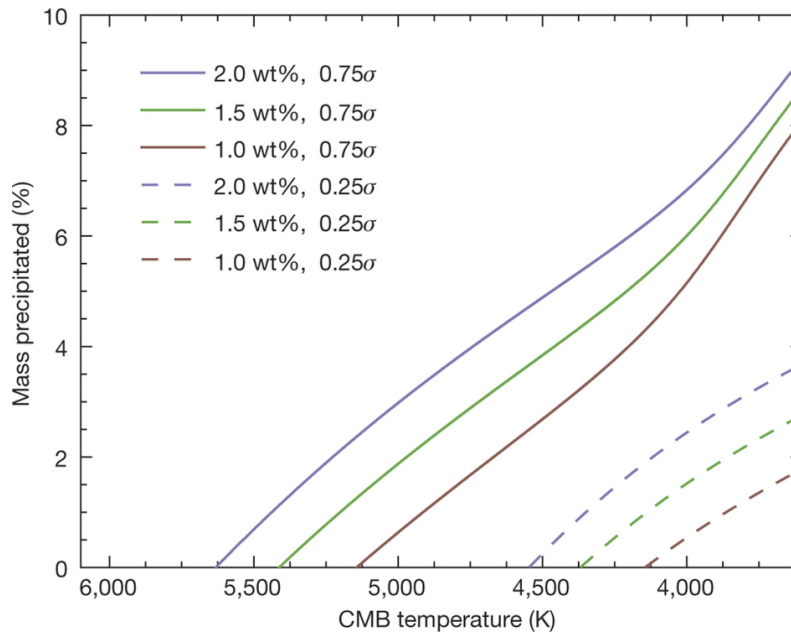


Figure 2.2: The colours denote initial Mg abundances, while solid and dashed lines represent calculations with the constants a_O , b_O , and c_O used to calculate O solubility (K_O) decreased by different fractions of a standard deviation.

Figure 2.2 shows representative calculations of the precipitation of Mg-bearing silicates and oxides from Earth's core. Here we assume that the core initially contained 3 wt% Si and 6 wt% O. We find that the amount of mass precipitated as a function of temperature is a sensitive function of the solubility of O, along with the expected dependence on the initial Mg abundance. Using the mean exchange coefficient for Mg, at least 1 wt% Mg is required for precipitation to begin above 4,000 K. Alternatively, the constants used to calculate the exchange coefficient for O could be decreased by more than 0.25σ from their estimated mean values. Figure 2.3 illustrates one example of the evolving composition of the precipitate. The solubility of Mg is below that of Si and O, so it comprises almost half the precipitate by number despite having the lowest abundance. The precipitate becomes more Si-rich as Mg is depleted, whereas the Fe content remains roughly constant. Overall, $\sim 0.5\%$ of the initial mass precipitates per 100 K of cooling once precipitation begins.

Transporting precipitated material to the CMB from a mostly well-mixed outer core releases more gravitational energy per unit mass than inner-core growth. Large-scale vertical motions are necessary to maintain the dynamo, meaning that either thermal

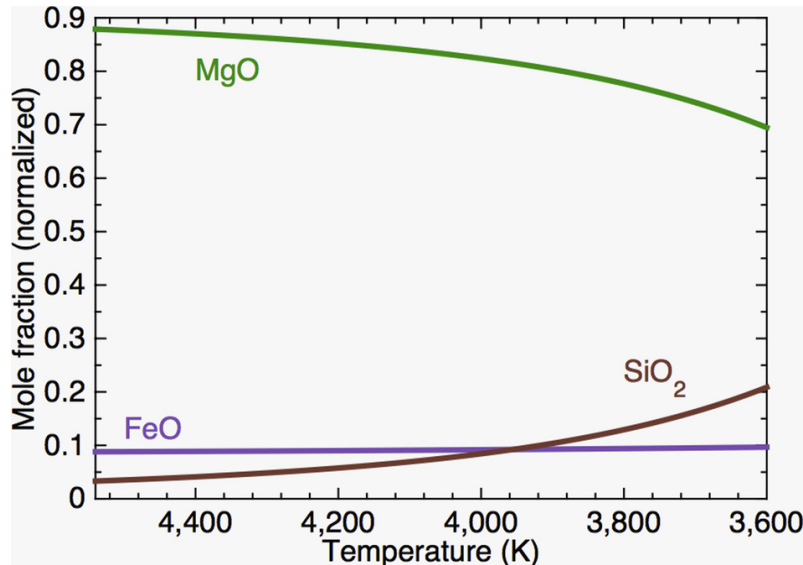


Figure 2.3: Here the core initially contains 2 wt% Mg, 3 wt% Si and 6 wt% O. Additionally, the constants a_0 , b_0 and c_0 are each reduced by 0.25σ from their estimated mean values. The actual mineralogy of the precipitate (for example, the amount and composition of perovskite) is not modelled in detail.

or compositional effects must provide enough buoyancy to keep the temperature profile in the liquid outer core close to the adiabat in the region of dynamo generation (Stevenson, 2003; Nimmo, 2015). Crucially, the density difference between the precipitate and the outer core is approximately ten times the contrast between the inner and outer core attributable to composition (roughly half of the $\sim 5\%$ total). This means that precipitating a layer of Mg-bearing material with a thickness of only ~ 10 km above the CMB is energetically equivalent to crystallizing the entire inner core. We incorporate Mg precipitation into comprehensive models of the energetics of the core to explore its importance further.

Figure 2.4 presents several calculations for the thermochemical evolution of the core. We iterate the equations of global energy and entropy balance backwards in time from present-day conditions (Nimmo, 2015). Given a fixed amount of entropy production, we calculate the CMB heat flow and cooling rate necessary to sustain the dynamo. We use the recently revised value of core thermal conductivity, despite a new study (Zhang et al., 2015) that militates against the emerging theoretical and experimental consensus (Koker et al., 2012; Pozzo et al., 2012; Gomi et al., 2013; Seagle et al., 2013). If there is no Mg precipitation, an entropy production rate of 500 MW K^{-1} (corresponding to $\sim 2.5 \text{ TW}$ of ohmic dissipation) implies initial CMB temperatures of $\sim 7,000 \text{ K}$ and a core-to-mantle heat flow of 40 TW to 70 TW

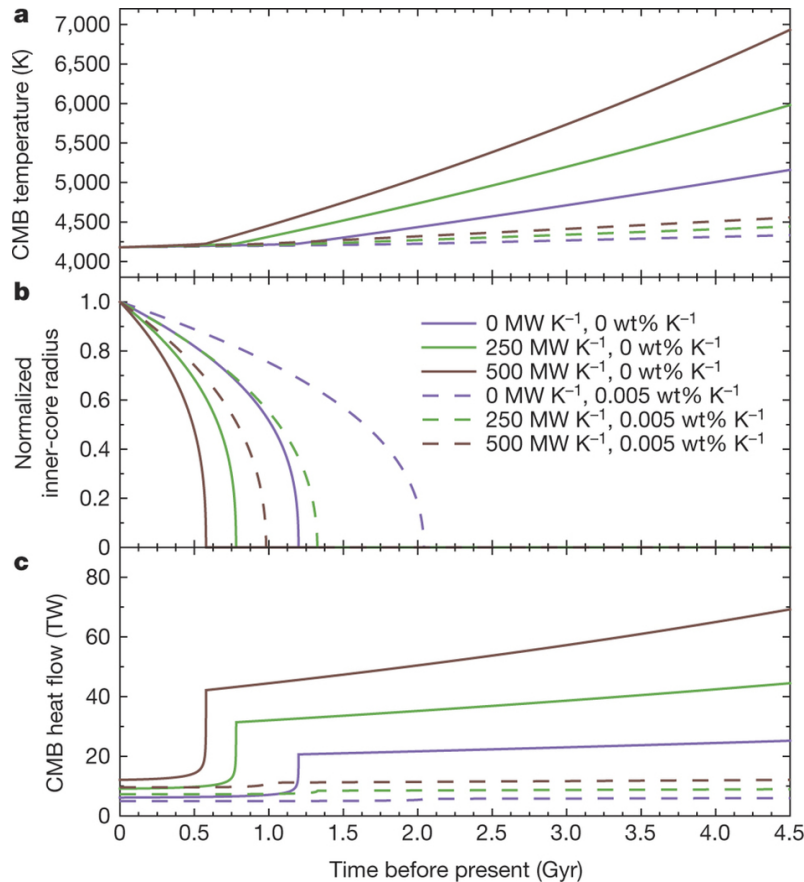


Figure 2.4: Assuming that the core always produces a constant amount of entropy required to sustain the dynamo, we calculate the implied CMB temperature (a), inner-core radius relative to the present (b), and CMB heat flow (c). Gyr, billion years.

before inner-core nucleation at ~ 0.6 billion years ago. Incorporating the plausible precipitation rate lowers the necessary amount of secular cooling to only ~ 300 K over 4.5 billion years. A core heat flow close to the present-day value (< 20 TW) is thus sufficient to power a dynamo for Earth's entire history.

Precipitation of Mg from the core has profound implications for the evolution of Earth's deep interior. Most importantly, it eliminates the need to invoke a geochemically dubious magnitude of radiogenic heating (Corgne et al., 2007) or enhanced heat flux across the CMB into a basal magma ocean (Labrosse, Hernlund, et al., 2007). High thermal conductivity and slow core cooling are consistent with inner-core nucleation in the Mesoproterozoic (Biggin, Piispa, et al., 2015). Models that include only the inner core as a source of compositional buoyancy predict that stable layers hundreds of kilometres thick should develop near the CMB (Pozzo

et al., 2012), which may be disrupted by precipitation. However, precipitation may actually occur at depth if the solubility of Mg is strongly pressure dependent. The real situation is even more complicated if the CMB is undersaturated in Si and O, meaning that material from the mantle tends to dissolve in the core. Elemental transport in both directions is potentially permissible because the Mg-rich precipitate differs in composition from the CMB. The effect of giant impacts on core formation should motivate additional experiments on metal–silicate partitioning at temperatures above 5,000 K. Non-standard evolutionary scenarios featuring precipitation are perhaps applicable to the cores of other terrestrial planets.

2.3 Detailed Methods

Element partitioning

For an element M besides oxygen with valence n , the partition coefficient is defined as $D_M = X_M^{met} / X_{MO_{n/2}}^{sil}$, where X_M^{met} is the mole fraction of the element M in metal and $X_{MO_{n/2}}^{sil}$ is the mole fraction of the corresponding oxide $MO_{n/2}$ in the silicate (Fischer et al., 2015). The associated exchange coefficient is $K_M = D_M / D_{Fe}^{n/2}$. For oxygen, $K_O = X_{Fe}^{met} X_O^{met} / X_{FeO}^{sil}$. Using experimental data, the exchange coefficients K_M may be parameterized as follows (Fischer et al., 2015):

$$\begin{aligned} \log_{10} K_M &= a_M + \frac{b_M}{T} + \frac{c_M P}{T} + \frac{\epsilon_M^M \ln(1 - X_M)}{2.303} \\ &+ \frac{1}{2.303} \sum_{\substack{k=1 \\ k \neq i}}^N \epsilon_k^i X_k \left(1 + \frac{\ln(1 - X_k)}{X_k} - \frac{1}{1 - X_i} \right) \\ &- \frac{1}{2.303} \sum_{\substack{k=1 \\ k \neq i}}^N \epsilon_k^i X_k^2 X_i \left(\frac{1}{1 - X_i} + \frac{1}{1 - X_k} - \frac{X_i}{2(1 - X_i)^2} - 1 \right), \quad (2.1) \end{aligned}$$

where P is pressure, and a_M , b_M and c_M are constants. Each ϵ_j^i is the interaction parameter of elements i and j in the liquid at temperature T , which is a function of the reference interaction parameter e_j^i determined at a reference temperature of 1,873 K. These compositional parameters are necessary to fit partitioning data for V and Cr, but are typically set to zero for other siderophile elements (Fischer et al., 2015).

We estimate a_{Mg} and b_{Mg} using experimental results from Takafuji et al. (2005) and assuming that 0.05 wt% of Mg (below the detection limit) was present in quenched liquid iron at 2,500 K. Our derived values are in agreement with theoretical predictions (Wahl and Militzer, 2015) and preliminary results from diamond-anvil

cell experiments at higher temperatures (Nomura et al., 2012). We adopt formal errors (100% and 9%, respectively) for these parameters a_{Mg} and b_{Mg} , which are comparable in magnitude to those for other elements (Fischer et al., 2015). We assume here that $c_{Mg} = 0$ and that interaction effects are negligible, although future experiments may reveal that these factors actually are important.

i	Bulk Earth	σ	Primitive Mantle	σ	Units	n	a_i	σ	b_i	σ	c_i	σ
Fe	31.9	1.3	6.3	0.063	wt%							
Ca	1.71	0.10	2.61	0.21	wt%							
Al	1.59	0.10	2.38	0.19	wt%							
Mg	15.4	0.62	22.17	0.22	wt%	2	0.1	0.1	-10,851	1,000		
Si	16.1	0.48	21.22	0.21	wt%	4	1.3	0.3	-13,500	900		
Ni	1.82	0.13	0.186	0.009	wt%	2	0.46	0.16	2,700	300	-61	6
Co	880	35	102	5.1	ppm	2	0.36	0.15	1,500	300	-33	5
Nb	0.44	0.044	0.595	0.119	ppm	5	2.66	0.11	-14,032		-199	16
Ta	0.025	0.003	0.043	0.002	ppm	5	0.84	0.09	-13,806		-115	13
V	105	6.3	86	4.3	ppm	3	-1.5	0.3	-2,300	700	9	9
Cr	4,700	235	2,520	252	ppm	2	-0.3	0.2	-2,200	600	-5	7

Table 2.1: The table shows the oxygen-free composition of bulk Earth (Palme and O’Neill, 2013), elemental abundances in the primitive mantle (McDonough, 2001), and constants a_i , b_i , and c_i used to model partitioning behaviour (Rubie, Jacobson, et al., 2015; Fischer et al., 2015). For O, $a = 0.6 \pm 0.4$, $b = -3,800 \pm 900$, and $c = 22 \pm 14$. Likewise, $e_O^V = -0.077 \pm 0.008$, $e_{Si}^V = 0.039 \pm 0.014$, and $e_O^{Cr} = -0.037 \pm 0.007$, which are used to calculate temperature-dependent interaction parameters as described in Fischer et al. (2015).

Equations for the exchange coefficients and mass balance allow us to solve for the composition of the metal and silicate phases for any initial bulk composition, given the temperature and pressure of equilibration. Methods for solving these equations are detailed by Rubie, Frost, et al. (2011) and Rubie, Jacobson, et al. (2015) and others (Siebert et al., 2013; Fischer et al., 2015). Since the valences of elements in the silicates are specified, oxygen fugacity is not a free parameter. Table 2.1 lists experimentally determined values for all constants in our models, along with their formal errors.

Core formation

We consider two simple scenarios for Earth’s accretion and differentiation. Both models have 37 parameters with quantified uncertainties corresponding to the oxygen-free composition of bulk Earth³² and the constants used to calculate partitioning behaviour (Rubie, Jacobson, et al., 2015; Fischer et al., 2015). Our single-stage model has two additional parameters: P_1 , the pressure at equilibration,

and $[\text{Fe}/\text{O}]_1$, the ratio of the molar abundances of iron and oxygen in bulk Earth. In this case, we assume that equilibration occurs at the base of a magma ocean with temperature on the peridotite liquidus. In our two-stage model, we permit a fraction of Earth to equilibrate at T_2 between 5,000 K and 8,000 K, which is hotter than the peridotite liquidus at the CMB. This material may equilibrate at a different pressure, P_2 , and can also have a different bulk oxygen content, $[\text{Fe}/\text{O}]_2$. We restrict P_1 and P_2 between 0 GPa and 135 GPa with equal prior probability throughout this range. Likewise, we allow $0.25 < [\text{Fe}/\text{O}]_1 < 0.65$ and $0.25 < [\text{Fe}/\text{O}]_2 < 0.6$, representing a range of oxidizing and reducing conditions. For reference, the best-fit $[\text{Fe}/\text{O}]_1 = 0.52 \pm 0.02$ in the single-stage model. We aim to reproduce ten data points: the estimated abundances of Fe, Si, Ni, Co, V, Cr, Nb, and Ta in the primitive mantle, along with the ratio Nb/Ta (14.0 ± 0.3) and the core mass fraction, f_c (0.32 ± 0.01).

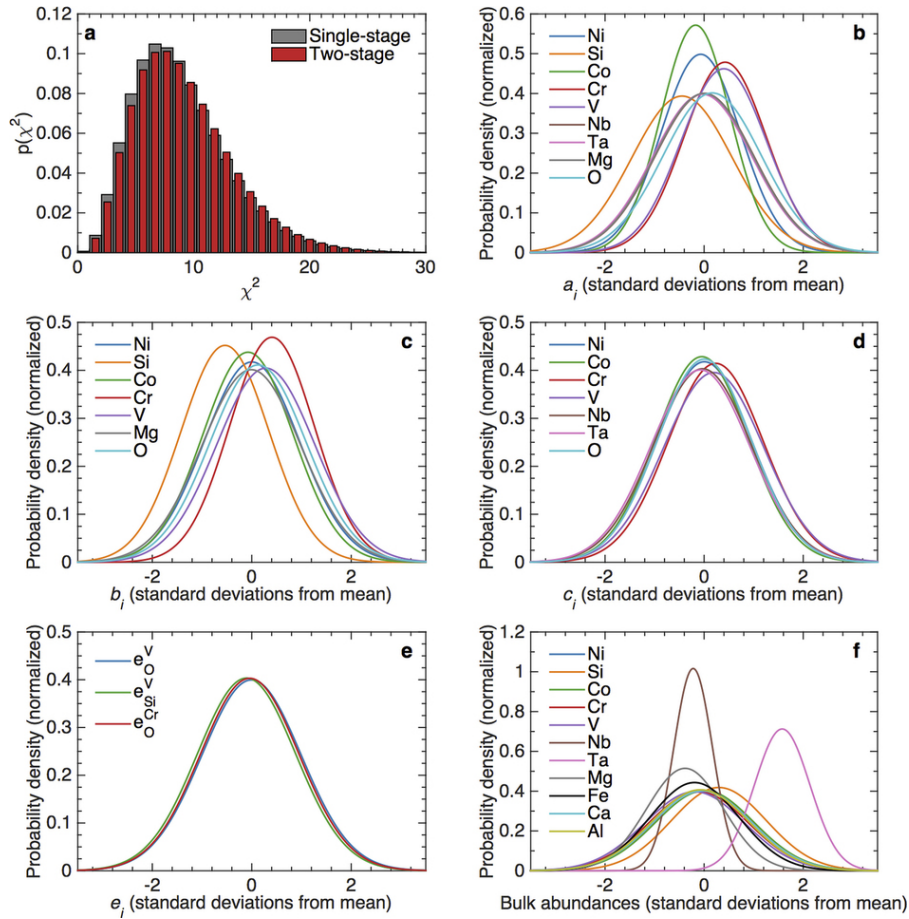


Figure 2.5: Normalized distributions of chi-squared values, $p(\chi^2)$, for both models of core formation (a), along with posterior probability densities for the coefficients a_i , b_i , c_i , and e_j^i for various elements i and j used in the two-stage model to calculate partitioning behaviour (b–e) and elemental abundances in bulk Earth (f).

Given the high dimensionality of our models, a comprehensive grid search is computationally prohibitive. The Markov chain Monte Carlo technique, however, samples only each point in the parameter space that has a frequency equal to the posterior probability at that point. We use the standard Metropolis–Hastings sampling (Chib and Greenberg, 1995). Briefly, we begin with an initial guess for the model parameters, N_x . To decide whether to add another set of model parameters, N_{x+1} , to the chain, we compute the likelihood and prior probability. The posterior probability, $p(N_x)$, is proportional to the multiple of the likelihood and the prior. The likelihood is proportional to the conventional chi-squared value computed from the difference between the model output and the data. The prior is determined from experimental constraints. For example, a model that sets all constants used to calculate partitioning behaviour equal to their mean estimated values has a higher prior than a model where a few constants are increased or decreased by a fraction of a standard deviation. However, the second model may have a substantially higher likelihood and thus posterior. The algorithm always accepts new sets if $p(N_{x+1}) \geq p(N_x)$. Critically, new sets with lower posteriors are sometimes accepted with probability $p(N_{x+1})/p(N_x)$.

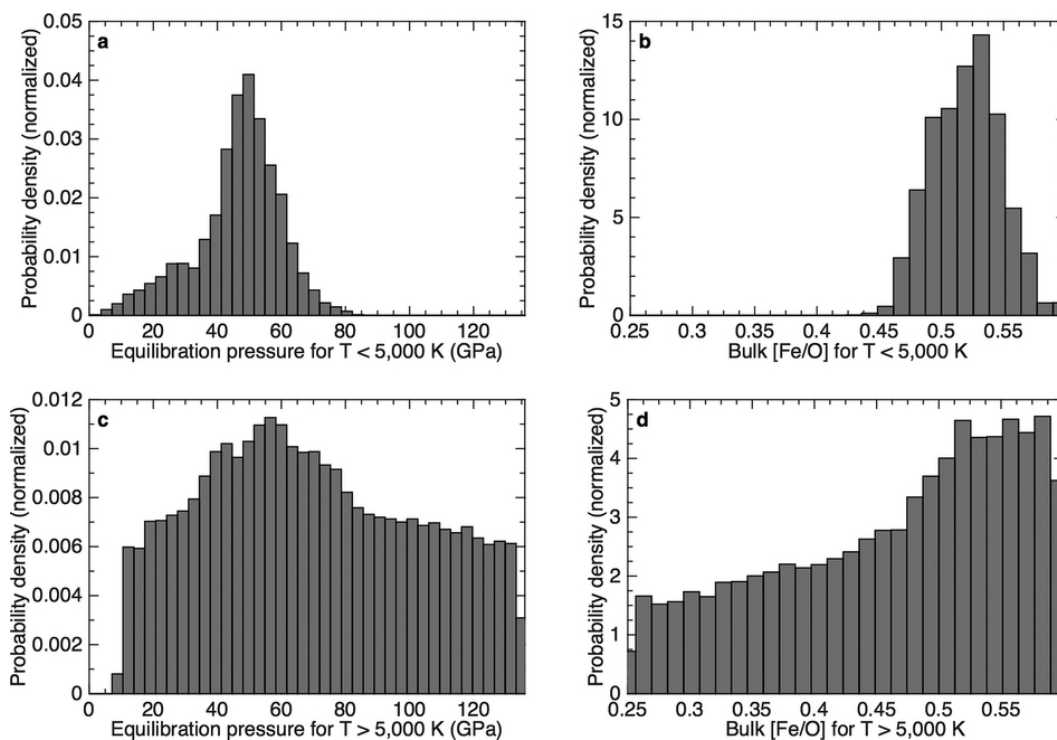


Figure 2.6: Posterior probability densities for parameters in the two-stage model of Earth's core–mantle differentiation

The generation functions that we used to guess N_{x+1} are tuned to produce an overall acceptance rate of $\sim 25\%$ to 75% . We report results from Markov chains with 1.66×10^6 and 2.71×10^6 accepted links for the single- and two-stage models, respectively. Visual inspection of the output traces reveals that these chains have converged, meaning that each Markov chain is equivalent to a long series of random draws from the real posterior distributions. To remove any dependence on our initial guess of model parameters, we remove all links before the likelihood first dips below its eventual median. Only 434 and 445 links were deleted from the Markov chains for the single- and two-stage models, respectively. Figure 2.5 shows the distributions of chi-squared values for both models, along with the posterior distributions for Earth's bulk composition and constants governing partitioning behaviour. As desired, posteriors for these parameters are basically equal to the priors. The posterior for the bulk abundance of Ta peaks 1.58 standard deviations away from the estimated mean, but values within 1σ remain quite plausible. Figure 2.6 contains the posterior probability distributions for other parameters in the two-stage model.

Magnesium precipitation

We constructed a simple model for the precipitation of Mg-rich silicates and oxides. The output of this calculation is the mass of precipitate associated with a given amount of cooling, which is an essential parameter in the complete thermochemical model detailed below. At a given temperature, a condition for silicates and oxides to precipitate may be written as:

$$X_{FeO} + X_{MgO} + X_{SiO_2} \geq 1, \quad (2.2)$$

where X_i are the mole fractions of three metal oxides that are calculated as functions of the mole fractions and exchange coefficients for Fe, Mg, and O in the core as follows (Rubie, Frost, et al., 2011; Siebert et al., 2013; Rubie, Jacobson, et al., 2015; Fischer et al., 2015):

$$X_{FeO} = X_{Fe} \times X_O / K_O \quad (2.3)$$

$$X_{MgO} = X_{FeO} / X_{Fe} \times X_{Mg} / K_{Mg} \quad (2.4)$$

$$X_{SiO_2} = (X_{FeO} / X_{Fe})^2 \times X_{Si} / K_{Si}. \quad (2.5)$$

Here we assume that precipitated material is instantaneously removed from the core. To generate Fig. 2.2, we begin with an undersaturated core at 6,000 K. We then decrease the temperature in increments of 1 K until precipitation begins. Next, we calculate how much of each oxide to remove to return the core to equilibrium.

As temperature decreases further, the core gradually becomes depleted in light elements.

Thermochemical histories

Neglecting some small terms, the energy balance of the core is:

$$Q_{CMB} = Q_R + Q_S + Q_G + Q_{G'} + Q_L, \quad (2.6)$$

where Q_{CMB} is the heat flux across the CMB, Q_R is the amount of radiogenic heating, Q_S is the magnitude of secular cooling, Q_G and $Q_{G'}$ are gravitational energy changes associated with inner-core growth and Mg precipitation, respectively, and Q_L is the latent heat released from phase transitions (Nimmo, 2015). Heating due to dynamo activity is both generated and dissipated within the core and thus is not included. It is, however, important to the entropy balance (Nimmo, 2015):

$$E_\phi + E_K = E_R + E_S + E_G + E_{G'} + E_L. \quad (2.7)$$

Here E_ϕ , E_K and E_R are the entropy fluxes associated with ohmic dissipation, adiabatic heat flow, and radioactivity, respectively. The last four terms— E_S , E_G , $E_{G'}$ and E_L —are directly proportional to the rate of core cooling. We use parameterizations of these terms from Nimmo (2015), plus our own estimates of the contribution from the precipitation of Mg-rich material detailed below. Other analytical models for the evolution of the core may imply higher initial CMB temperatures for dynamos driven by thermal convection alone (Labrosse, 2015). Throughout, we assume that the thermal conductivity equals $130 \text{ W m}^{-1} \text{ K}^{-1}$, based on the vast majority of recent studies (Koker et al., 2012; Pozzo et al., 2012; Gomi et al., 2013; Seagle et al., 2013), and that the abundance of potassium (K) in the core is 100 parts per million.

Combining the entropy and energy balances yields an expression for the heat flow across the CMB that is needed to drive a dynamo:

$$Q_{CMB} = Q_R \left[1 - \frac{Q_T}{E_T} \left(\frac{E_R}{Q_R} \right) \right] + \frac{Q_T}{E_T} (E_\phi + E_K), \quad (2.8)$$

where the heat flow $Q_T = (Q_S + Q_G + Q_{G'} + Q_L)/(dT_{CMB}/dt)$ and the entropy $E_T = (E_S + E_G + E_{G'} + E_L)/(dT_{CMB}/dt)$ combine production terms that depend on the cooling rate. The temperature at the CMB is T_{CMB} . The implied cooling rate is $dT_{CMB}/dt = -(Q_{CMB} - Q_R)/Q_T$. If we assume a fixed value for E_ϕ , we can iterate these equations backwards in time from the present to calculate the thermo-chemical

history of the core. Increasing the amount of entropy required for the dynamo or the adiabatic heat flow implies higher initial temperatures and heat flow. Radiogenic heating limits the amount of secular cooling, but actually mandates higher core-to-mantle heat flow to sustain a dynamo. In reality, the thermal evolution of the mantle determines Q_{CMB} and thus the amount of entropy available for the dynamo. By assuming that E_ϕ is fixed to a particular value, we are essentially computing the minimum heat flow that the mantle must be able to accommodate from the core.

The gravitational contribution to core heating from Mg precipitation may be estimated as:

$$Q_{G'} = \int_{\infty} \psi \left(\frac{\partial \rho}{\partial t} \right)_{P,T} dV = \int_{\infty} \psi \rho \alpha_c C_m \left(\frac{dT_{CMB}}{dt} \right) dV, \quad (2.9)$$

where ψ is the gravitational potential, ρ is density, t is time, and V is volume. The coefficient of compositional expansivity $\alpha_c = -1/\rho(\partial\rho/\partial c)_{P,T} \approx 1.12$, where c is the concentration of the light elements that precipitate out of the core. The rate of precipitation, C_m , is normalized to the initial core mass and directly proportional to the rate of cooling dT_{CMB}/dt . Since inspection of Fig. 2 suggests that about 0.5% of initial core mass precipitates per 100 K of cooling, we set $C_m = 5 \times 10^{-5}$. The exclusion of Mg from the inner core, if any, is already taken into account by using the empirical density difference across the inner-core boundary to calculate the gravitational contribution from the solidification of the inner core. The associated entropy flux²⁶ is simply $E_{G'} = Q_{G'}/T_{CMB}$. The entropy contribution from the latent heat of precipitation is exactly zero if precipitation occurs at the top of the core. Accordingly, we do not include any contribution from latent heat of precipitation in our calculation of Q_{CMB} . At present, $Q_L \approx 5$ TW and the rate of inner-core growth by mass is perhaps 2 to 4 times the amount of precipitation (Nimmo, 2015). Including the latent heat of precipitation would possibly increase Q_{CMB} by 1–2 TW and slightly decrease the implied amount of secular cooling.

*Chapter 3***THERMAL EVOLUTION OF EARTH WITH MAGNESIUM
PRECIPITATION IN THE CORE****3.1 Abstract**

Vigorous convection in Earth's core powers our global magnetic field, which has survived for over three billion years. In this study, we calculate the rate of entropy production available to drive the dynamo throughout geologic time using one-dimensional parameterizations of the evolution of Earth's core and mantle. To prevent a thermal catastrophe in models with realistic Urey ratios, we avoid the conventional scaling for plate tectonics in favor of one featuring reduced convective vigor for hotter mantle. We present multiple simulations that capture the effects of uncertainties in key parameters like the rheology of the lower mantle and the overall thermal budget. Simple scaling laws imply that the heat flow across the core/mantle boundary was elevated by less than a factor of two in the past relative to the present. Another process like the precipitation of magnesium-bearing minerals is therefore required to sustain convection prior to the nucleation of the inner core roughly one billion years ago, especially given the recent, upward revision to the thermal conductivity of the core. Simulations that include precipitation lack a dramatic increase in entropy production associated with the formation of the inner core, complicating attempts to determine its age using paleomagnetic measurements of field intensity. Because mantle dynamics impose strict limits on the amount of heat extracted from the core, we find that the addition of radioactive isotopes like potassium-40 implies less entropy production today and in the past. On terrestrial planets like Venus with more sluggish mantle convection, even precipitation of elements like magnesium may not sustain a dynamo if cooling rates are too slow.

3.2 Introduction

The dynamo created in Earth's liquid outer core has survived for billions of years. Paleomagnetic studies of unmetamorphosed rocks with ages near 3.45 Gyr unambiguously show that the strength of Earth's global magnetic field at that time was at least half its present-day value (e.g., Tarduno, Cottrell, Watkeys, et al., 2010; Biggin, Wit, et al., 2011). No rocks of sufficiently low metamorphic grade have been found from earlier epochs, so the question of whether our magnetic field is even older

remains unanswered. Recently, detrital zircon crystals found in the Jack Hills of Western Australia were proposed to record field intensities of modern magnitudes (Tarduno, Cottrell, Davis, et al., 2015). These data are controversial, however, because zircon-bearing rocks in the Jack Hills may have suffered pervasive remagnetization related to the emplacement of a nearby igneous province (e.g., Weiss et al., 2015). In any case, how to power convection in the core and thus a dynamo for the vast majority of Earth's history remains one of the most pressing puzzles in geophysics.

Thermal convection in the core is possible if the heat flow across the core/mantle boundary (CMB) exceeds the rate at which heat is conducted along an adiabatic temperature gradient (e.g., Stevenson, 2003). Over the past few years, some theoretical calculations (e.g., Koker et al., 2012; Pozzo et al., 2012) and diamond-anvil cell experiments (e.g., Gomi et al., 2013; Seagle et al., 2013; Ohta et al., 2016) have indicated that the thermal conductivity of the core's iron-rich alloy is a factor of two to three larger than prior estimates. The conductive heat flux is $\sim 10\text{--}15$ TW at present according to these new values. However, countervailing evidence from high-pressure experiments that the previous, low values are actually correct has also been presented recently, so debate over this issue will likely continue (Konôpková et al., 2016).

Cooling rates approaching twice the conductive heat flux have been suggested as the minimum required to compensate for Ohmic dissipation (e.g., Stelzer and Jackson, 2013). But this dissipation mainly occurs at high harmonic degree and its scaling with dipole field strength is uncertain. Since the dissipation due to the low harmonics alone is far less than the actual heat flow, maintaining the observed field with a heat flow only mildly in excess of conduction along the adiabat is possible in principle. In any case, the actual CMB heat flow of $\sim 5\text{--}15$ TW estimated from seismology and mineral physics (e.g., Lay et al., 2008) may be only marginally sufficient to sustain the dynamo by thermal convection alone. Fortunately, the dynamic chemistry of the core yields additional sources of energy.

The exclusion of light elements from the solidifying inner core provides enough compositional buoyancy to drive convection today. Once compositional buoyancy is present, the heat flow out of the core need not exceed conduction along the adiabat (i.e., convection can even carry heat downwards). In practice, models with a growing inner core also benefit from the significant release of latent heat and accordingly require less rapid cooling. Conventional calculations have indicated

that the inner core nucleated roughly one billion years ago (e.g., Labrosse, Poirier, et al., 2001). The age of the inner core is several hundred million years less in models with increased CMB heat flow and thus faster cooling/freezing to accommodate the revised values for thermal conductivity (e.g., Nimmo, 2015; Labrosse, 2015).

The energy available for dissipation in dynamo generation dramatically increases once the inner core forms, which might imply a larger magnetic field according to scaling laws where the buoyancy flux determines the global field strength (e.g., Christensen, 2010). In some canonical models, the inner core thus prevents the dynamo from turning off (e.g., Stevenson et al., 1983), but these models do not explain the current total heat flow of Earth. Biggin, Piispa, et al. (2015) claimed to observe an increase in Earth's dipole moment associated with the formation of the inner core in the Mesoproterozoic. Given the relevant experimental and statistical uncertainties, however, the available data are arguably consistent with roughly constant field intensities throughout the Precambrian (e.g., Smirnov et al., 2016).

O'Rourke and Stevenson (2016) proposed the precipitation of magnesium-bearing minerals as an alternative power source. One or two weight percent of magnesium can partition into the core in the high-temperature aftermath of giant impacts during Earth's accretion according to earlier calculations (Wahl and Militzer, 2015) and subsequent diamond-anvil cell experiments (Badro, Siebert, et al., 2016). Because its solubility in iron alloy is strongly-temperature dependent, subsequent cooling quickly saturates the core in magnesium. Elements like aluminum and calcium may have similar thermodynamic properties (Badro, Siebert, et al., 2016), but their abundances are relatively small. Transporting magnesium-rich oxide or silicate across the CMB provides an order-of-magnitude more gravitational energy than freezing an equivalent mass of the inner core. Precipitation drives vigorous, compositional convection before the nucleation of the inner core, even without vastly higher CMB heat flow than today. O'Rourke and Stevenson (2016), however, only calculated the CMB heat flow implied by a constant rate of entropy production for the dynamo. In reality, mantle dynamics control CMB heat flow, so entropy production should vary over time.

The purpose of this paper is to describe simple models of Earth's thermal evolution that are consistent with the observed longevity of the dynamo. First, we describe how we couple a one-dimensional model of the core to simple scaling laws for mantle dynamics. We next identify which parameters control the amount of power

available for the dynamo throughout geologic time. Specifically, we focus on the rheology of the boundary layer at the base of the mantle and the abundance of radioactive isotopes like potassium-40 in the core. After presenting representative simulations, we discuss the limitations of our model for early Earth history and the implications for other planets.

3.3 Theoretical formulation

In this section, we present a parametrized model for the coupled evolution of Earth's core and mantle. Figure 3.1 shows the simplified structure with which we calculate thermal histories. Key model parameters are listed in Table 3.1. As in nearly all models of core history for the past fifty years, we assume that the core is sufficiently low viscosity that the convective state is extremely close to an isentropic and homogeneous state, except in thin boundary layers (e.g., Stevenson, 1987). Although most previous studies (e.g., Stevenson et al., 1983; Buffett, 2002) only consider a thermal boundary layer at the base of the mantle, we allow for the existence of a stagnant layer that may not participate in convection because it is compositionally dense (Hernlund and McNamara, 2015), possibly the solidified remnant of a basal magma ocean (e.g., Labrosse, Hernlund, et al., 2007). The existence of this distinct chemical layer could explain why the thermal excess associated with mantle plumes may be less than half the total temperature contrast across the CMB (e.g., Farnetani, 1997). Because our primary focus is how mantle dynamics affect the evolution of the core, we do not model the dynamics of the crust and lithosphere in detail. Finally, we present simulations that demonstrate the effects of varying key parameters.

Evolution of the mantle

The governing equation here is the global energy balance for the mantle (e.g., Christensen, 1985):

$$C_M \frac{dT_M(t)}{dt} = H_M(t) - Q_M(t) + Q_{CMB}(t), \quad (3.1)$$

where C_M is the heat capacity of the entire mantle, T_M is the potential temperature of the mantle, H_M is the radiogenic heating in the convecting mantle, Q_M is the heat flow out of the surface from mantle convection, and Q_{CMB} is heat flow across the core/mantle boundary. Heat-producing elements are partially sequestered in the continental crust, so H_M is less than the present-day heat production of the bulk silicate Earth. Table 3.2 lists the values we adopt for parameters like C_M that are generally fixed in our simulations.

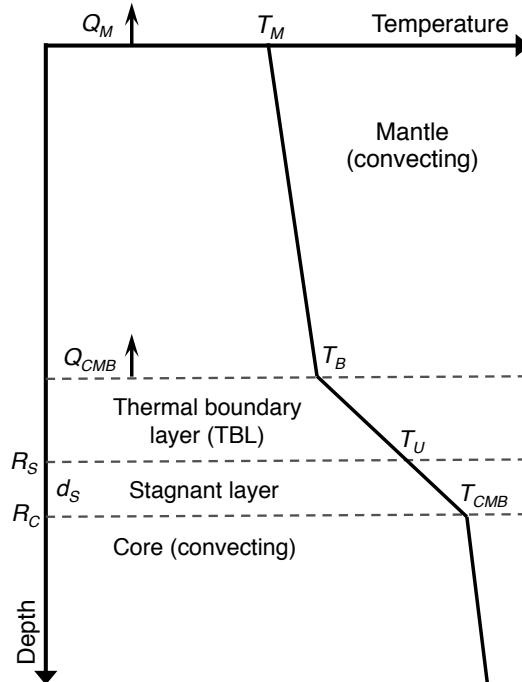


Figure 3.1: Cartoon showing the assumed thermal structure of Earth and the key parameters tracked during simulations of Earth’s evolution. The temperature gradients and vertical dimensions of each layer are not to scale.

At present, how to calculate Q_M remains quite controversial. Conventional scalings for Q_M assume that the mantle behaves like a simple convecting system in which hotter temperature yields an increased vigor of convection and thus heat flow. But there is a well-known problem with these scalings that arises when the convective Urey ratio, $Ur(t) = H_M(t)/Q_M(t)$, is considered (Christensen, 1985). Integrating Eq. 3.1 backwards in time yields unrealistically high values of T_M unless the present-day $Ur(t_0) \sim 0.75$. Robust geochemical constraints, however, imply that $Ur(t_0) \sim 0.2$ to 0.4 in reality (e.g., Korenaga, 2008; Lay et al., 2008).

Using the realistic Urey ratio in simulations of Earth’s evolution produces a “thermal catastrophe” in which calculated mantle temperatures before $\sim 2\text{--}3$ Ga rapidly exceed petrological constraints (e.g., Herzberg et al., 2010). To avoid this problem, we calculate Q_M as a function of T_M following Korenaga (2006). This simple formulation is sufficient for the purposes of this study and is consistent with fully dynamical models (e.g., Korenaga, 2010b), especially considering uncertainties related to mantle hydration and the scaling of bending dissipation for subducting plates (e.g., Rose and Korenaga, 2011; Korenaga, 2011).

Term	Definition
Q_M	Heat flow from the mantle
Q_{CMB}	Heat flow from the core
Q_R	Radiogenic heating in the core
Q_S	Secular cooling of the core
Q_P	Gravitational energy release from precipitation
Q_G	Gravitational energy release from the inner core
Q_L	Latent heat associated with the inner core
H_M	Radiogenic heating in the convecting mantle
T_M	Potential temperature of the mantle
T_B	Basal temperature of the convecting mantle
T_U	Temperature at the top of the stagnant layer
T_{CMB}	Temperature of the uppermost core
T_I	Temperature at the inner core boundary
R_I	Radius of the inner core
E_K	Entropy production associated with conduction
E_ϕ	Entropy production available for the dynamo

Table 3.1: List of key parameters tracked during simulations of Earth’s thermal evolution and their definitions.

Term	Definition	Value	Units	Ref.
C_M	Specific heat capacity of the mantle	4.5×10^{27}	J	[1]
k_M	Thermal conductivity in the stagnant layer	5	$\text{W m}^{-1} \text{K}^{-1}$	[2]
$\eta_B(T_{ref})$	Mantle viscosity at reference temperature	2×10^{21}	Pa s	[3]
T_{ref}	Reference temperature for mantle viscosity	2500	K	[3]
$k_C(0)$	Thermal conductivity at the core’s center	163	$\text{W m}^{-1} \text{K}^{-1}$	[4]
L_p	Length scale for density profile in the core	8049	km	[4]
A_p	Constant for density profile in the core	0.4835		[4]
A_k	Constant for conductivity profile in the core	2.39		[4]
dT_m/dP	Liquidus slope at the inner core boundary	9	K GPa^{-1}	[4]

Table 3.2: Values of parameters held fixed in our simulations. Other constants used to simulate the evolution of the mantle and to calculate the terms in the energy and entropy balances of the core were taken without modification from Korenaga (2006) and Labrosse (2015) unless otherwise indicated. References: [1] Christensen (1985), [2] Tang et al. (2014), [3] Korenaga (2005), and [4] Labrosse (2015).

The properties of the thermal boundary layer at the base of the mantle determine the core/mantle heat flow. We incorporate a simple boundary-layer model resting on the assumption that convective instability occurs once a local Rayleigh number reaches a critical value. Thus, we calculate the value of Q_{CMB} at any epoch relative to the present (Buffett, 2002):

$$\frac{Q_{CMB}(t_1)}{Q_{CMB}(t_0)} = \left(\frac{T_U(t_1) - T_B(t_1)}{T_U(t_0) - T_B(t_0)} \right)^{\frac{4}{3}} \left(\frac{\eta_B[\bar{T}(t_0)]}{\eta_B[\bar{T}(t_1)]} \right)^{\frac{1}{3}}, \quad (3.2)$$

where $\bar{T}(t) = [T_U(t) + T_B(t)]/2$ is the average temperature in the thermal boundary layer. Assuming whole-mantle convection as indicated by seismic tomography of slabs and plumes (e.g., Hilst et al., 1997; French and Romanowicz, 2015), the temperature at the base of the mantle scales as $T_B(t_1) = [T_M(t_1)/T_M(t_0)]T_B(t_0)$. If convection in the mantle were layered, then T_B would increase by the temperature contrast across the mid-mantle transition layer. Thus, the estimated temperature contrast across the CMB would decrease.

The effective viscosity of the thermal boundary layer is calculated as (Korenaga, 2005)

$$\eta_B(T) = \eta_B(T_{ref}) \exp \left[\frac{H_{eff}}{RT} - \frac{H_{eff}}{RT_{ref}} \right], \quad (3.3)$$

where H_{eff} is the activation enthalpy, R is the universal gas constant, and $\eta_B(T_{ref})$ is the reference viscosity, comparable to the average viscosity of the lower mantle, at some reference temperature T_{ref} . Typical values assumed for H_{eff} are on the order of ~ 300 kJ mol⁻¹. But the rheology of the lower mantle is uncertain enough that negative values are also possible, in which case hotter material would have higher viscosity (e.g., Solomatov, 1996; Korenaga, 2005).

Assuming the stagnant layer is in a steady state, the temperature at the top of the stagnant layer is easily calculated (e.g., Turcotte and Schubert, 2002):

$$T_U = T_{CMB} - \frac{Q_{CMB}}{4\pi k_M} \left(\frac{1}{R_C} - \frac{1}{R_S} \right), \quad (3.4)$$

where T_{CMB} is the temperature at the top of the core, k_M is the thermal conductivity of the lower mantle, and $R_S = R_C + d_S$ is the distance from the center of Earth to the top of the stagnant layer. The effective thickness of the stagnant layer is d_S . Small changes to d_S (<10 km) are degenerate with the slight decrease in T_U caused by plausible rates of radiogenic heating in the stagnant layer, which we neglect.

Energetics of the core

The global energy balance for the core is (e.g., Labrosse, 2015):

$$Q_{CMB} = Q_R + Q_S + Q_P + Q_G + Q_L, \quad (3.5)$$

where Q_R is radiogenic heating and Q_S is secular cooling. Gravitational energy associated with the precipitation of magnesium-bearing minerals is Q_P (e.g., Buffett et al., 2000; O'Rourke and Stevenson, 2016). The final two terms are the gravitational energy (Q_G) and latent heat (Q_L) associated with the growth of the inner core. Note

that the ohmic dissipation of the dynamo is not included here, because such heating is both generated and dissipated entirely within the core. Analytic expressions for all but one term are available in Labrosse (2015), along with associated constants like the density contrast at the inner core boundary and the slopes of the liquidus and isentropic temperature gradients. We derive a polynomial expression for Q_P in the Appendix. In O'Rourke and Stevenson (2016), we presented an expression for Q_P compatible with the formulation of Nimmo (2015). We use the fourth-order expansion of Labrosse (2015) in this paper for a better match to the density structure of the core from PREM and estimates of the heat gradients at the top of the core.

We approximate the thermal conductivity within the core using a quadratic polynomial (Labrosse, 2015):

$$k_C(r) = k_C(0) \left(1 - A_k \frac{r^2}{L_p^2} \right), \quad (3.6)$$

where r is radial distance, L_p is derived from the equation of state for the liquid core alloy, and A_k is a constant. According to most recent studies, the thermal conductivity at the center of the core is $k_C(0) \approx 163 \text{ W m}^{-1} \text{ K}^{-1}$ (e.g., Labrosse, 2015). But we run some simulations using values as low as $40 \text{ W m}^{-1} \text{ K}^{-1}$ (Konôpková et al., 2016).

Each of the terms besides Q_R are proportional to the cooling rate of the core. That is,

$$Q_{CMB} = Q_R + (\tilde{Q}_S + \tilde{Q}_P + \tilde{Q}_G + \tilde{Q}_L) \frac{dT_{CMB}}{dt}, \quad (3.7)$$

where $\tilde{Q}_i = Q_i / (dT_{CMB}/dt)$. The growth rate of the inner core is simply proportional to the overall cooling rate as $dR_I/dt = \gamma_I (dT_{CMB}/dt)$. Here, we use a conversion factor (Nimmo, 2015):

$$\gamma_I = \frac{-1}{\frac{dT_m}{dP} - \frac{dT_a}{dP}} \left(\frac{T_I}{g \rho_I T_{CMB}} \right), \quad (3.8)$$

where dT_m/dP and dT_a/dP are the slopes of the melting curve and adiabatic temperature gradient, respectively, at the inner core boundary. Likewise, T_I and ρ_I are the temperature and density at the inner core boundary calculated from the adiabatic profiles in Labrosse (2015).

Another equation expresses the conservation of entropy production (e.g., Gubbins, 1977; Labrosse, 2015):

$$\frac{Q_{CMB}}{T_{CMB}} = \frac{Q_R}{T_R} + \frac{Q_S}{T_S} + \frac{Q_L}{T_L} + E_K + E_\phi, \quad (3.9)$$

where T_R , T_S , and T_L are effective temperatures at which the respective heat sources are dissipated. The entropy production rates associated with conductive heat transport along the adiabatic temperature gradient and ohmic dissipation are E_K and E_ϕ , respectively.

Rearranging Eq. 3.7, the cooling rate of the core is

$$\frac{dT_{CMB}}{dt} = \frac{Q_{CMB} - Q_R}{\tilde{Q}_S + \tilde{Q}_P + \tilde{Q}_G + \tilde{Q}_L}. \quad (3.10)$$

Combining Eqs. 3.7 and 3.9, we finally calculate the entropy available to sustain the dynamo:

$$E_\phi = \frac{Q_{CMB}}{T_{CMB}} - \frac{Q_R}{T_R} - \left(\frac{\tilde{Q}_S}{T_S} + \frac{\tilde{Q}_L}{T_L} \right) \frac{dT_{CMB}}{dt} - E_K. \quad (3.11)$$

To sustain a dynamo, E_ϕ must of course be positive. Something in the rather wide range of $\sim 20\text{--}500 \text{ MW K}^{-1}$ is probably required, and the actual minimum value is poorly constrained because ohmic dissipation occurs at short length scales that are difficult to simulate (e.g., Gubbins, 1977). We can estimate the energy associated with ohmic dissipation as $Q_\phi = T_\phi E_\phi$, where $T_\phi \approx 5000 \text{ K}$ is some characteristic temperature of dissipation between T_{CMB} and the temperature at the inner core boundary (Nimmo, 2015). The dissipation rate is an acceptable proxy for magnetic field strength, although more complicated scaling laws have been formulated (e.g., Christensen, 2010).

Only a portion of core formation occurred in the aftermath of giant impacts. Since the equilibration temperature for most material was $< 4500 \text{ K}$, the core was likely undersaturated in light elements at first, assuming full mixing and an initially homogeneous core. Thus, precipitation of magnesium-bearing minerals was delayed until after an initial episode of cooling (O'Rourke and Stevenson, 2016; Badro, Siebert, et al., 2016). Once started, however, precipitation continues until the core is entirely depleted in light elements. Here we assume that precipitation has been occurring for the entire length of our simulations, meaning that the core became saturated within $\sim 500 \text{ Myr}$ after accretion.

Based on diamond-anvil cell experiments conducted at extreme temperature/pressure conditions, Badro, Siebert, et al. (2016) determined that pure MgO would precipitate at a rate $C_M \approx 2.5 \times 10^{-5} \text{ K}^{-1}$ normalized to the total mass of the core. O'Rourke and Stevenson (2016) included SiO_2 and FeO in the precipitate and did not assume the core and mantle were in equilibrium after accretion, yielding a larger $C_M \approx 5 \times 10^{-5} \text{ K}^{-1}$. These calculations were based on extrapolations of earlier

experiments conducted at lower temperatures, but Badro, Siebert, et al. (2016) obtained roughly consistent expressions for the relevant exchange coefficients. Entropic arguments suggest that the precipitate should include every element present in the outer core. Because Mg is least soluble, the precipitate is initially MgO-rich but contains increasing amounts of SiO_2 as T_{CMB} decreases. The initial abundances of each element—several combinations of which satisfy constraints from seismology and mineral physics (e.g., Badro, Côté, et al., 2014; Fischer et al., 2015)—dictate the evolving composition of the precipitate. Given the myriad uncertainties, we use the intermediate value $C_M = 4 \times 10^{-5} \text{ K}^{-1}$ for most simulations but also describe the implications of higher or lower values.

If E_ϕ is assumed to have been roughly constant throughout geologic time, then we can modify the above equations to calculate the implied values of Q_{CMB} and T_{CMB} in the past (e.g., O'Rourke and Stevenson, 2016). However, since mantle dynamics actually control Q_{CMB} and thus T_{CMB} as detailed above, using Eq. 3.11 and a coupled model of core/mantle evolution is required to determine what scenarios are compatible with the observed longevity of Earth's dynamo.

Calculating thermochemical histories

Various observational constraints on the thermal budget of Earth today are available. The total heat flux at the surface is $44 \pm 3 \text{ TW}$ (Jaupart et al., 2007). Estimates of the present-day heat production in the bulk silicate Earth range from $16 \pm 3 \text{ TW}$ (Lyubetskaya and Korenaga, 2007b) to $\sim 20 \text{ TW}$ (Jaupart et al., 2007). Arguments from mineral physics and seismology have implied that the core/mantle boundary heat flow is currently ~ 5 to 15 TW (e.g., Lay et al., 2008). With heat production in the continental crust estimated as ~ 6 to 8 TW (Jaupart et al., 2007), radiogenic heating in the mantle is perhaps ~ 6 to 14 TW and reasonable values for the mantle heat flux might be ~ 33 to 41 TW . Experiments on metal-silicate partitioning suggest that the abundance of potassium in the core is less than 200 ppm (e.g., Corgne et al., 2007), implying that radiogenic heating in the core is $< 1.5 \text{ TW}$ at present.

Absolute temperatures within Earth now are comparably uncertain. Extrapolating temperatures of the relevant phase transitions at the mantle's transition zone down an adiabatic gradient imply that the basal temperature of the mantle is ~ 2500 to 2800 K . With a present-day temperature of $\sim 4000 \text{ K}$ at the top of the core (Labrosse, 2015), the temperature contrast across the core/mantle boundary is ~ 1000 to 1800 K , much larger than the thermal excess of $< 500 \text{ K}$ attributed to mantle plumes (e.g., French

and Romanowicz, 2015). Note that this thermal excess may diminish by a factor of roughly two as plumes ascend from the CMB to the upper mantle. That is, a near-surface thermal excess of ~ 250 K may imply a temperature difference of ~ 500 K across the thermal boundary layer at the base of the mantle (e.g., Leng and Zhong, 2008).

Using the present as an “initial” condition, we can integrate the equations presented above backwards in time to calculate a thermochemical history of Earth. The present-day thermal budget has significant uncertainties, but constraints on the state of the mantle and core at the time that plate tectonics began are obviously much weaker. This procedure may not reproduce the state of the core and mantle throughout the Hadean because scaling laws other than those presented above or more complicated numerical simulations are required to model the aftermath of giant impacts, the solidification of the primordial magma ocean, and any regime of mantle dynamics that may have preceded plate tectonics. Accordingly, the primary utility of our approach is to reconstruct a thermal history for the mantle consistent with geologic evidence for the period when the geodynamo definitely existed.

In every simulation, we assume that $T_B(t_0) = 2800$ K and that continents grew to their modern size by 4 Ga. Using the adiabatic temperature gradient for the core from Labrosse (2015) implies that $T_{CMB} \approx 4050$ K given the present-day radius of the inner core, $R_I = 1220$ km. Unless otherwise indicated, we use the following set of “nominal” parameters: $Q_M(t_0) = 36$ TW, $Q_{CMB}(t_0) = 10$ TW, $H_M(t_0) = 10$ TW, $H_{eff} = 300$ kJ mol $^{-1}$ and $[K] = 50$ ppm in the core. With 8 TW of radiogenic heating in the continental crust in this case, the present-day heat flow thus totals 44 TW. We also assume that the effective thickness of the stagnant layer, $d_S = 50$ km, except when $Q_{CMB}(t_0)$ is varied.

3.4 Results

Figure 3.2 shows the results of the thermal evolution simulation using our nominal parameters. With the rate of magnesium precipitation $C_M = 4 \times 10^{-5}$ K $^{-1}$ (normalized to the total mass of the core), $E_\phi > 500$ MW K $^{-1}$ at all times. The entropy production rises to maxima of ~ 670 and 630 MW K $^{-1}$ near 0.65 and 2.5 Ga, respectively, equivalent to ohmic dissipation rates of $Q_\phi \approx 3.1$ – 3.4 TW that are well above the minimum estimated to sustain a dynamo (e.g., Nimmo, 2015). The age of the inner core is ~ 0.83 Ga, at which point Q_L and Q_G disappear and the entropy production rate reaches a local minimum. At present day, the temperature differences

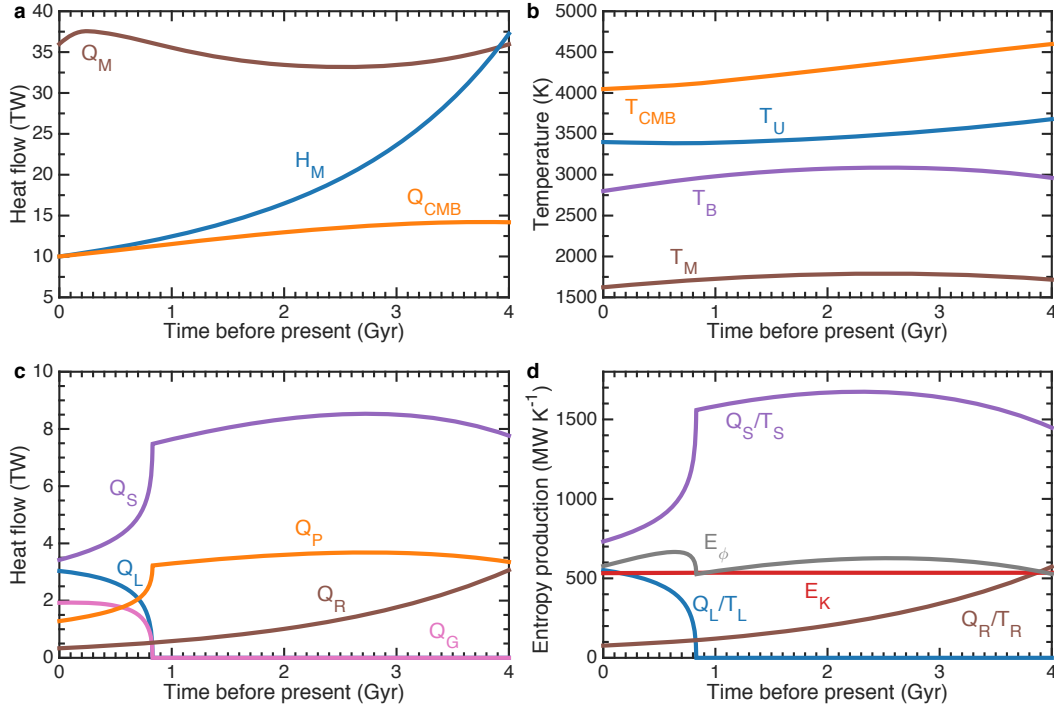


Figure 3.2: Simulation of the thermal evolution of Earth with nominal initial conditions: $k_C(0) = 163 \text{ W m}^{-1} \text{ K}^{-1}$, $Q_M(t_0) = 36 \text{ TW}$, $Q_{CMB}(t_0) = 10 \text{ TW}$, $H_M(t_0) = 10 \text{ TW}$, $H_{eff} = 300 \text{ kJ mol}^{-1}$, $d_S = 50 \text{ km}$, and $[K] = 50 \text{ ppm}$. Magnesium-bearing minerals precipitate from the core at a rate of $C_M = 4 \times 10^{-5} \text{ K}^{-1}$. a) Heat budget of the mantle. b) Temperatures of the mantle and core. Contributions to the energy (c) and entropy (d) budgets of the core.

across the thermal boundary layer and the adjacent stagnant layer are both $\sim 600 \text{ K}$, which roughly matches constraints on the thermal excess associated with mantle plumes and the total temperature contrast across the core/mantle boundary. For the entire simulation, the change in entropy content associated with thermal conduction is as large as the total entropy production available for the dynamo (i.e., $E_K \approx E_\phi$). Precipitation is critical to the operation of a dynamo before inner core nucleation, even though $Q_P \sim 0.5Q_S$. That is, the contribution of secular cooling to the total dissipation is penalized by a Carnot-like efficiency term $\sim (T_S - T_{CMB})/T_{CMB}$ relative to compositional buoyancy from precipitation or the inner core (Nimmo, 2015; Labrosse, 2015).

Figure 3.3 illustrates the effects of varying the rate of magnesium precipitation. Five simulations were performed with C_M increasing from 0 to $8 \times 10^{-5} \text{ K}^{-1}$ in increments of $2 \times 10^{-5} \text{ K}^{-1}$. Increasing C_M yields increased entropy production rates, along with decreased Q_{CMB} and T_{CMB} in the past. At least some precipitation is required to

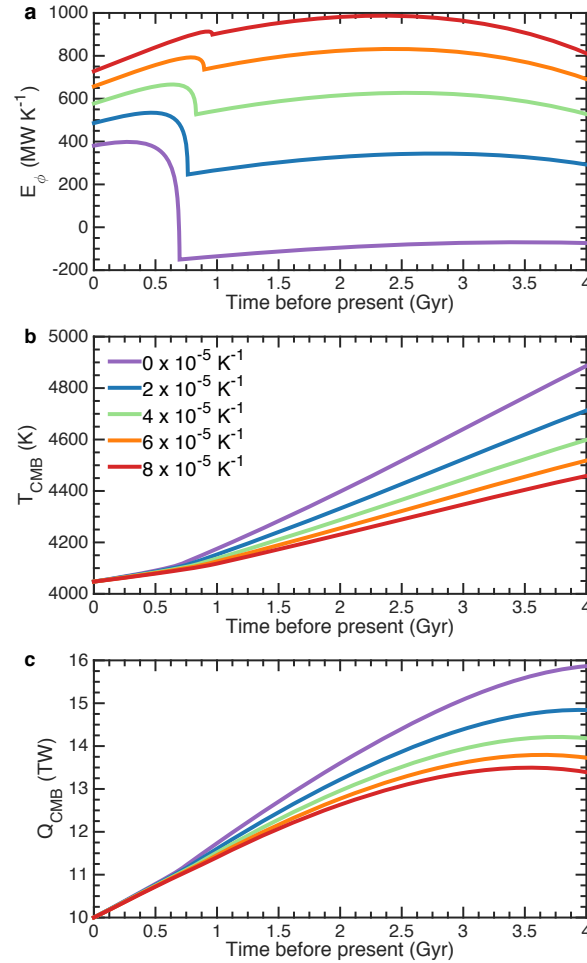


Figure 3.3: Multiple simulations showing that increasing the precipitation rate of magnesium-bearing minerals increases the entropy production for the dynamo (a) and, relative to the present, decreases the implied temperatures of the core (b), core/mantle heat flow (c) in the past.

maintain positive values of E_ϕ before nucleation of the inner core. Moreover, values of $C_M \geq 4 \times 10^{-5} K^{-1}$ are preferred because E_ϕ must be significantly larger than zero to sustain a global magnetic field (e.g., Nimmo, 2015). Magnesium precipitation notably limits the extent to which E_ϕ , and thus presumably the strength of Earth's magnetic field recorded at the surface, reaches a local minimum at the time of inner core nucleation. That is, entropy production rates are roughly constant within $\sim 10\%$ throughout geologic time in simulations with $C_M \gtrsim 4 \times 10^{-5} K^{-1}$.

We repeated the simulations shown in Fig. 3.3 with the thermal conductivity decreased from $k_C(0) = 163$ to $40 W m^{-1} K^{-1}$. With all other parameters held constant, E_K is the only term affected. Thus, the evolution of Q_{CMB} and T_{CMB}

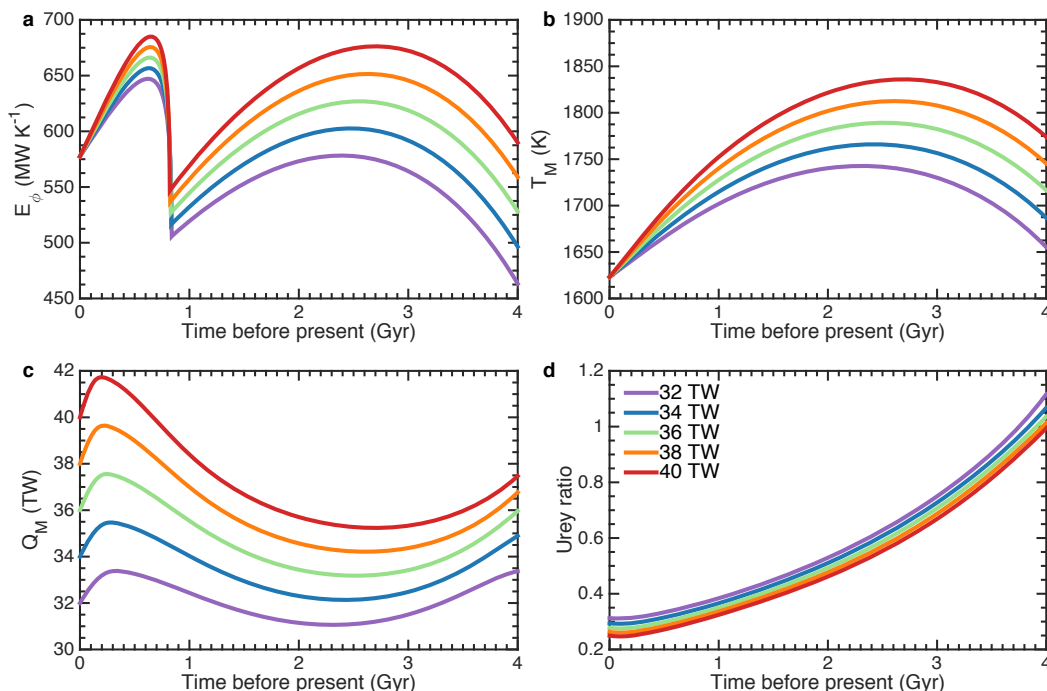


Figure 3.4: Simulations showing that increasing the mantle heat flow implies increased rate of entropy production available for the dynamo in the past (a), potential temperature of the mantle (b), and heat flow from the mantle to the surface (c), while the Urey ratio (d) is decreased.

is unchanged, while E_ϕ is increased by ~ 400 MW K⁻¹ at all times. If the lowest estimates of thermal conductivity are actually correct (Konôpková et al., 2016), then magnesium precipitation is not required to maintain positive dissipation. However, at least $C_M = 2 \times 10^{-5}$ is still necessary to unambiguously sustain a dynamo with $E_\phi > 500$ MW K⁻¹ at all times.

Figure 3.4 elucidates how varying the mantle heat flow affects the evolution of the core. Simulations were performed with $Q_M(t_0)$ varied from 32 to 40 TW to represent the uncertainties in the thermal budget of Earth. In each of these simulations, $C_M = 4 \times 10^{-5}$ K⁻¹, $H_M(t_0) = 10$ TW, and 8 TW of radiogenic heating is assumed for the continental crust. Increasing $Q_M(t_0)$ implies more entropy production for the dynamo in the past, along with higher values of both Q_M and T_M . The effect on the dynamics of the core, however, is relatively small compared to the uncertainties centered on the other parameters described above. In these simulations, the present-day Urey ratio is ~ 0.3 , increasing to ~ 1 – 1.2 at 4 Ga. However, using a high present-day Urey ratio (~ 0.75), together with conventional scaling laws for mantle dynamics, would only marginally affect our results, at least during the few

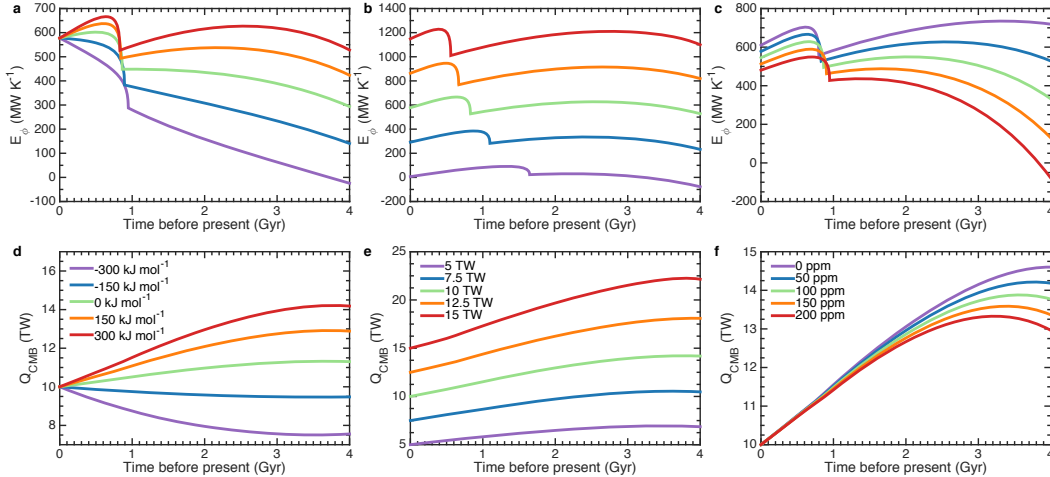


Figure 3.5: Simulations with H_{eff} varied from -300 to 300 kJ mol^{-1} (left), $Q_{CMB}(t_0)$ from 5 to 15 TW (center), and $[\text{K}]$ from 0 to 200 ppm (right). Top: Rate of entropy production available for the dynamo. Bottom: Heat flow across the core/mantle boundary.

billion years before the “thermal catastrophe” renders the mantle globally molten.

Figure 3.5 contains tests of the sensitivity of our simulations to three additional parameters. Each simulation has $C_M = 4 \times 10^{-5} \text{ K}^{-1}$ so that positive dissipation is maintained in most cases. Decreasing C_M to $2.5 \times 10^{-5} \text{ K}^{-1}$ only lowers the estimated entropy production rates by $\sim 100 \text{ MW K}^{-1}$ at all times. Conventional scalings have the viscosity of the lower mantle decreasing with increasing temperature (e.g., Buffett, 2002). In this case, the CMB heat flow is higher in the past. If $H_{eff} = 300 \text{ kJ mol}^{-1}$, the implied value is almost 15 TW at 4 Ga for $Q_{CMB}(t_0) = 10 \text{ TW}$. Attaining more than twice the present-day CMB heat flow in the past is difficult, requiring $H_{eff} \geq 600 \text{ kJ mol}^{-1}$ and the absence of any compositionally-distinct, stagnant layer.

The rheology of the lower mantle is poorly constrained. If the grain size-dependent part of diffusion creep dominates, then hotter mantle may actually have higher viscosity (Solomatov, 1996; Korenaga, 2005). In simulations with negative values of H_{eff} , hotter temperatures in the past would imply a thicker thermal boundary layer at the base of the mantle, leading to inhibited Q_{CMB} and thus a lower likelihood of sustaining a dynamo. With $H_{eff} = -300 \text{ kJ mol}^{-1}$, the viscosity contrast across the thermal boundary layer is roughly one order of magnitude as long as a stagnant, compositionally-distinct layer with $d_S = 50 \text{ km}$ is still present. If H_{eff} were even more negative, however, then the viscosity contrast may become large enough that

the bottom portion of the thermal boundary layer would itself stagnate, despite its compositional homogeneity (e.g., Solomatov and Moresi, 2000). In this case, calculating Q_{CMB} is more complicated (Korenaga, 2005), and a compositionally distinct layer is not required to explain the different thermal excesses associated with the CMB and mantle plumes.

Rates of entropy production are very sensitive to the present-day core/mantle heat flow. To maintain roughly equal differences in temperature across the lower thermal boundary layer for the simulations in Fig. 3.5, we vary d_S from 72 km for $Q_{CMB}(t_0) = 5$ TW to 38 km for $Q_{CMB}(t_0) = 15$ TW in equal increments of 12 km per 5 TW. If $Q_{CMB}(t_0)$ is ~ 5 TW, at the lower end of modern estimates, then even $C_M = 5 \times 10^{-5} \text{ K}^{-1}$ is insufficient to sustain positive dissipation. Without precipitation, $E_\phi \approx 100\text{--}150 \text{ MW K}^{-1}$ before the inner core nucleates if $Q_{CMB}(t_0) = 15$ TW, $[\text{K}] = 0$ ppm, and $H_{eff} = 300 \text{ kJ mol}^{-1}$. However, higher dissipation rates are likely required to produce the present-day magnetic field strength (Nimmo, 2015). Decreasing $Q_{CMB}(t_0)$ implies that values of Q_{CMB} are depressed by roughly the same amount in the past and also that the inner core is older.

Increased abundances of potassium in the core imply lower rates of ohmic dissipation in the past. This result may seem counterintuitive because radiogenic heating is a positive source of energy and entropy—albeit an inefficient one because of another Carnot-like efficiency term. Calculations that consider only the thermal evolution of the core demonstrate that increased radioactivity lowers the amount of secular cooling required to sustain a dynamo and thus the temperature of the core in the past, but also necessitates a higher core/mantle heat flow (e.g., Nimmo, 2015; Labrosse, 2015; O’Rourke and Stevenson, 2016). There is no reason, however, that Q_{CMB} should increase because of radiogenic heating in the core. In fact, the relatively slow cooling implied by such heating tends to decrease Q_{CMB} by lowering the temperature contrast across the core/mantle boundary. Fundamentally, the rheology of the lower mantle governs Q_{CMB} . Any given value of Q_{CMB} will yield more entropy for a dynamo if cooling causes inner core growth or precipitation rather than just removing heat from the decay of potassium or other radioactive isotopes of uranium and thorium.

We also repeated these sensitivity tests using the lower bound on thermal conductivity. With $k_C(0) = 40 \text{ W m}^{-1} \text{ K}^{-1}$, positive dissipation is always maintained for each value of H_{eff} , $Q_{CMB}(t_0)$, and $[\text{K}]$ even absent precipitation. Low thermal conductivity also permits $E_\phi \approx 400 \text{ MW K}^{-1}$ when $Q_{CMB}(t_0) = 5$ TW and

$C_M = 4 \times 10^{-5} \text{ K}^{-1}$. If $Q_{CMB}(t_0) = 5 \text{ TW}$ with low thermal conductivity but no precipitation, then $E_\phi \approx 100 \text{ MW K}^{-1}$ in the past and rises to $\sim 300 \text{ MW K}^{-1}$ when the inner core nucleates at $\sim 1.4 \text{ Gyr}$ before today. Increasing $Q_{CMB}(t_0)$ to 15 TW then yields ~ 500 and 1250 MW K^{-1} of entropy production prior to and following the nucleation of the inner core, respectively.

3.5 Discussion

Earth's initially hot state

The final stage of Earth's formation featured a number of violent collisions, notably including the Moon-forming impact, that would have at least partially melted the mantle (e.g., Rubie, Jacobson, et al., 2015). Even absent giant impacts, the gravitational energy associated with accretion is large enough to create temperatures in the core and mantle much higher than those prevailing today. Without high temperatures at the time of core formation, insufficient magnesium would partition into the core to provide an appreciable amount of compositional buoyancy during its later evolution (Wahl and Militzer, 2015; O'Rourke and Stevenson, 2016; Badro, Siebert, et al., 2016). If extrapolated backwards until the time of Earth's accretion, however, our scalings of plate tectonics predict that the mantle was not much hotter than it is today. Efficient heat loss from a vigorously convecting magma ocean must have actually occurred after accretion. We have not explicitly included a period of rapid cooling before the initiation of plate tectonics, so our simulations may not be representative of Earth's earliest history.

Assuming that plate tectonics operated throughout the Proterozoic is quite reasonable (e.g., Korenaga, 2013), and our central goal is explaining how Earth sustained a dynamo throughout this eon. Observational evidence for the operation of plate tectonics is lacking for the same reason—a scarcity of rocks—that the existence of a magnetic field in the deep past remains controversial. Calculations in this paper and fully dynamical simulations using the new scaling for plate tectonics suggest that the potential temperature of the mantle was $\sim 1800 \text{ K}$ at $>3 \text{ Ga}$ (Herzberg et al., 2010; Korenaga, 2011). Crucially, this is within $\sim 100 \text{ K}$ of the potential temperature necessary for a surface magma ocean (e.g., Rubie, Jacobson, et al., 2015), meaning that our simulations of plate tectonics should smoothly connect with models that describe the solidification of a magma ocean and possibly another, short-lived regime of mantle convection (e.g., Moore and Webb, 2013).

A magma ocean extending from the surface through the transition zone to 660 km

depth would have existed when the potential temperature was $\sim 2200\text{--}2300$ K (e.g., Rubie, Jacobson, et al., 2015). Subsequently cooling the mantle by ~ 400 K over 1 Gyr, for example, to the state when plate tectonics may have begun requires $Q_M \sim 100$ TW from the magma ocean, more than twice the heat flow associated with solid-state convection. Of course, the actual lifespan of the surface magma ocean, which could be much shorter than 1 Gyr, is very uncertain (e.g., Solomatov, 2007). Additionally, the temperature of the core may have decreased by ~ 1000 K or more during the earliest phase of cooling after Earth's "hot start." After this initial burst, a long-lived magma ocean at the base of the mantle may have delayed the onset of the geodynamo. That is, the core would not continue cooling below the liquidus temperature of the mantle melt until the basal magma ocean solidified (Labrosse, Hernlund, et al., 2007). Discovering whether a global magnetic field existed throughout the Archean and Hadean would provide critical constraints on these processes.

Limitations of our modeling approach

Using one-dimensional scaling laws to describe the coupled evolution of Earth's core and mantle is computationally efficient and allows for rapid sensitivity tests and description of first-order phenomena (e.g., Stevenson et al., 1983; Christensen, 1985). Future work, however, should address some shortcomings of our approach. Parameterizations of core energetics coupled to fully dynamical simulations of the mantle (e.g., Nakagawa and Tackley, 2010) should include precipitation of magnesium-bearing minerals. If CMB heat flow is sub-adiabatic and no compositional buoyancy is available (e.g., before the nucleation of the inner core absent precipitation), then additional equations are required to model the dynamics in the presence of a thick, stable layer at the top of the core since only part of the outer core would vigorously convect (e.g., Labrosse, 2015). We have neglected this complication because such scenarios are probably not compatible with the observed longevity of the global magnetic field.

More importantly, the CMB is both spatially and temporally heterogeneous in terms of composition and temperature. The stagnant layer in our models condenses vertical and lateral variations such as the post-perovskite phase transition and double-crossings, along with regions like large low-shear-wave-velocity provinces and ultralow-velocity zones (e.g., Hernlund and McNamara, 2015). The spatial variability of CMB heat flow caused by cold slabs, in particular, may control the timing of geomagnetic reversals (e.g., Olson et al., 2013). Fluid motions asso-

ciated with baroclinic instability can drive lateral transport of heat and assist the operation of a dynamo. The associated entropy production, however, is likely small because the effective temperature of dissipation is close to that of the CMB, reducing its Carnot-like efficiency (e.g., Labrosse, 2015). Thus, we have not included any parameterization of this process.

Implications for Venus

Spacecraft have constrained the magnetic moment on Venus to less than 10^{-5} times the terrestrial value (Phillips and Russell, 1987). Although its moment of inertia is presently unknown, assuming that Venus has an iron-rich core like Earth seems reasonable. Thermal evolution models imply that the core of Venus would not have frozen completely solid (e.g., Stevenson et al., 1983), but convection must have ceased in the liquid portion for some reason. Jacobson et al. (2015) proposed that Venus did not suffer a giant impact, in which case a stable stratification would develop as the concentration of light elements in material added to the top of the core increased with pressure/temperature conditions during accretion. No giant impact also means no magnesium to precipitate and provide energy and entropy for the dynamo. Future work should consider estimates of the CMB heat flow from, for example, thermal evolution models (e.g., Nimmo, 2002; O'Rourke and Korenaga, 2015) and the buoyancy flux of mantle plumes (e.g., Smrekar and Sotin, 2012). Estimates above the critical value required to drive a dynamo in a mostly isentropic and homogeneous core would serve as evidence that the core of Venus was indeed initially stratified.

3.6 Conclusions

Simple scalings for mantle dynamics, along with a parametrized model for the energetics of the core, allow us to estimate how much entropy has been available to sustain a dynamo throughout geologic time. If the recent upward revision of the thermal conductivity of the core is correct, then the precipitation of magnesium-bearing minerals at rates suggested by O'Rourke and Stevenson (2016) and Badro, Siebert, et al. (2016) allows vigorous convection prior to the nucleation of the inner core for most combinations of initial conditions. Ongoing precipitation would produce positive rates of entropy production for at least 3.45 Gyr as long as the abundance of potassium is under ~ 200 ppm and the present-day CMB heat flow is above ~ 5 TW. Because the minimum required heat flow across the core/mantle boundary remains roughly constant, the longevity of the magnetic field is compatible

with a weak dependence of mantle heat flow on temperature. Precipitation may yield roughly constant rates of entropy production over time, meaning that inner core's formation may not create a dramatic increase in field strength preserved in the paleomagnetic record. Similar computational exercises are relevant to Venus and probably differentiated "super-Earth" exoplanets.

*Chapter 4***INTERPRETING THE SPATIAL DISTRIBUTION OF
VOLCANICALLY MODIFIED CRATERS ON VENUS****4.1 Abstract**

To understand the impact cratering record on Venus, we investigate two distinct resurfacing styles: localized, thin flows and large shield volcanoes. We statistically analyze the size-frequency distribution of volcanically modified craters and, using Monte Carlo simulations, their spatial distribution. Lava flows partially fill most craters, darkening their floors in radar images. We find that a model featuring localized, thin flows occurring throughout geologic time predicts their observed distribution. Individual flows may be morphologically indistinguishable, but combined they cover large provinces. Recent mantle plumes may drive a small amount of hotspot magmatism that produces the observed clusters of large shield volcanoes and obviously embayed craters. Ultimately, our analysis demonstrates that two styles of volcanism are needed to explain the observed properties of impact craters, and that catastrophic resurfacing is not required.

4.2 Introduction

Venus and Earth are terrestrial planets with similar sizes, densities, and positions in the Solar System. They are usually assumed to have similar bulk compositions, too (e.g., Namiki and Solomon, 1998). But Earth is clement, whereas greenhouse gases have raised surface temperatures on Venus to ~ 740 K (e.g., Bullock and Grinspoon, 2001). Differences in the mantle dynamics between these planets mirror, and probably explain, their distinctive surface conditions. On Earth, plate tectonics recycles surface material, concentrates volcanism near spreading centers and subduction zones, and sustains habitability (e.g., Korenaga, 2012). Venus, in contrast, currently operates in the stagnant-lid regime—the mode of mantle convection found on every terrestrial planet except Earth (e.g., Solomatov, 1996; Solomatov and Moresi, 2000)—where solid-state convection occurs below an unbroken, planet-encompassing lithosphere. Beyond this simple description of its present state, the history of Venus is vigorously debated.

A global stratigraphy for the surface of Venus has been proposed, corresponding to a so-called “directional” evolution. Spatially disparate terrains are grouped into

global units based on morphologic similarities (e.g., Basilevsky and Head, 1998; Basilevsky and Head, 2000; Basilevsky and Head, 2002; Ivanov and Head, 2011; Ivanov and Head, 2013). A relative age is assigned to each unit with crater counting, which relies on virtually all craters residing atop the local stratigraphy. Each unit is then attributed to volcanic and/or tectonic processes. The key feature of the directional history is that these processes are global and basically confined to the time period that their associated units represent. For example, global tectonism is interpreted to have shaped the oldest tessera terrain and heavily tectonized volcanic plains, but its intensity quickly diminished during the formation of the younger volcanic plains. Transitions between different global processes are rapid in this history. The emplacement of volcanic plains and features covering most of Venus, in particular, is proposed to have lasted ~ 100 Myr, less than half of the mean surface age (e.g., Schaber et al., 1992). Several geophysical explanations have emerged for this catastrophic resurfacing event (e.g., Turcotte, 1993; Moresi and Solomatov, 1998; Reese, Solomatov, and Moresi, 1999; Armann and Tackley, 2012).

Countervailing evidence suggests that the surface evolution of Venus was likely more complex. New mapping efforts indicate that large areas preserve an ancient history that records the effects of localized resurfacing processes that operated throughout geologic time (e.g., Guest and Stofan, 1999; Stofan, Brian, et al., 2005; Hansen and Lopez, 2010). Similar-looking terrains scattered across Venus are not always temporally correlated (e.g., Guest and Stofan, 1999). Feedback between atmospheric conditions and interior dynamics might cause localized resurfacing and strong variations in surface age (Noack et al., 2012). Without the necessity of catastrophic resurfacing, modelers might also stick to the simplest story for mantle dynamics—continual evolution in the stagnant-lid regime, which is most natural for terrestrial planets lacking surface water (e.g., Solomatov, 1995; Korenaga, 2010a; O'Rourke and Korenaga, 2012).

Observations of impact craters constrain the geologic history of Venus. In the early 1990s, synthetic aperture radar images from NASA's Magellan mission, covering $\sim 98\%$ of the surface, revealed ~ 1000 craters (Phillips, Raubertas, et al., 1992; Schaber et al., 1992). Considering the abundance of likely impactors and the strength of atmospheric screening, the effective mean surface age is ~ 300 Myr – 1 Gyr (McKinnon et al., 1997). Slow winds and the absence of surface water preclude the erosion of craters, although eolian processes may degrade associated features like dark haloes and parabolic ejecta deposits over time (Izenberg et al.,

1994; Basilevsky and Head, 2002). Only a small percentage (<10%) of the extant craters are obviously embayed by external lava flows that breach their rims or cover a large portion of their ejecta blankets (Schaber et al., 1992; Phillips, Raubertas, et al., 1992; Strom et al., 1994; Collins et al., 1999). Coupled with the apparent statistical randomness of the coordinates of craters, this observation was initially seen as strong evidence for catastrophic resurfacing and a relatively young, superimposed crater population. Adherents to catastrophic resurfacing invoke $\sim 0.01\text{--}0.15 \text{ km}^3/\text{yr}$ of subsequent, more recent volcanism to explain the obviously embayed craters (e.g., Strom et al., 1994).

However, there are challenges to this paradigm. Crater locations are not necessarily random with respect to geology (e.g., Hauck, Phillips, and Price, 1998) or topography (e.g., Herrick and Phillips, 1994). Localized resurfacing events that occur frequently over several Gyr can also yield an overall spatial distribution that looks random (e.g., Phillips, Raubertas, et al., 1992). Bjonnes et al. (2012) produced a low number of embayed craters in Monte Carlo simulations featuring shield volcanoes—but did not investigate their spatial distribution. They assumed that all craters not obviously embayed in Magellan imagery are pristine.

A growing body of evidence suggests that thin, morphologically indistinguishable lava flows have filled the radar-dark craters, which comprise $\sim 80\%$ of the total population. The floors of these craters have low radar backscatter relative to their ejecta blankets and rims—they thus resemble the volcanic plains. Neither impact melting nor eolian processes fully account for their morphological differences with the bright-floored craters, which appear truly pristine (Wichman, 1999; Herrick and Sharpton, 2000; Herrick and Rumpf, 2011). In particular, dark-floored craters have systematically shallower rim-floor depths and rim heights than bright-floored craters, implying partial filling of these craters and flooding of their surroundings. Additionally, virtually all dark-floored craters with $D > 20 \text{ km}$ and dark halos surrounding continuous ejecta have had a portion of their dark halo removed (Herrick and Rumpf, 2011). Ivanov and Head (2013) compared the possible magmatic filling of dark-floored craters to the subtle embayment by mare material of Lichtenberg, a rayed crater on the Moon (Schultz and Spudis, 1983). Interior floor volcanism may also contribute to crater filling. Age estimates that underlie the directional stratigraphy are invalid if most craters suffered post-impact volcanic modification. Until now, no study has attempted to simulate the volcanic modification of dark-floored craters.

Here, we test two non-catastrophic models for volcanic processes: thin, low viscosity flows and large shield volcanoes. We compare predictions for the spatial and size-frequency distributions of volcanically modified craters against observations. We find that no single process can explain the cratering record, but thin flows are likely responsible for most magmatism. This implies that catastrophic resurfacing need not be invoked; rather, stagnant-lid convection fed localized volcanism continuously throughout time.

4.3 Crater classifications and size-frequency distributions

Two different databases of impact craters are available, hosted by the Lunar and Planetary Institute (LPI) (Herrick, Sharpton, et al., 1997) and the USGS Astrogeology Branch (Schaber et al., 1992; Strom et al., 1994). We primarily rely on the LPI database, which contains detailed, quantitative descriptions of crater morphology and does not bias its classifications with assumptions about the geologic history of Venus. Figure 4.1 contains our map of impact craters. We are interested in the location, diameter, floor reflectivity, and any obvious embayment by external lava flows of each crater. Out of 933, 748 (~80%, filled symbols) are classified as dark-floored and the remaining 185 (~20%, unfilled symbols) are radar-bright. Only 86 craters (~9%, red symbols) show unequivocal signs of external embayment. Merely 6 obviously embayed craters also have radar-bright floors.

Eleven craters are incompletely described in the LPI database because of gaps in the Magellan imagery of their floors and rims. Following the USGS database, we classify the craters Ellen and Orlova as dark-floored and, respectively, as obviously embayed and not. We exclude the remaining 9 craters from our analysis. We also analyze the distribution of 56 (~6%) obviously embayed craters in the USGS database. However, only 32 of these craters are similarly classified in the LPI database. The rest do not have distinct breaches in their rims or ejecta blankets, and some small craters are omitted entirely.

A complex interplay between the impactor population, atmospheric screening, and volcanic modification creates the modern size-frequency distribution of craters. Overall, observed diameters range from ~1.5–268.7 km, with a median of 14.5 km. Larger craters are deeper, as seen in Panel B of Fig. 4.1, which contains formulas for the rim-floor depths of dark- and bright- floored craters (d_{df} and d_{bf} , respectively) that were fit to topographic profiles of 91 craters with $D > 15$ km (Herrick and Rumpf, 2011). Volcanically modified craters tend to be larger than unmodified

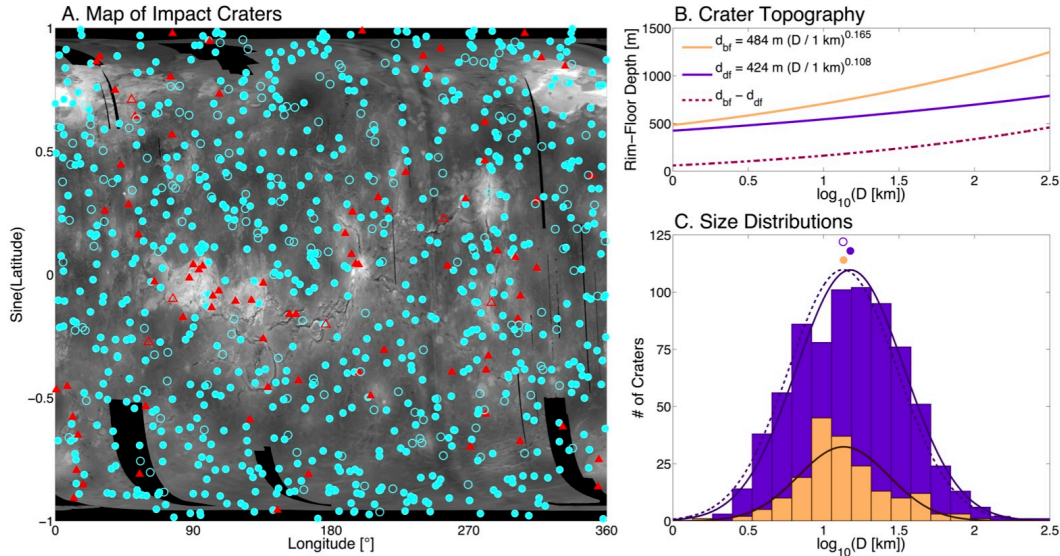


Figure 4.1: Panel A: Map of impact craters on Venus based on the LPI database (Herrick, Sharpton, et al., 1997). Locations of 933 craters are plotted over the available Magellan topography (elevated terrain is brighter). The 847 craters without exterior volcanic embayment are blue circles, whereas the 86 embayed craters are red triangles. Filled symbols represent the 748 craters with radar-dark floors, whereas symbols for the 185 bright-floored craters are unfilled. Panel B: Best-fit formulas from Herrick and Rumpf (2011) for the rim-floor depths of bright-floored (d_{bf}) and dark-floored (d_{df}) craters and their difference. Panel C: Histograms showing the distributions of the diameters of dark-floored (purple) and bright-floored (orange) craters, along with their best-fit normal probability density functions (pdfs, solid curves). The dashed, purple curve is a pdf that approximates the size-frequency distribution of craters that were volcanically modified to produce the dark-floored ones (inferred as discussed in Section 4). The mean value of this pdf (empty, purple circle) is nearly identical to the average diameter of the bright-floored craters.

ones. Craters that are and are not obviously embayed have median diameters of 23.6 and 20.2 km, respectively. Likewise, the median diameter of dark-floored craters is 21.3 km, compared to 17.6 km for the bright-floored ones. Panel C in Fig. 4.1 shows the two size-frequency distributions (histograms), along with best-fit log-normal probability density functions (pdfs, solid curves). The best-fit parameters in log space are $\mu_b = 1.133$ and $\sigma_b = 0.3$ for bright-floored craters and $\mu_d = 1.178$ and $\sigma_d = 0.358$ for dark-floored craters. We assessed uncertainties on these distributions using standard bootstrap Monte Carlo resampling, yielding errors on the mean log-diameters of 0.006 and 0.004, respectively, compared to $\mu_d - \mu_b = 0.045$. Thus, the difference between these two pdfs is statistically significant.

4.4 Quantifying randomness of spatial distributions

We analyze the populations of craters on Venus using nearest neighbor distances (Hauck, Phillips, and Price, 1998). This method is more sensitive than chi-squared tests on coordinates and intercrater angles. Given coordinates for N craters, we can calculate sets of angular distances between each crater and its M th nearest neighbors. As noted by Scott and Tout (1989), the pdf for randomly distributed craters is given by

$$p(\theta|N, M) = \frac{(N-1)!}{2^{N-1}(N-M-1)!(M-1)!} \sin(\theta)[1-\cos(\theta)]^{M-1}[1+\cos(\theta)]^{N-M-1}, \quad (4.1)$$

where $\theta \in [0, \pi]$. Hauck, Phillips, and Price (1998) used a pdf for the $M = 1$ case based on modeling the spatial crater distribution as a Poisson process describing points placed randomly on a plane, but their formula diverges slightly from the correct pdf for $N < 10^3$ because of the difference between arc and chord lengths. We calculate the first and second moments of the above pdf, representing the expected mean angular distance and its corresponding standard deviation, μ_{exp} and σ_{exp} , respectively. We then compare the expected value to the observed mean angular distance for the true crater population, μ_{obs} , using the normalized test statistic (Hauck, Phillips, and Price, 1998):

$$z = \frac{\mu_{exp} - \mu_{obs}}{\sigma_{exp}}. \quad (4.2)$$

For a perfectly random distribution, $z = 0$, reflecting points that show a small random degree of clustering. Distributions with values of $z < 0$ or $z > 0$ reflect under- or over-clustering of points, respectively.

We explored the spatial distributions of dark- and bright-floored craters, along with obviously embayed craters from both databases. The z -statistic values for each population with $M = 1, 3,$ and 6 were calculated and are shown as dashed, vertical lines in Figure 4.2. For comparison, we computed distributions of z with 10^5 random placements of points on a sphere (grey histograms in Figure 4.2). At each value of M , we calculated one-sided p -values to test the hypothesis of random spatial distribution for each population, where values of $p \leq 0.01$ – 0.05 are considered sufficiently unlikely to reject the corresponding null hypothesis.

We find that the distributions of dark- and bright-floored craters are compatible with randomness (shown by comfortably large p -values), although bright-floored craters perhaps indicate some degree of clustering for $M \geq 3$. Obviously embayed craters

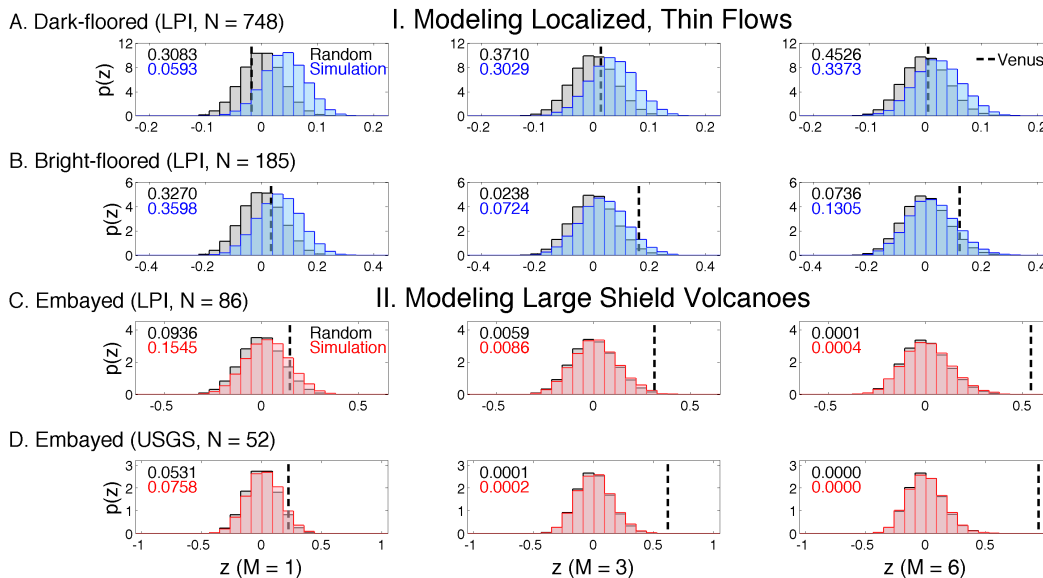


Figure 4.2: Comparisons of test statistics representing the distributions of four populations of craters (vertical, dashed lines) to distributions of test statistics associated with 10^5 sets of randomly distributed points (grey histograms) and 10^4 simulations (colored histograms). From left to right, each column shows values of z for $M = 1, 3,$ and 6 . One-sided p -values for testing the hypotheses that the spatial distributions on Venus are random (black, upper) or result from the simulated processes (colored, lower) are reported in the top, left corner of each plot. Simulations of resurfacing by thin flows (blue histograms) successfully reproduce the distributions of the dark-floored (row A) and bright-floored (row B) craters in the LPI database. Simulations in which large shield volcanoes are produced everywhere on Venus with equal probability (red histograms) fail to reproduce the clustering of obviously embayed craters in both the LPI (row C) and USGS (row D) databases.

are consistent with random distributions for $M = 1$, but are unambiguously clustered for $M \geq 3$, as shown in the lower half of Figure 4.1. Those in the LPI database are slightly less clustered than those in the USGS database, which includes very few obviously embayed craters on volcanic plains.

4.5 Modeling localized, thin flows on Venus

We test whether localized resurfacing can reproduce the observed cratering record using Monte Carlo simulations. Computational and conceptual expedience mandate several simplifying assumptions. In particular, we assume equal diameters for all craters and model cratering as a Poisson process that occurs everywhere on the surface with equal probability. We simulate cratering events with an exponential distribution, using a time constant, τ_c , that is fixed for the total duration of each

simulation, T . Likewise, we model resurfacing events as a Poisson process with another time constant, τ_r . We use $T = 3.0$ Gyr for all simulations, although we obtain consistent results for $T \leq 4.5$ Gyr. Assumptions of constant rates for cratering and resurfacing are ill-suited to early Venus, which endured giant impacts, a solidifying magma ocean, and the Late Heavy Bombardment (e.g., Agnor et al., 1999; Solomatov and Moresi, 2000). Nevertheless, the resulting distributions are somewhat insensitive to this simplification because more recent resurfacing has erased the surface record of this ancient period.

Using the general simulation method described above, we explore a number of resurfacing models to determine how well they can reproduce the observed crater distributions. Our first task is to investigate whether localized, thin flows can reproduce the populations of dark- and bright-floored craters. We developed a simple model for this type of magmatism, shown in the left side of Figure 4.3. Here, craters within R_p of the center of the resurfacing event are partially filled and should have radar-dark floors. Lava can breach crater rims on short length scales or emerge from fractures on crater floors. Once filled X times, craters are completely buried and thus erased from the surface record. Craters that were never partially filled should appear radar-bright today. Figure 4.3 contains examples of each type of crater. Each lava flow covers a fraction of the surface, $\alpha = 0.25(R_p/R_V)^2$, where $R_V \approx 6052$ km is the radius of Venus. For $X = 5$, implied flow depths are ~ 150 m. We model each flow as one instantaneous event but, in reality, multiple smaller flows from a single source region could combine over a few Myr. With the initial condition of zero craters at the start of each simulation, we calculate the expected number of craters that have experienced x resurfacing events by solving a system of differential equations:

$$\frac{dN_0(t)}{dt} = \frac{1}{\tau_c} - \frac{\alpha N_0(t)}{\tau_r} \quad (4.3)$$

$$\frac{dN_x(t)}{dt} = \frac{\alpha}{\tau_r} [N_{x-1}(t) - N_x(t)], \quad (4.4)$$

where $0 < x < X$. Specifically, we can calculate the expected number of bright-floored craters as a function of time, defined as those that have experienced no resurfacing events ($x = 0$):

$$N_b(t) = \frac{\tau_r}{\alpha \tau_c} \left[1 - \exp\left(-\frac{\alpha t}{\tau_r}\right) \right]. \quad (4.5)$$

Likewise, we can predict how many craters have experienced $x > 0$ partial resur-

facing events:

$$N_x(t) = N_b(t) - \left\{ \sum_{i=1}^x \left[\frac{\alpha^{(i-1)} t^i}{i! \tau_r^{(i-1)} \tau_c^i} \right] \right\} \exp\left(-\frac{\alpha t}{\tau_r}\right). \quad (4.6)$$

The total number of dark-floored craters is given simply by $N_d(t) = N_1(t) + \dots + N_{X-1}(t)$. For realistic evolution times of ~ 3 Gyr, $t \gg \tau_r/\alpha$ and thus the simulation reaches equilibrium with $N_x = N_b$ and $N_d/N_b = X - 1$. We can therefore predict the expected number of bright- and dark-floored craters that will remain at the end of a simulation for any choice of X , R_p , τ_r , and τ_c . We used $\tau_c = 1$ Myr/event, well within the range of plausible estimates (McKinnon et al., 1997). With this cratering rate, a catastrophically resurfaced Venus would have a mean surface age of 933 Myr. A larger or smaller τ_c simply implies that τ_r should proportionally increase or decrease to maintain the observed number of craters. We tested several pairs of values for α and τ_r .

Representative results from 10^4 simulations are plotted as blue histograms in Figure 4.2. In this case, we set $X = 5$, $\tau_r = 0.1$ Myr/event, and $R_p = 280$ km ($\alpha = 10^{-3.27}$), which yields $N_b(T) = 187 \pm 18$ and $N_d(T) = 744 \pm 28$. All p -values are >0.05 , meaning that the observed distribution of dark- and bright-floored craters represents a statistically plausible outcome of our model. The mean age of craters that survive to the present is 562 Myr, but craters as old as ~ 2 Gyr occasionally survive. The mean age of the most recent partial fillings of each dark-floored crater is 190 Myr. So, although much of the surface is young within this model, Venus should preserve an ancient history in many locations. Bright-floored craters should have a variety of ages, consistent with the observation that some bright-floored craters (presumably the younger ones) have parabolic deposits, while many others do not (e.g., Herrick, Sharpton, et al., 1997).

The suitability of this resurfacing model is largely insensitive to our choice of simulation parameters. Specifically, we obtained consistent results for $\tau_r \leq 1.5$ Myr/event and corresponding $R_p \leq 1079$ km ($\alpha \leq 10^{-2.1}$). For $X \leq 4$, the fraction of bright-floored craters increases beyond what is currently observed, but simulations still reproduce the observed distributions of dark- and bright-floored craters. As τ_r increases, both groups of craters become increasingly clustered. That is, p -values for the bright-floored craters increase (to >0.3), but the match to the $M = 1$ case for dark-floored craters worsens.

We considered whether this model is consistent with the differences between the size-frequency distributions of dark- and bright-floored craters. The probability of

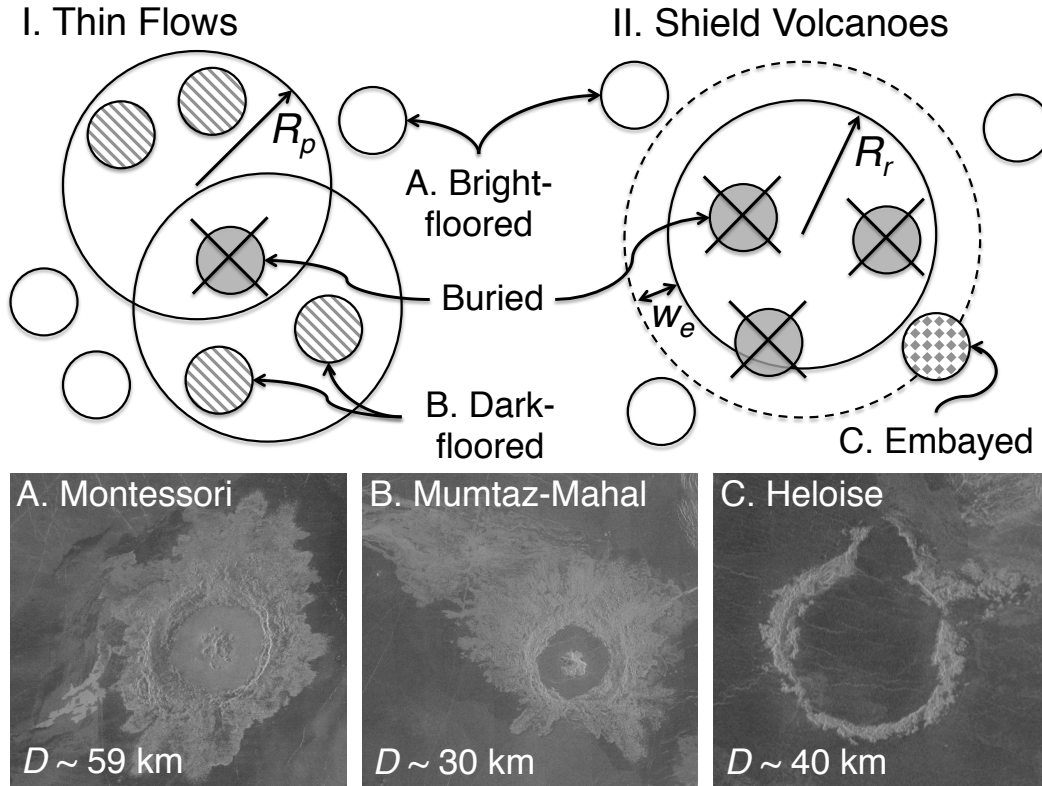


Figure 4.3: Cartoons of our two models of volcanic resurfacing events and Magellan radar images of representative craters. Initially, craters are bright-floored and pristine like Montessori. Thin, low viscosity flows (left) partially bury craters within a radius R_p , which become dark-floored like Mumtaz-Mahal. Craters that are filled X times are completely buried. In this cartoon, $X = 2$, but we ran simulations with $X = 2-5$. Large shield volcanos (right) completely bury all impact craters within a radius R_r . Craters on the outskirts, in an annulus of width w_e , are partially embayed like Heloise.

observing a crater with diameter D is $p(D) = p(D|I, A)p(D|V)$, where $p(D|I, A)$ is the probability of crater production given the impactor population and the effects of atmospheric screening, represented by I and A , respectively. In this model, the probability that a produced crater escapes complete volcanic burial until the present is directly proportional to its original depth, $p(D|V) \propto d(D)$. Diameter is only important to survival insofar as it predicts depth because it is much smaller than the length scale of a typical flow. Assuming that all craters were originally as deep as the bright-floored ones are today, we can approximate the diameter-depth relation, $d(D) \sim d_{bf}(D)$. We calculated the initial size-frequency distribution of craters that were modified to produce the observed dark-floored craters, $p_d(D|I, A) \propto p_d(D)/d_{bf}(D)$, where $p_d(D)$ is the pdf associated with the

size-frequency distribution of dark-floored craters. We plotted $p_d(D|I, A)$, renormalized, as a dashed, purple curve in Panel C of Figure 4.1. This derived pdf has a mean value that agrees with that of the bright-floored craters to within derived uncertainties, i.e., $\Delta\mu < 0.004$. The size-frequency distribution of impactors and the efficiency of atmospheric screening may have varied over Venus history; nevertheless, this correspondence suggests that the dark-floored craters derived from a population like the bright-floored craters, modified by a depth-dependent process like thin flows.

4.6 Shield volcanoes and clustering of embayed craters

Simulations of the evolution of the surface of Venus usually only consider volcanic modification of obviously embayed craters by large shield volcanoes. The right side of Figure 4.3 is a cartoon of the model used in previous Monte Carlo simulations (e.g., Strom et al., 1994; Bjonnes et al., 2012). Craters are completely obliterated within a circular patch of radius R_r , which covers a fraction of the surface, $\alpha = 0.25(R_r/R_V)^2$. Within the external annulus of width w_e , craters are partially embayed. If we again assume that cratering and resurfacing are Poisson processes that occur everywhere on the surface with equal probability, then the expected number of craters exposed on the surface as a function of time, $N(t)$, equals $N_b(t)$ from Equation 4.5. This model becomes degenerate with our model for thin-flow magmatism in the case that $X = 1$, $R_r \rightarrow 0$, and $w_e \rightarrow R_p$, but represents a distinct volcanic process in which a single source of magma feeds the growth of a shield volcano that is identifiable in the Magellan imagery.

Strom et al. (1994) claimed that any non-catastrophic model must use extremely low values of α ($\leq 3 \times 10^{-4}$) because they believed that Venus lacks volcanic features covering 0.03–10% of the surface (Head et al., 1992; Crumpler et al., 1997). They argued that such models inevitably produce too many embayed craters. However, mappers might mistakenly lump several distinct lava flows together as one based on the available data, lacking mineralogical information or high-resolution imagery. Bjonnes et al. (2012) found that non-catastrophic models using larger resurfacing patches ($\alpha = 0.001$ – 0.01) can produce a random-looking distribution of craters with a low number of partially embayed craters.

Tuning this model to obtain the observed number of embayed craters is easy, provided that the external annulus w_e is sufficiently small. However, some values of w_e are perhaps more physically plausible than others. Bjonnes et al. (2012) used the

median diameter of observed craters (~ 15 km), while Strom et al. (1994) used the observed diameters of craters as a distribution of values for w_e . Other authors model volcanoes as pyramids with slopes $\sim 0.2\text{--}2.0^\circ$ (e.g., Romeo, 2013). A typical crater with diameter $D = 15$ km might have a rim-floor depth of ~ 750 m and a rim height of ~ 210 m (Herrick and Rumpf, 2011). In this scenario, $w_e \sim 15\text{--}150$ km is the region where lava is thick enough to flow over the rim but too thin to completely fill the crater and bury the rim. Larger craters are more likely to intersect this region, so it is not surprising that obviously embayed craters tend to be larger than average.

Resurfacing models featuring only large shield volcanoes, however, always fail to reproduce the observed clustering of embayed craters on Venus. We performed simulations using virtually the same parameters as Bjonnes et al. (2012). Specifically, we set $\tau_c = 1$ Myr/event and $\alpha = 10^{-3}$. We found that $\tau_r = 0.9898$ Myr/event produces $N(T) = 942 \pm 36$. We ran two sets of 10^4 simulations each for $w_e = 13.9$ and 21.8 km, which yield 56 ± 8 and 86 ± 9 embayed craters, respectively, for comparison to the LPI and USGS databases. Our results are plotted as red histograms in Figure 4.2. These simulations predict a random distribution of obviously embayed craters, which is incompatible with reality. Large shield volcanoes can only produce the observed clustering if they are restricted to a few regions on Venus.

Our conclusion here is again insensitive to our choice of simulation parameters. In particular, we tested different values of T and the extreme case where resurfacing is halted ~ 1.5 Gyr before the end of the simulations, which allows the overall distribution to look random for $\alpha \leq 10^{-2}$ (Bjonnes et al., 2012). But we found that embayed craters are always insufficiently clustered ($p < 10^{-3}$ for $M = 6$). Obviously embayed craters are found on only $\sim 30\%$ of the surface, with a $\sim 10\%$ reduction in the local crater density, meaning that associated magmatism only represents $\sim 3\%$ of the total—reflecting a possibly distinct qualitative origin that nevertheless remains quantitatively minor in the grand scheme of the cratering record.

4.7 Discussion

Stagnant-lid convection involves two primary sources of magmatism that may correspond to our two models of resurfacing processes. Over time, mantle material rises to replace cold, sinking lithosphere. Pressure-release melting of this passively upwelling mantle could cause localized, thin flows on the surface, although the nature of extrusive volcanism related to this process requires further investigation (e.g., Phillips and Hansen, 1994; Reese, Solomatov, and Orth, 2007). Plate tectonics

concentrates pressure-release melting at spreading centers, but passive upwellings are widespread under stagnant lids, supporting our assumption of spatial uniformity for this type of resurfacing (e.g., Solomatov and Moresi, 2000; Armann and Tackley, 2012; Noack et al., 2012). Localized mobilization of near-surface lithosphere during periods of extremely high surface temperatures is an alternative source of these flows (Noack et al., 2012).

Large shield volcanoes are possibly related to mantle plumes, particularly in areas that resemble terrestrial hotspots like Hawaii (e.g., Smrekar, Stofan, et al., 2010). Anomalously hot material rising from the core/mantle boundary drives a few (~9) plumes on Venus that are likely responsible for large volcanic rises, young flows, and associated emissivity anomalies (Smrekar, Stofan, et al., 2010; Smrekar and Sotin, 2012). Stagnant-lid convection is inefficient compared to plate tectonics, so a well-insulated mantle may initially limit core cooling. Passive upwelling may have produced more magmatism on Mars than mantle plumes until ~1–2 Ga (Weizman et al., 2001). Likewise, plumes inside Venus are perhaps a recent phenomenon, whereas magmatism from passive upwelling has continued throughout geologic time. The duration and dynamics of plume activity, however, are sensitive to poorly determined properties of the interior of Venus (e.g., Smrekar and Sotin, 2012).

Higher resolution imagery and topography are required to better constrain our models. For example, we predict that dark-floored craters exhibit a wide spectrum of rim-floor depths and rim heights, implying degrees of volcanic flooding ranging from negligible to nearly complete. Analysis of the limited sample of craters with stereo-derived topography suggests but does not confirm this hypothesis (Herrick and Rumpf, 2011). There is a well-known correlation between the locations of obviously embayed craters and large volcanic edifices, particularly in the Beta-Atla-Themis region (e.g., Herrick and Phillips, 1994; Strom et al., 1994; Crumpler et al., 1997). Future data and mapping, however, might reveal that some obviously embayed craters are associated with other processes like multiple thin flows, instead of shield volcanoes. Most dark-floored craters are located on the plains, which generally lack obvious volcanic sources (e.g., Ivanov and Head, 2013).

4.8 Conclusions

Early studies of the cratering record on Venus birthed the catastrophic resurfacing hypothesis, bolstered later by the directional stratigraphic history. But new evidence that the dark-floored craters have suffered post-impact volcanic modification poten-

tially violates the fundamental assumption made by those initial investigations that most craters on Venus are pristine. Our Monte Carlo simulations demonstrate that two types of non-catastrophic volcanism can explain the observed cratering record. We reproduce the modern spatial and size-frequency distributions of dark-floored craters using a model featuring thin, morphologically similar flows that escape from vents spread over a wide area and penetrate rims at short length scales or fill craters from vents that open on their floors. Large shield volcanoes associated with a limited amount of hotspot magmatism or another geologic process are possibly responsible for the clustered population of obviously embayed craters. Improved imagery and topography are required to definitively link modified craters to volcanic sources.

*Chapter 5***SIGNATURES OF LITHOSPHERIC FLEXURE IN STEREO
TOPOGRAPHY AT CORONAE ON VENUS****5.1 Abstract**

Signatures of lithospheric flexure were previously identified around several large coronae on Venus. Thin plate models fit to topographic profiles return the elastic parameters, allowing derivation of mechanical thickness and thermal gradients given an assumed yield strength envelope. However, the low resolution of altimetry data from the NASA Magellan mission has precluded their application to the vast majority of coronae, particularly those with diameters less than a few hundred kilometers. Here we search for flexural signatures around 99 coronae in the stereo topographic dataset that was recently assembled from synthetic aperture radar images covering ~20% of the surface. We derive elastic thicknesses of ~1.5 to 37 km with Cartesian and axisymmetric models at 22 coronae, corresponding to mechanical thicknesses and temperature gradients ranging from ~2 to 64 km and ~4 to 118 K km⁻¹, respectively. Implied surface heat flows are more than double the global averages predicted by most thermal evolution models. Using binomial statistics, we suggest that “Type 2” coronae with incomplete fracture annuli are less likely to host flexural signatures than “Type 1” coronae with more complete annuli, although a planet-wide survey is required for robust inferences. We discuss the implications of low (<5–10 km) elastic thickness that were also noted in previous gravity studies. Flexural parameters do not vary systematically as a function of coronae type, geologic setting, or topographic class in our limited sample. Obtaining quality, high-resolution topography for the entire surface of Venus is vital to verifying our conclusions.

5.2 Introduction

Coronae are enigmatic, quasi-circular features found only on Venus among the terrestrial planets in our solar system. Rings of concentric fractures ranging in diameter from ~60 to >1000 km are their primary distinguishing features (Barsukov et al., 1986). These fractures are superimposed on various complex morphologies and associated with at least small-scale volcanism (e.g., Stofan, Sharpton, et al., 1992; Smrekar and Stofan, 1997). Coronae are preferentially located near chasmata or fracture belts, not randomly distributed on the surface like impact craters (e.g.,

Stofan, Sharpton, et al., 1992; Squyres et al., 1993). But at least some coronae are found in every geologic environment including topographic rises, volcanic plains, and tessera terrain (e.g., Glaze et al., 2002). So-called “Type 2” coronae, comprising ~20% of the >500 total, have been identified with arcs of fractures extending less than 180° but possibly complete topographic rims, signifying both brittle and ductile deformation (e.g., Stofan, Smrekar, Tapper, et al., 2001). They are clearly different in appearance and more commonly isolated in the plains than most of the population, but their size distribution is statistically indistinguishable from the “Type 1” coronae with complete fracture annuli (Glaze et al., 2002). Although difficult to interpret, the complex properties of coronae are likely key to elucidating the unique rheology of the lithosphere on Venus.

Many modelers have attempted to reproduce the topographic profiles and gravity signatures observed at coronae. Upwelling mantle plumes or diapirs are a popular explanation for the abundance of elevated topography and extensional fractures in general, although such models differ considerably in detail (e.g., Stofan, Bind-schadler, et al., 1991; Janes et al., 1992; Koch and Manga, 1996; Smrekar and Stofan, 1997; Gerya, 2014). However, models with downwellings like Rayleigh-Taylor instabilities may also account for the gravity and topography data (e.g., Tackley and Stevenson, 1991; Hoogenboom and Houseman, 2006; Grindrod and Hoogenboom, 2006). Hybrid processes involving the interaction between a mantle plume and an adjacent, downwelling instability may have formed the coronae associated with large rifts (Piskorz et al., 2014). Both upwellings and downwellings are frequent occurrences with plate tectonics on Earth and in the stagnant-lid regime of mantle convection that may currently prevail within Venus (e.g., Solomatov and Moresi, 1996; O’Rourke and Korenaga, 2015) so multiple scenarios seem plausible. Deciding what subset of this myriad is compatible with all available observations, including the extent of fracturing and magmatism, will require additional simulations using modern software packages.

Coronae offer the opportunity to estimate the elastic thickness of the lithosphere, provided that flexure persists throughout geologic time and measurements are thus representative of the true values prior to their formation. Once constrained, the average elastic thickness may be used in global inversions of gravity and topography data for crustal thickness and dynamic support from the mantle (e.g., James et al., 2013). On Earth, simple elastic models correctly describe bending of the uppermost (≤ 30 km) lithosphere under loads from volcanic islands or at ocean trenches (e.g.,

Turcotte and Schubert, 2002). It is unclear whether to expect thinner or thicker elastic lithosphere on Venus because hotter temperatures weaken rocks, but the lack of water dramatically increases the strength of diabase (Mackwell et al., 1998). Comparatively large values ($\sim 35\text{--}70$ km) have been reported near the largest coronae like Artemis (e.g., Sandwell and Schubert, 1992; Johnson and Sandwell, 1994; Brown and Grimm, 1996), although moment saturation may limit the applicability of elastic plate models fit to topographic profiles at these locations (Phillips, Johnson, et al., 1997). In contrast, Earth-like thicknesses ($\sim 10\text{--}30$ km) have been derived through applying similar methods to the Freyja Montes deformation zone (Solomon and Head, 1990) and slightly smaller coronae (Sandwell and Schubert, 1992; Johnson and Sandwell, 1994). Noise in the available topographic data, however, has heretofore halted attempts to search for flexure at coronae with diameters less than the ~ 210 km average.

Estimates of elastic thickness obtained from modeling topography at coronae complement inferences from gravity data and other geologic features. For example, theoretical calculations indicate that volcanic edifices with steep, conical slopes are perhaps associated with thick elastic lithosphere, where flexural stresses allow the ascent of magma directly to the surface. In contrast, low elastic thicknesses may favor lateral transport of magma and thus the formation of dome-shaped edifices that are also seen on the surface (McGovern et al., 2013). Gravity surveys of coronae using admittance methods have likewise found elastic thicknesses ranging from $\sim 0\text{--}80$ km (Smrekar, Comstock, et al., 2003; Hoogenboom, Smrekar, et al., 2004; Hoogenboom, Houseman, and Martin, 2005). Both Type 1 and 2 coronae have elastic thicknesses spanning this range, regardless of whether they form on the plains or near fracture belts (Smrekar and Stofan, 2003). Coronae that formed after nearby chasmata are preferentially associated with thinner elastic lithosphere, although coronae that predate chasmata occasionally have small (≤ 5 km) elastic thickness as well (Hoogenboom, Houseman, and Martin, 2005). Near-zero thicknesses are thus associated with either formation on relatively warm and weak lithosphere or subsequent isostatic compensation and/or gravitational relaxation.

The purpose of this paper is to report on our search for flexural signatures around smaller coronae. We first discuss the newly available stereo topography that enables this investigation. Next, we explain our elastic plate models and the procedures for deriving related quantities. Before delving into the entire population of coronae with flexure, we present detailed analyses of four representative coronae. Finally,

we describe correlations between the prevalence and magnitude of flexure as functions of coronae type, size, topographic class, and geologic setting and discuss the implications for thermal histories.

5.3 Methods

Data

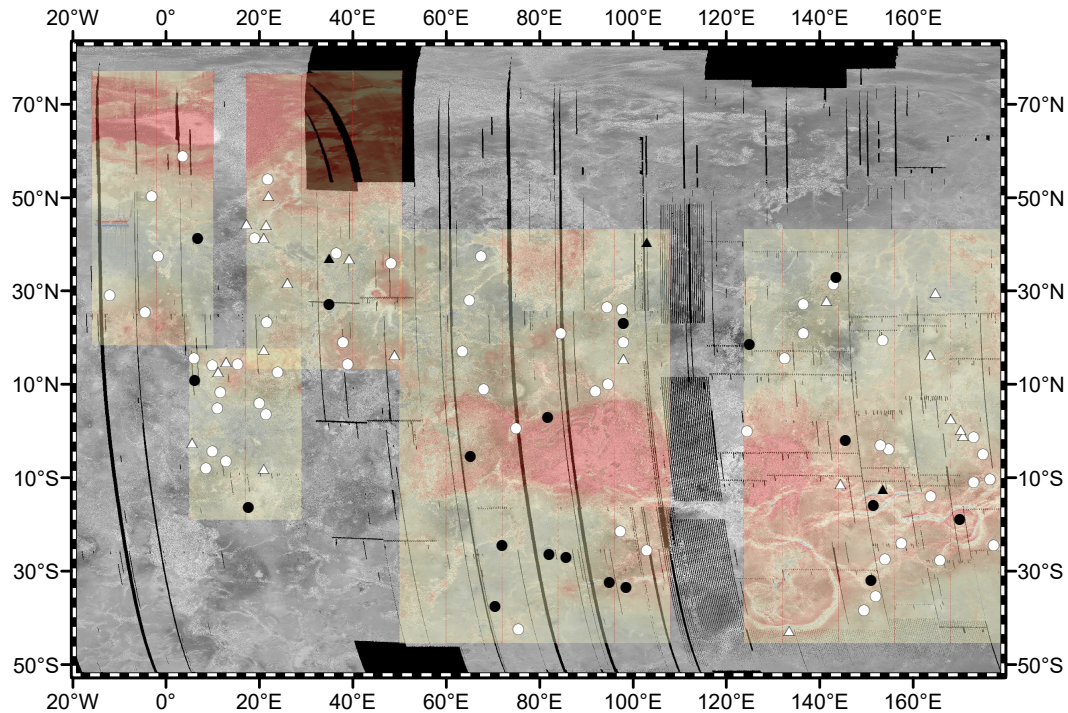


Figure 5.1: Mercator-projection map of the study area showing all available stereo topography in color (red is high, blue is low) overlaying greyscale SAR images from Cycle 1. Black and white symbols indicate the coordinates of coronae with and without flexural signatures, respectively. Type 1 coronae are denoted with circles, whereas triangles represent those classified as Type 2.

The NASA Magellan mission obtained synthetic aperture radar (SAR) images for nearly all (~98%) of the surface of Venus with a resolution of ~100–200 m (Saunders et al., 1992). Nearly 84% of the surface was mapped during the first Venusian day (Cycle 1) with east-facing or “left-looking” incidence angles. During Cycle 2 of the extended mission, Magellan first filled most of the gaps in the SAR coverage in right-looking geometry. Cycle 3 was dedicated to revisiting areas imaged in Cycle 1 with left-looking geometry but incidence angles adjusted by ~20° to produce stereo images. Unfortunately, emergent problems with the spacecraft limited stereo coverage to ~20% of the surface, mostly concentrated near the equator from 60–

180°E and 40°N to 40°S in partially non-contiguous swaths with numerous gaps (Herrick, Stahlke, et al., 2012).

Operating the radar dish in altimetry mode yielded a global topographic data record (GTDR) with a horizontal resolution of ~10–20 km and a maximum vertical resolution of ~50–100 m (Ford and Pettengill, 1992). Many features in the SAR imagery—some impact craters, volcanoes, and tectonic deformation associated with coronae—are not resolved in this coarse data set. Topography with nearly the same resolution as the imagery, however, is theoretically obtainable from the stereo SAR data. Using an automated matching routine, Herrick, Stahlke, et al. (2012) derived a new digital elevation model with a horizontal resolution of ~1 km, an order-of-magnitude improvement, from the overlapping coverage of Cycles 1 and 3. Gaps in stereo coverage are filled with GTDR data in this new, publicly accessible dataset, which has already motivated a reinterpretation of the impact cratering record (e.g., Herrick and Rumpf, 2011; O’Rourke, Wolf, et al., 2014).

Stereo-derived topography at least partially overlaps with 75 and 24 of the Type 1 and 2 coronae smaller than Artemis, respectively, identified in previous surveys of Magellan data (e.g., Stofan, Smrekar, Tapper, et al., 2001). Figure 5.1 shows the location of these coronae in the region of stereo coverage. First, we reconfirm the classification of each corona according to topographic shape (e.g., Smrekar and Stofan, 1997). We next describe the qualitative extent and type of associated volcanic features like small cones, pancake domes, and flows of various sizes. Finally, we extract topographic profiles that contain a relative low (e.g., a trench) interior to an external rise with smaller amplitude (e.g., Sandwell and Schubert, 1992; Johnson and Sandwell, 1994). Radial profiles are extracted so that topography is along the strike of concentric fractures that define each coronae as determined from the Magellan SAR imagery. Previous studies only used along-track profiles, which are not necessarily aligned with the coronae and potentially lead to overestimates of the elastic thickness by artificially elongating topography (e.g., Johnson and Sandwell, 1994).

Analytical models

Following previous studies, we consider two models of lithospheric flexure applicable to different plate geometries. Both are one-dimensional in that they describe topography as a function of distance along a single profile. Cartesian models feature simple analytic expressions for various parameters, but axisymmetric solutions are

arguably more realistic.

Cartesian geometry

The first model is applicable to a load and/or a bending moment applied to the end of a broken, elastic plate with Cartesian geometry. In this case, the elevation along a profile is (e.g., Johnson and Sandwell, 1994)

$$w(x) = \exp\left(-\frac{x}{\alpha_c}\right) \left[c_1 \cos\left(\frac{x}{\alpha_c}\right) + c_2 \sin\left(\frac{x}{\alpha_c}\right) \right] + s_r x + w_0, \quad (5.1)$$

where w is elevation, x is the distance along track from the position of the applied load and/or bending moment, s_r is the regional slope, and w_0 is a vertical offset. We assume that the load and/or bending moment are applied just before x_0 , the point of minimum elevation (bottom of the trench) in the topographic profiles. In other words, we normalize $x = d - x_0$, where d is the distance along our topographic profiles. Each profile begins with $d = 0$ m interior to the putative trench on an area of higher elevation. The flexural parameter is defined as (e.g., Turcotte and Schubert, 2002)

$$\alpha_c = \left(\frac{4D}{\Delta\rho g} \right)^{1/4}, \quad (5.2)$$

where $\Delta\rho = 3000 \text{ kg m}^{-3}$ is the density contrast between material at the upper and lower boundaries of the plate (atmosphere and asthenosphere, respectively) and $g = 8.87 \text{ m s}^{-2}$ is gravitational acceleration. The flexural rigidity is written in terms of other rheological parameters as (e.g., Turcotte and Schubert, 2002)

$$D = \frac{E h_c^3}{12(1 - \nu^2)}, \quad (5.3)$$

where $E = 65 \text{ GPa}$ is Young's modulus, $\nu = 0.25$ is Poisson's ratio, and h_c is the elastic thickness of the lithosphere estimated from the Cartesian model (Johnson and Sandwell, 1994). Combining and rearranging these two equations,

$$h_c = \left[\frac{3}{E} (\Delta\rho g \alpha_c^4) (1 - \nu^2) \right]^{1/3}. \quad (5.4)$$

Estimated values of h_c are relatively insensitive to uncertainties in $\Delta\rho$ and E because these terms are raised to the one-third versus four-thirds power of α_c in this equation. The curvature of the topographic profile is also described analytically as

$$\kappa(x) = \frac{2}{\alpha_c^2} \exp\left(-\frac{x}{\alpha_c}\right) \left[c_1 \sin\left(\frac{x}{\alpha_c}\right) - c_2 \cos\left(\frac{x}{\alpha_c}\right) \right], \quad (5.5)$$

where positive curvature is concave downwards. The maximum curvature κ_1 is typically $\sim 20\text{--}50\%$ larger than and found interior to κ_0 , the value at the first zero-crossing. Curvature is only strongly negative close to the bottom of the trench, and vanishes to zero as distance increases past the forebulge.

Tectonic stress associated with plate curvature may produce faults. Within the elastic plate, the stress profile is defined as (e.g., Turcotte and Schubert, 2002)

$$\Delta\sigma_e(x, z) = -\frac{E(z - h_c/2)\kappa(x)}{1 - \nu^2}, \quad (5.6)$$

where z is depth increasing from $z = 0$ m at the upper boundary. Compressive and tensional stresses are thus negative and positive, respectively. According to the Anderson theory of faulting, the brittle lithospheric strength is (e.g., Turcotte and Schubert, 2002)

$$\Delta\sigma_c(z) = \frac{\pm 2f_s(\rho g z - P_w)}{(1 + f_s^2)^{1/2} \mp f_s}, \quad (5.7)$$

where $\rho = 2900 \text{ kg m}^{-3}$ is the lithospheric density. Here the upper and lower signs correspond to thrust and normal faults, respectively, in compression and tension. For Venus, we assume that water pore pressure $P_w = 0$ Pa. The coefficient of static friction $f_s \approx 0.85$ for stress ≤ 200 MPa and possible rock types, essentially independent of slip rate and temperature (Byerlee, 1978; Mueller and Phillips, 1995). Plugging in nominal values for all parameters, $\Delta\sigma_c(z) = 202 \text{ MPa } (z/10 \text{ km})$ defines the portion of a yield strength envelope associated with brittle failure in our model of lithospheric flexure.

At the position of the first zero-crossing x_f , we calculate an effective depth of faulting z_f based on the critical condition $\Delta\sigma_e(x_f, z_f) \geq \Delta\sigma_c(z_f)$. Since tensional strength vanishes at the surface, faults should extend from approximately z_f continuously to the upper boundary. Extensional faults with widths ≥ 1 km are identifiable in SAR imagery as a dark band adjacent to a bright band that is further from the source of illumination, but smaller faults are difficult to classify. Bottoms of plates are in compression, but ductile flow rather than brittle failure begins where elastic stress crosses the yield strength envelope (e.g., McNutt, 1984). Regional stresses or flexural processes not captured in our models with principal stresses that exceed $\Delta\sigma_e$ may lead to other types of faults (thrust or strike-slip) on the surface.

Finally, we can write the magnitudes of the applied load and bending moment using the other terms in Eq. 5.1 as, respectively, (e.g., Turcotte and Schubert, 2002)

$$V_0 = \frac{2D}{\alpha_c^3}(c_1 + c_2) \quad (5.8)$$

and

$$M_0 = -\frac{2D}{\alpha_c^2}(c_2). \quad (5.9)$$

Here we assume that c_1 and c_2 are completely independent, although their best-fit values for a given profile are certainly correlated. To model a line load (i.e., with infinitesimal width along track) on a continuous rather than broken plate, we would mandate $c_1 = c_2$. Setting $c_2 = 0$ instead is appropriate for a load applied to the end of a broken plate without any bending moment.

This Cartesian model thus has five best-fit parameters: α_c , c_1 , c_2 , s_r , and w_0 . In practice, c_1 and c_2 also capture any deviation between the estimated value of x_0 and the actual position of the load. This means the above equations do not necessarily return perfectly accurate values of V_0 and M_0 . However, adding an additional fitting parameter to compensate for this discrepancy would introduce large correlated errors that would harm the precision of estimates for α_c and other parameters. In addition, coroneae are quasi-circular objects so assuming a Cartesian geometry is not necessarily appropriate. Because the radius of curvature is only a few times larger than the derived flexural parameter for a typical corona, using this Cartesian model may result in incorrectly estimating some parameters by tens of percents (Johnson and Sandwell, 1994).

Axisymmetric geometry

Our second model is applicable to a disk load on a continuous, elastic plate that is symmetric around an axis perpendicular to the disk and passing through its center. For a disk of radius R with an applied force per unit area of P_0 , the resulting topography has an analytical solution that is conditionally defined as (e.g., Wolf, 1984)

$$w(r) = \begin{cases} -\frac{P_0}{\Delta\rho g} \left(\frac{R}{\alpha_a}\right) \left[\ker' \left(\frac{R}{\alpha_a}\right) \text{ber} \left(\frac{r}{\alpha_a}\right) - \text{kei}' \left(\frac{R}{\alpha_a}\right) \text{bei} \left(\frac{r}{\alpha_a}\right) + \frac{\alpha_a}{R} \right] + s_r r + w_0 \\ -\frac{P_0}{\Delta\rho g} \left(\frac{R}{\alpha_a}\right) \left[\text{ber}' \left(\frac{R}{\alpha_a}\right) \ker \left(\frac{r}{\alpha_a}\right) - \text{bei}' \left(\frac{R}{\alpha_a}\right) \text{kei} \left(\frac{r}{\alpha_a}\right) \right] + s_r r + w_0 \end{cases}, \quad (5.10)$$

where the top and bottom equations are valid for $r < R$ and $r \geq R$, respectively. The ber, bei, ker, and kei are Kelvin functions with apostrophes indicating first derivatives. The regional slope s_r and vertical offset w_0 are the same as in the Cartesian model. Here we assume that radial distance from the center of the load $r = d - x_0 + \Delta x$. If we assume that the minimum elevation in the topographic profile x_0 corresponds to the edge of the disk, then the horizontal offset $\Delta x \approx R$, where R approximately equals the radius of the corona. Values of $\Delta x > R$ indicate

positive distance between a disk and the beginning of a profile, whereas $\Delta x < R$ would imply that the profile partially extends under the load.

Accordingly, this model also has five best-fit parameters: α_a , $P_0/(\Delta\rho g)$, Δx , s_r , and w_0 . Varying R simultaneously with Δx would introduce degeneracies and harm the fits for other parameters. We calculate h_a , the elastic thickness estimated from the axisymmetric model, using Eq. 5.4 and replacing α_c with $2^{1/2}\alpha_a$. Johnson and Sandwell (1994) also considered models of axisymmetric ring and Cartesian bar loads (i.e., with non-negligible widths along track). But those models are essentially equivalent to those for axisymmetric disk and Cartesian line loads, respectively, since the widths of their loads are several times less than typical flexural parameters. In addition, Johnson and Sandwell (1994) found that best-fit estimates of α_c and $2^{1/2}\alpha_a$ should differ by $\leq 10\%$ for coronae with R equal to ~ 0.5 – 10 times the real flexural parameter, although errors in derived values of the load magnitude and actual position are more severe (~ 20 – 50%).

Fitting procedure and sensitivity tests

We determine the best-fit parameters for both flexure models with the Levenberg-Marquardt algorithm (e.g., Markwardt, 2009). This non-linear, least-squares fitting technique also returns an estimate of the covariance matrix, which we convert into the standard error of each parameter. First, we individually fit models to every profile. In order to quantify the impact of topographic noise on the best-fit parameters, we repeat the axisymmetric fits for some profiles after adding Brownian noise, equivalent to fractional Brownian motion with a Hurst index of 0.5. To test the sensitivity of α_a to R , we also repeat some fits with R changed by $\sim 50\%$. Finally, we attempt a “unified fit” by simultaneously fitting axisymmetric models to every topographic profile extracted from a given corona. In this case, we derive only one value of α_a and $P_0/(\Delta\rho g)$ for a corona, but Δx , s_r , and w_0 are still fit separately for each profile to account for their different orientations and starting positions. The number of best-fit parameters in a unified fit is thus equal to $2 + 3n$, where n is the number of topographic profiles. Using the best-fit value of α_a , we then calculate the unified elastic thickness, H_a , and its standard error.

Derived quantities

A real, mechanical plate is necessarily thicker than indicated by purely elastic models to accommodate brittle failure at the top and ductile deformation at the

bottom. Conversion between h_a and h_m , the mechanical thickness, is obtained from linear interpolation of Fig. 4 in Solomon and Head (1990) given a yield strength envelope and an estimate of plate curvature. We assume that ductile deformation begins when yield strength drops below $\sim 50\text{--}100$ MPa, which corresponds to the 1013 K isotherm for a strain rate of 10^{-16} s $^{-1}$ in a flow law appropriate to dry olivine (McNutt, 1984; Solomon and Head, 1990). We also use κ_0 , the curvature calculated from Eq. 5.5 at the first zero-crossing along the Cartesian model, which closely overlaps with the axisymmetric model. We numerically differentiate a spline of degree five—the minimum needed to neatly follow the curve—formulated with best-fit values of α_a and $P_0/(\Delta\rho g)$ to calculate κ_0 and thus H_m , the mechanical thickness associated with the unified fit. Because models with various geometries produce nearly identical fits to the data, any error associated with diverse methods of estimating κ_0 are quite small. Instead using κ_1 , the maximum curvature along the profile, would likewise yield a $<5\text{--}10\%$ increase in mechanical thickness (Mueller and Phillips, 1995).

The average surface temperature of Venus is ~ 740 K. A linear approximation of the lithospheric temperature gradient is thus $dT/dz = 273$ K/ h_m . Likewise, the heat flow out of the surface is $F_S = k(dT/dz)$, where $k \approx 4$ W m $^{-1}$ K $^{-1}$ is thermal conductivity and the sign conventions ensure positive values (e.g., Turcotte and Schubert, 2002). A mechanical thickness of $h_m \approx 27.3$ km, for example, corresponds to a thermal gradient of $dT/dz \approx 10$ K km $^{-1}$ and a heat flow of $F_S \approx 40$ mW m $^{-2}$. Thermal evolution models featuring continuous evolution of Venus in the stagnant-lid regime predict roughly this heat flow as a planet-wide average (e.g., O’Rourke and Korenaga, 2015). Numerical simulations with periodic global overturns obtain wildly different behavior in the past, but again surface heat flows $\sim 40\text{--}60$ mW m $^{-2}$ at present (e.g., Armann and Tackley, 2012). More sophisticated simulations with a coupled atmosphere-interior model also produce an episodic lid regime for the past ~ 2 Gyr with surface heat flow ≤ 40 mW m $^{-2}$ today, but spiking to ~ 60 mW m $^{-2}$ occasionally over the age of the surface (Gillmann and Tackley, 2014). On Earth, the global heat flow is 86 ± 6 mW m $^{-1}$ on average now, roughly twice the values predicted for Venus (Jaupart et al., 2007).

5.4 Results

Representative coronae

Figure 5.2 shows SAR images of four Type 1 coronae that illustrate examples of our analysis in general. They were selected based on having complete stereo coverage,

Name	#	h_a (km)	\pm (km)	h_c (km)	h_m (km)	$2^{1/2}\alpha_a$ (km)	$10^8\kappa_0$ (m ⁻¹)	dT/dz (K km ⁻¹)
Aramaiti	1	17.8	1.3	17.1	20.4	47.1	11	13
	2	25.9	1.2	22.8	34.3	62.4	24	8
	3	12.9	0.9	12.5	15.0	36.9	17	18
	4	3.2	0.1	7.3	4.2	13.1	34	65
Verdandi	1	2.6	0.1	4.3	4.4	11.2	148	62
	2	2.2	0.1	3.9	3.8	10.0	145	72
	3	8.3	0.9	7.2	11.8	26.5	53	23
Nishtigri	1	2.8	0.3	3.3	4.2	11.6	73	65
	2	3.1	0.6	3.5	4.6	12.6	65	59
	3	21.2	1.3	18.8	28.4	53.7	34	10
	4	15.1	1.7	14.2	19.8	41.6	31	14
	5	18.0	2.0	16.7	24.5	47.5	26	11
	6	24.1	1.9	21.9	35.6	59.1	39	8
	7	2.6	0.1	3.7	4.4	11.2	121	62
Ved-Ava	1	7.3	0.5	10.2	7.9	24.0	6	35
	2	5.8	0.5	9.4	6.5	20.3	11	42
	3	4.4	0.2	7.4	5.0	16.4	13	55
	4	3.5	0.2	6.0	4.2	14.0	19	65
	5	5.8	0.2	8.1	7.1	20.3	26	38
	6	7.6	0.4	10.8	9.0	24.8	20	30

Table 5.1: Best-fit parameters from Cartesian and axisymmetric flexure models, along with derived mechanical thicknesses and thermal gradients, for every topographic profile obtained from the four example coronae.

multiple topographic profiles, and representative morphologies. Interpreting their elastic parameters in particular is also somewhat complicated, as discussed below. Between three to seven profiles—drawn and sequentially labeled on each image—were extracted from each corona with visually distinct spacing on the displayed scale from every sector with possible flexural signatures. Myriad volcanic and tectonic features are identifiable beneath the overlying layer of stereo topography, which is mostly transparent. Three Type 2 coronae with flexural signatures are described in the following section, but feature only partial stereo coverage and two analyzed profiles apiece. Figure 5.3 contains the elevation extracted from each profile below best-fit Cartesian, axisymmetric, and unified models found with our least-squares algorithm. Qualitatively, the plotted fits overlap and seem to provide equivalent matches to topographic profiles. Although they are built on divergent assumptions about geometries of the plate and load, available data do not discriminate between them absent any significantly different goodness-of-fit to any profile.

Table 5.1 lists some parameters from these best-fit flexural models alongside derived quantities like mechanical thickness and approximate temperature gradients. The formal errors (“1- σ ”) quoted here for h_a are relatively small (<5–10%), but the best-fit values are correlated with other parameters. Correlation coefficients between α_a

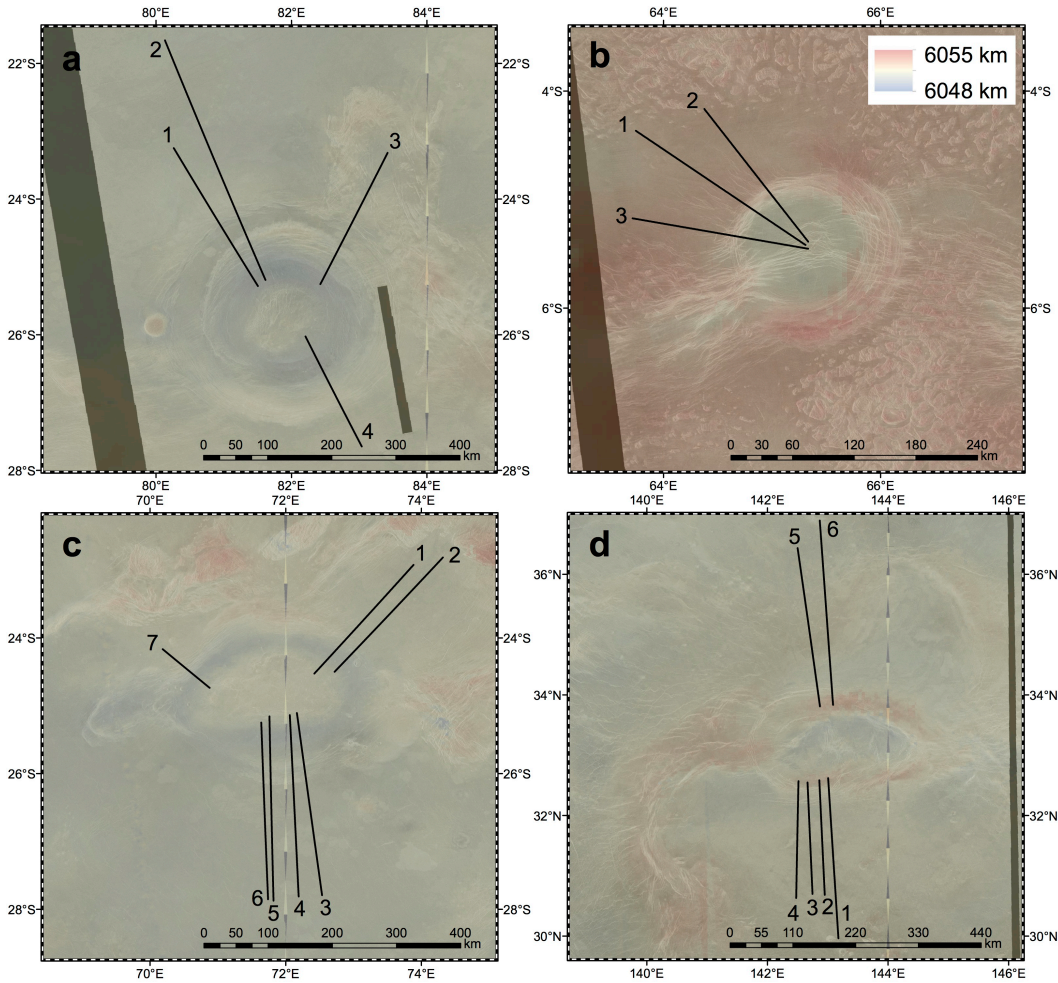


Figure 5.2: Representative images of coronae with topographic profiles containing signatures of lithospheric flexure. The transparent layer in color represents elevation (expressed as distance from the center of Venus, with the mean planetary radius at 6052 km), whereas the underlying greyscale layer is SAR imagery from Cycle 1. The official names of these coronae are (a) Aramaiti, (b) Verdandi, (c) Nishtigri, and (d) Ved-Ava.

and, for instance, Δx and $P_0/(\Delta\rho g)$ are usually $>0.8-0.9$. They may drop to ~ 0.2 for some profiles, but always remain positive since thicker lithosphere requires a higher load placed slightly further away to produce an observed amount of flexure. The terms s_r and w_0 nearly always have coefficients near -0.95 , indicating a strong negative correlation as expected. Non-zero correlations between these two terms and the others simply means that longer profiles usually yield better estimates of flexural parameters through tighter constraints on the regional elevation and slope, assuming that nearby volcanic or tectonic features do not confound the model.

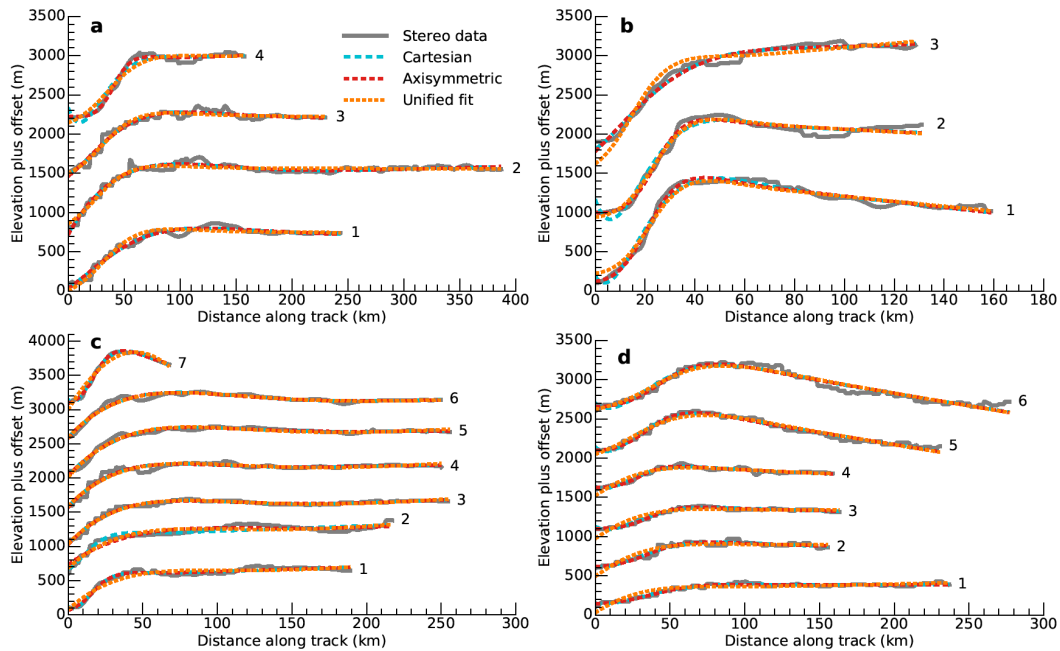


Figure 5.3: Topographic profiles numbered as in Fig. 5.2 (grey, solid lines) and best-fit models of lithospheric flexure (dashed lines) with Cartesian (blue), axisymmetric (red), and unified axisymmetric (orange) geometry. Horizontal axes are distance along the profile from the minimum elevation, omitting portions of each profile covering elevated terrain interior to the minimum elevation. Vertical axes are elevation plus a constant offset for visualization.

Aramaiti has a diameter of ~ 350 km and is located near a faint fracture belt. It is nearly circular, featuring a complete rim with an interior plateau. Topography is rough to the east, but relatively smooth in other directions. Various volcanic features are visible, including a pancake dome to the west and numerous small cones on the interior, rim, and exterior. Each profile yields an estimate for elastic thickness with a formal error < 2 km. Estimates of the flexural parameters from the Cartesian and axisymmetric models—expected to deviate by $\sim 10\%$ (Johnson and Sandwell, 1994)—are consistent within this margin for three out of four profiles. However, the differences between values derived for each profile are much larger than these individual uncertainties. They are probably not normally distributed since their mean ($\bar{h}_a = 15$ km) is less than two times the associated standard deviation (~ 8 km) away from negative values, which are physically impossible. In any case, the range of $h_a \sim 3\text{--}26$ km corresponds to mechanical thicknesses from $\sim 4\text{--}34$ km and surface heat flows from $\sim 30\text{--}260$ mW m $^{-2}$.

Neither SAR images nor inspection of Fig. 5.3 provides evidence to prefer the results

from any profile(s) in particular. External topography and volcanism is arguably most likely to confound profile 3, but the associated estimate of elastic thickness is intermediate overall. This possibly indicates that plate thickness near this corona has dramatic spatial variability. The best-fit value from the unified model, $H_a = 8.2 \pm 0.3$ km, is slightly smaller than \bar{h}_a and associated with less loading force, e.g., $P_0/(\Delta\rho g) \approx 814$ m versus $\sim 1000\text{--}6200$ m for profiles 1–3. So, the formal errors perhaps underestimate the individual uncertainties—the unified model may provide a more accurate plate thickness that is valid around the entire corona.

We performed further analyses of the stereo data extracted from Aramaiti to quantify other sources of uncertainty. First, we repeatedly re-derive h_a for each profile after adding fifty different Brownian noise vectors with a maximum variance of ± 300 m. For profiles 1 through 4, respectively, we find $h_a = 17.9 \pm 1.3$ km, 25.9 ± 1.3 km, 13.1 ± 1.0 km, and 3.2 ± 0.1 km. As expected, the mean values of h_a are nearly equal to the estimates extracted from stereo data without additional, synthetic noise. The distribution of h_a from the noisy profiles is also comparable to the formal errors associated with the original profile. Doubling the maximum variance of the Brownian noise increases the related uncertainties by $\sim 25\text{--}100\%$. Next, we tested various values of R without any artificial noise. We find only a minor effect—best-fit values of h_a change by < 1 km for $R = 100\text{--}250$ km. Therefore, our results are insensitive to any errors in the measurement of coronae radii.

Verdandi is a smaller coronae with a diameter of ~ 180 km located on Manatum Tessera. A circular, complete rim surrounds an inner rise, as with Aramaiti. No pancake domes or large constructs are visible here, but small cones are prevalent as usual. We identified signatures of lithospheric flexure along three profiles radiating from the center of Verdandi to the northwest. We obtained closely clustered estimates for the elastic thickness, associated with mechanical thicknesses < 12 km that are below the mean estimate for Aramaiti. The best-fit value from the unified model, $H_a = 2.9$ km, is consistent within ± 1 km with the averaged value, $\bar{h}_a = 4.4$ km, from each profile. Thin lithosphere implies a high thermal gradient, mostly > 60 K km $^{-1}$ with $F_S > 200$ mW m $^{-2}$. In this case, the load terms are clustered in the range $P_0/(\Delta\rho g) \approx 1200\text{--}1700$ m. Relatively high loads on thin plates also produce comparatively high curvatures, with $\kappa_0 > 1.4$ μm^{-1} for profiles 1 and 2 compared to typical values < 1 μm^{-1} at all coronae. All calculations here assume basaltic properties as is conventional for the volcanic plains, but granitic composition for the tessera has been proposed based on some geomorphic similarities to Earth's continents

(e.g., Treiman, 2007). Decreasing E by $\sim 20\%$ in accordance, for example, would correspond to a $\sim 6\%$ increase in elastic thickness. Accommodating the $\sim 10\%$ decrease in density would require a proportionally thicker brittle layer atop the mechanical plate (e.g., Turcotte and Schubert, 2002). However, the ductile layer would not expand if the rheology of the uppermost mantle still sets the lower plate boundary.

Nishtigri is more elongated than the other example coronae, with a maximum diameter of ~ 376 km. Once again, the interior is elevated with respect to the surrounding terrain and includes both small cones and larger volcanic constructs. Johnson and Sandwell (1994) identified possible flexural signatures to the south in Magellan GTDR altimetry. In their analysis, axisymmetric models indicated $h_a \approx 11\text{--}22$ km in this location, which corresponds well to our analysis with stereo topography. For example, a unified fit using only the southern profiles (3–6) returns $H_a = 19.4 \pm 0.9$ km and $P_0/(\Delta\rho g) = 4914 \pm 526$ m. Topographic noise previously precluded identification of any flexure to the north. Using stereo topography, we extracted three profiles that indicate systematically thinner lithosphere. Profile 7 was constrained by the nearby fracture belt. We include this short segment in our analysis because the derived flexural parameters are consistent with those obtained from the longer profiles 1 and 2. The unified model returns a qualitatively similar agreement to all profiles with $H_a = 26.6 \pm 0.7$ km, matching results from some southern profiles within uncertainties. However, the obvious asymmetries in the SAR imagery makes significant spatial variability seem quite plausible.

Ved-Ava is another elongated corona that has a diameter of ~ 200 km. Concentric fractures cover the entire elevated rim. The interior is lower than the surrounding terrain, which also includes a nearby fracture belt and numerous small cones. Axisymmetric models fit to six profiles return estimates for lithospheric thickness that appear to cluster around $\bar{h}_a = 5.7$ km, possibly in a normal distribution with $\sigma \sim 1.5$ km. Additionally, there is a clear spatial pattern where elastic thickness decreases monotonically from east to west, estimated from profiles on either the north or south sides. Random error could produce this by chance with probability $\sim 1\%$ (six values in sequence) or $\sim 10\%$ (groups of two and four values, both in sequence). Alternatively, Ved-Ava may demonstrate—like Nishtigri but unlike Aramaiti—a spread in elastic parameters revealing real spatial variability in lithospheric structure and/or deformation. Estimated thermal gradients likely vary from ~ 65 K km $^{-1}$ in the east to only $\sim 30\text{--}35$ K km $^{-1}$ in the west. Our unified model produces an estimate of H_a

= 10.7 ± 0.3 km, higher than any of the individual fits, associated with an average load term increased by ~ 500 m.

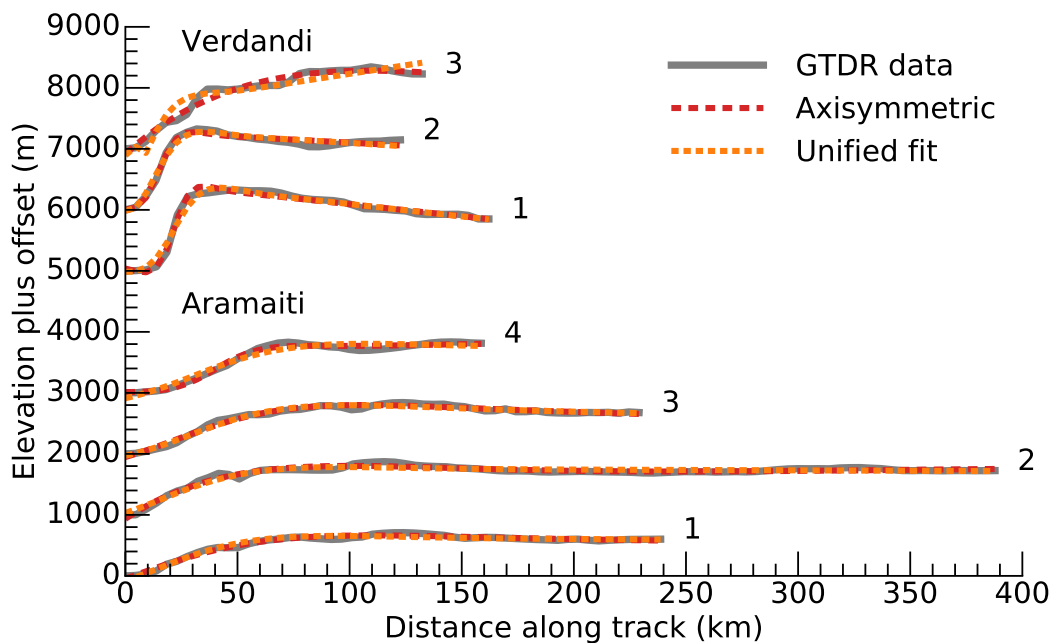


Figure 5.4: Topographic profiles from the original Magellan altimetry data (grey, solid lines) and best-fit models of lithospheric flexure (dashed lines) with axisymmetric (red) and unified (orange) geometry for Verdandi (top) and Aramaiti (bottom). Distance is plotted from the point of minimum elevation, with the interior, elevated portions of each profile removed. Elevation is displayed with arbitrary vertical offsets for visualization.

Figure 5.4 helps show the improvements enabled by high-resolution, stereo topography compared to the original Magellan altimetry. We plot the GTDR elevation for each of the profiles shown in Fig. 5.3 from Verdandi and Aramaiti coronae. Then, we attempt to fit axisymmetric and unified models using our usual least-squares algorithm. For Verdandi, best-fit values of $h_a = 1.2 \pm 0.1$ km, 1.4 ± 0.2 km, and 51.6 ± 167.6 km for profiles 1, 2, and 3, respectively. We also found $H_a = 2.2 \pm 0.3$ km. Although the unified fit is roughly consistent with the results from stereo topography, the obviously ridiculous fit for profile 3 would cast doubt on this result absent conformation from high-resolution data. For Aramaiti, the best-fit results in order from profile 1 are $h_a = 18.0 \pm 3.4$ km, 28.2 ± 3.6 km, 14.8 ± 2.1 km, and 4.0 ± 0.6 km. The unified fit yields $H_a = 11.6 \pm 1.1$ km. Within their uncertainties, these estimates are consistent with results from stereo topography, but the formal errors are several times larger. In general, GTDR data may accurately constrain the elevation of the interior relative to the surrounding terrain for coronae with relatively

shallow and wide trenches. However, stereo topography is critical to measuring the depth of most trenches and, for all small coronae, the plate curvature and thus estimates of mechanical thickness and heat flow.

Population statistics

Occurrence rates of flexural signatures

Using stereo topography, we identified signatures of lithospheric flexure around 18 coronae in addition to the four discussed in the previous section. Assuming the data resolution is sufficient to conclude that a non-detection actually means that flexure is absent, the overall occurrence rate is $\sim 22\%$. Bayesian statistics allow us to determine whether variations in occurrence rates from different subsets of the coronae population are significant, assuming also that our study area is an unbiased sample of the entire population. With a uniform prior, the posterior probability for F —the fraction of coronae with flexure—is derived from the binomial distribution as $\mathcal{P}(F|M, N) \propto F^M(1 - F)^{N-M}$, where N is the total number of coronae and M counts those observed with flexure (Sivia, 1996). The expected value for F is simply $\bar{F} = M/N$ and an estimate of the standard deviation is $\sigma_F = \sqrt{\bar{F}(1 - \bar{F})/N}$. If \bar{F} is very close to either 0 or 1, however, then $\mathcal{P}(F|M, N)$ is asymmetric and σ_F may not represent the usual confidence interval. This formulation is equivalent to determining the fairness of a coin with the presence or absence of flexure representing heads or tails (Sivia, 1996).

We now consider how the prevalence of flexure changes as a function of type, geologic setting, and topographic class. Table 5.2 lists the number of coronae in each category with and without flexural signatures. For Type 1 and 2 coronae, $\bar{F} \approx 0.253$ and 0.125 and $\sigma_F \approx 0.050$ and 0.068 , respectively. Flexure is therefore more often present at Type 1 than Type 2 coronae at the $\sim 2\text{-}\sigma$ confidence level. We could increase this conclusion to $>4\text{-}\sigma$ significance if we observed the same \bar{F} for each type in the $N > 500$ total population. Occurrence rates are higher for coronae near fracture belts than on the plains ($\bar{F} = 0.270$ vs. 0.182), but only with $\sim 1\text{-}\sigma$ significance regardless of whether the fb and fbf categories are compared independently or together. Half of coronae on tessera in our sample have flexural signatures, but $\sigma_F = 0.354$ is too large to determine statistical significance because $N = 2$. None of the coronae on topographic rises exhibit flexure possibly because formation processes unique to this environment do not produce flexural signatures, nearby volcanic or tectonic processes inevitably confound our analysis, or these

Label	Definition	<i>N</i>	<i>M</i>
Coronae type			
Type 1	$\geq 180^\circ$ fracture annulus	75	19
Type 2	$< 180^\circ$ fracture annulus	24	3
Geologic setting			
p	Plains	22	4
fb	Fracture belt	47	12
fbf	Fracture belt (faint)	16	5
t	Tesserae	2	1
r	Topographic rise	12	0
Topographic class			
1	Dome only	1	0
2	Plateau only	6	2
3a	Rim with interior high	17	3
3b	Rim with interior dome	4	2
4	Rim with depression	28	6
5	Outer rise, trough, rim, inner high	11	3
6	Outer rise, trough, rim, inner low	7	4
7	Rim only	18	1
8	Depression only	6	1
9	No topographic signature	1	0

Table 5.2: List of abbreviations that describe coronae type, geologic setting, and topographic class alongside *N*, the number of each category in our study area, and *M*, the number observed with signatures of lithospheric flexure.

areas have a higher heat flow and lack a brittle layer. The average radius and standard deviation for coronae with flexure are $\sim 143 \pm 83$ km, compared to $\sim 123 \pm 59$ km for all coronae without flexure in our study area.

No topographic classes have different occurrence rates at the $>3\text{-}\sigma$ significance level. In particular, the occurrence rates in classes 3a, 4, 5, and 8 are all equivalent within $\sim 1\text{-}\sigma$. The largest disparity is the $\sim 2.75\text{-}\sigma$ decrease in occurrence rates from topographic class 6 to 7, which is expected given the abundance of Type 2 coronae in each class. That is, over half of all Type 2 coronae are in class 7, compared to only $\sim 8\%$ of Type 1 coronae. Type 1 coronae of class 6 are rare ($< 5\%$ planet-wide), but identically zero Type 2 coronae have been placed in this category (Stofan, Smrekar, Tapper, et al., 2001). The difference between classes 6 and both 3a and 8 are also above $2\text{-}\sigma$. However, the significance level drops below $2\text{-}\sigma$ if classes 3a, 3b, 4, and 7 (i.e., with rims and either flat, elevated, or depressed interiors) are compared in combination with classes 5 and 6 (i.e., with outer rises and troughs). No coronae in the topographic classes 1 or 9 has a flexural signature, because the existence of any topographic low associated with a flexural load would mandate another classification. Since there is only one corona from these two categories in our study area, however, their 0% occurrence rates are technically not statistically significant.

Name	R (km)	Sett.	Topo.	n	\bar{h}_a (km)	H_a (km)	\pm (km)	$P_0/(\rho_m g)$ (m)	H_m (km)	F_s (mW m ⁻²)
Indrani	120	p	5	6	5.2	5.2	0.1	886	6.3	175
Verdandi	90	t	3a	3	4.4	2.9	0.1	1258	4.4	247
Habonde	70	fbf	4	3	1.9	1.7	0.1	884	2.8	384
Aramaiti	175	fbf	3b	4	15	8.2	0.3	814	9.2	119
Nishtigri	188	fbf	3b	7	12.4	26.6	0.7	10868	33.6	33
Ohogetsu	93	fbf	4	2	4.3	4.2	0.5	625	5	217
Tai Shan	88	fb	5	2	14.1	13.9	1.7	6315	17.8	61
Maya	113	fbf	3a	2	19.2	12	1.6	7628	17.4	63
Gefjun	150	fb	8	5	8.6	5.4	0.2	759	6.4	172
Abundia	125	p	4	1	4.2	4.2	0.5	406	4.8	227
Ved-Ava	100	fb	4	6	5.7	10.7	0.3	883	11.4	96
Colijnsplaat	175	fb	5	3	8	6.7	0.3	1611	8.3	131
Ceres	338	fb	6	3	9.8	24.1	1.6	5600	28.6	38
Hepat	75	fb	2	6	23.9	38.9	0.3	71511	49	22
Atahensik	405	fb	6	6	19	13.6	0.3	2327	15.7	70
Changko	100	fb	6	4	7.3	2.8	0.1	328	3.3	326
Fatua	200	p	6	6	3.7	4.7	0.2	498	5.4	201
Branwen	160	fb	3a	6	8.8	11.4	0.8	4410	15.1	72
Type 1	55	fb	4	6	8.3	15.9	1.8	1439	16.8	65
Type 2	141	p	7	2	11.3	10.3	0.9	1033	11.2	97
Type 2	105	fb	2	2	14.7	8.3	0.5	2000	10	109
Type 2	73	fb	4	2	6.5	8	0.7	205	8.7	126

Table 5.3: Properties of every coronae with identified signatures of lithospheric flexure, including classification of their geological setting and topography alongside best-fit parameters and derived quantities like mechanical thickness and surface heat flow from the unified model.

Variability of elastic properties

Table 5.3 lists the properties of all coronae with flexural signatures, including the elastic thickness and load term from the unified fit and the average value, \bar{h}_a , derived from n axisymmetric models. We also indicate the geologic setting (Stofan, Smrekar, Tapper, et al., 2001) and the topographic class (Smrekar and Stofan, 1997) of each coronae with and without flexure using abbreviations defined in Table 5.2. Coronae like Maya, Gefjun, Hepat, and Changko resemble Aramaiti with disparate estimates for h_a that do not match a normal distribution. Apart from Nishtigri and Ved-Ava, no obvious spatial pattern to the flexural parameters was identified at these coronae. Other coronae have tightly clustered flexural parameters like Verdandi. Volcanic features observed in or around each corona, including those without flexural signatures, are also noted. Small cones are present at virtually all (>95%) coronae. Volcanic channels and lava flows are also common with occurrence rates around ~41%, whereas pancake domes and larger volcanic domes are only found at 9% and 18% of coronae, respectively.

Johnson and Sandwell (1994) estimated the elastic thickness associated with some smaller coronae despite the impossibility of fitting their topographic profiles to

along-track GTDR data. Instead, they approximated the distance between the minimum elevation in the trench and the maximum height of the outer rise, which is equal to $\pi\alpha_c$ in the Cartesian geometry. Their rough values for elastic thickness were 4.2–7.3 km and 4.9–9.9 km for six and three profiles for Indrani and Fatua coronae, respectively. Our parameters derived from stereo topography are remarkably consistent with these earlier estimates, especially considering the difficulty of identifying the forebulge peak in GTDR data. Besides Nishtigri, discussed above, no other coronae in our study area had previously reported signatures of flexure.

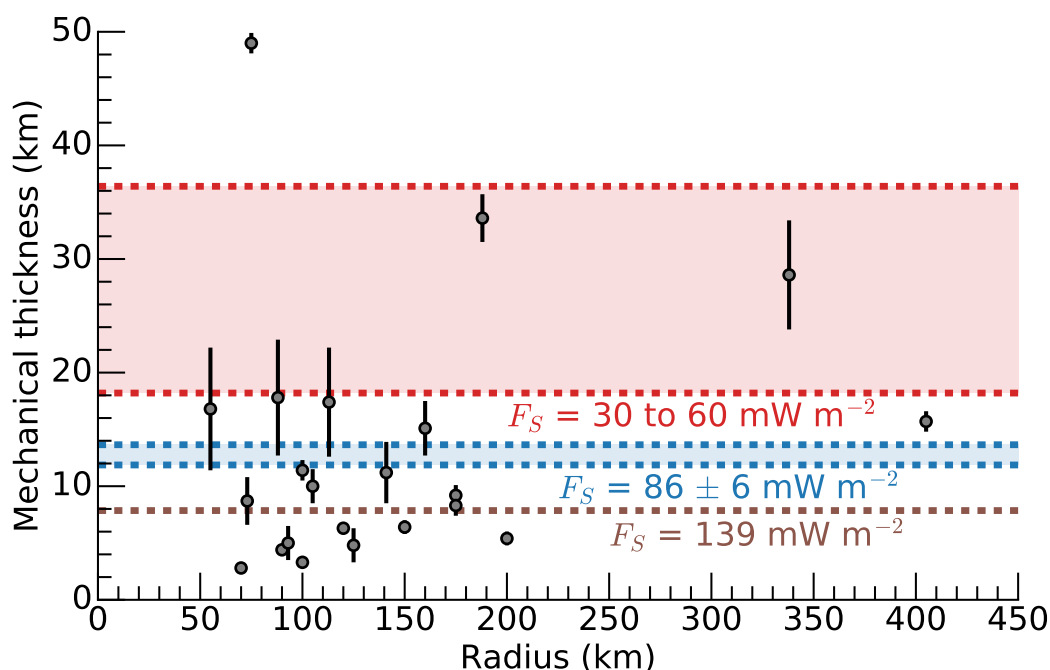


Figure 5.5: Mechanical thicknesses from the unified fit (grey dots), which are inversely proportional to surface heat flows, with formal errors multiplied by three for visualization (black bars). Shaded regions with dashed borders show the ranges associated with surface heat flows expected from models for Venus (red, top) and measured for Earth (blue, below) along with a brown, dashed line illustrating the average surface heat flow estimated from coronae in our study area.

Table 5.3 also includes the mechanical thicknesses and surface heat flows derived from the unified fit. They are plotted in Figure 5.5 with shaded regions of different colors indicating the range expected for Venus (~ 30 to 60 mW m^{-2}) and measured for Earth (e.g., Jaupart et al., 2007; Gillmann and Tackley, 2014; O’Rourke and Korenaga, 2015). Note that $F_S \propto H_m^{-1}$ instead of a linear relationship. The average and median values of surface heat flow are 138 and 114 mW m^{-2} , respectively, indicating bias towards lower values with a long tail of extremely high values rather

than normal distribution. Once again, we observe no correlation with radius. The lowest and highest heat flows are both found at coronae with radii $\sim 70\text{--}75$ km. Only eight coronae ($\sim 36\%$) are associated with Earth-like values or below. Assuming that derived heat flows are approximately valid for a circular radius equal to $3R$ around each corona, their total contribution is ~ 1.7 TW in our study area. Extrapolated to the entirety of Venus, coronae are thus associated with ~ 8.5 TW in total—more than a third of the estimated global budget—despite an effective area covering only $\sim 4\%$ of the surface. This crude calculation assumes that present-day elastic thicknesses represent steady-state heat flow near coronae. However, transient heating events in the past could have reduced their apparent elastic thickness, leading us to estimate low mechanical thicknesses today. Thermal gradients and heat flows were also derived from each individual profile. These exhibit a wider range ($\sim 17\text{--}470$ mW m^{-2}) as expected, but almost identical average and median of ~ 147 mW m^{-2} and ~ 113 mW m^{-2} , respectively.

Beyond occurrence rates, we can examine whether flexural parameters vary systematically between population subgroups. Figure 5.6 plots the estimates for elastic thickness from the unified fit listed in Table 5.3 against radius, geologic setting, and topography class. In general, average elastic thicknesses plus or minus one standard deviation are in the range $\sim 0\text{--}40$ km. Most coronae in our study area have radii between ~ 50 and 200 km. No trends are observed within this size range. Only two coronae with radii >300 km exhibit flexure, and their elastic thicknesses are not obviously distinct from those measured at small coronae. Their best-fit values are both >10 km, but we cannot conclude based on this small sample that large coronae typically host high elastic thicknesses. Likewise, elastic thicknesses of coronae in different geologic settings are apparently comparable. Verdandi is the only coronae with flexure on a tessera. Its \bar{h}_a and H_a are lower than average, but additional observations would be required to demonstrate that tessera preferentially yield low elastic thicknesses. Finally, we failed to identify any specific pattern in the elastic thicknesses of coronae in different topography classes, although the single-digit numbers of examples in each category hinders quantitative analysis.

Virtually every profile crosses concentric faults, which are located on and/or interior to the topographic rise interpreted as a flexural forebulge. Even profiles from the three Type 2 coronae were extracted from the limited region with concentric fractures. Profiles 4, 5, and 6 from Indrani are the only potential exceptions without visible faulting. Inspection of the SAR imagery, however, reveals a dark patch where

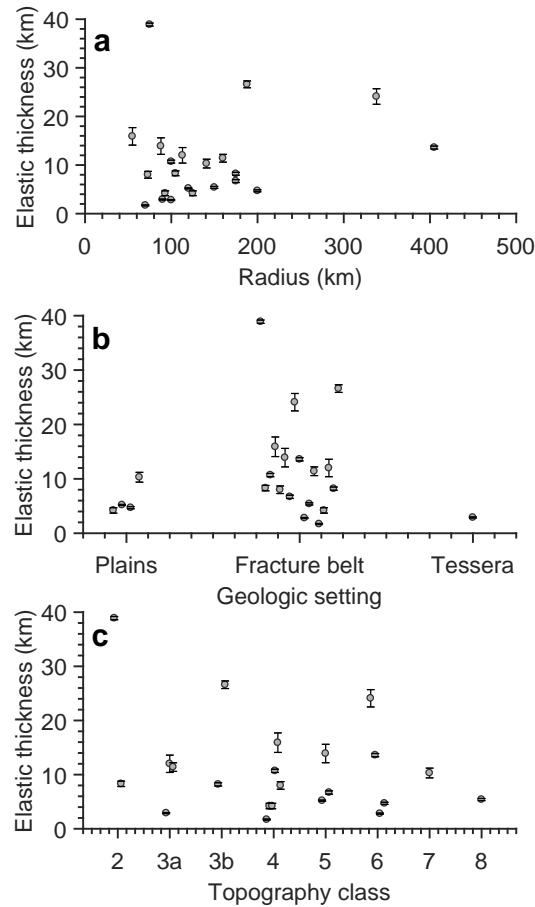


Figure 5.6: Derived values and uncertainties for elastic thickness from the unified fit of each coronae with flexural signatures, ordered by coronae diameter (a), geologic setting (b), and topographic class (c). Small horizontal offsets are inserted within each group in (b) and (c) solely for visualization.

we would expect fracturing, possibly evidencing recent volcanism that has locally buried any tectonic features. A unified fit using those profiles alone suggests $H_a = 6.4 \pm 0.2$ km, larger than the value derived from all profiles. But their effective depths of faulting are also larger, suggesting an increased propensity to host fractures. That is, $z_f = 1.7\text{--}4.0$ km at the first zero-crossing compared to $\sim 0.9\text{--}1.1$ km for profiles 1, 2, and 3 that are observed to intersect concentric fractures as usual. We also calculated values of z_f derived from the best-fit Cartesian models for every profile. They vary from $\sim 0.5\text{--}10.9$ km ($\Delta\sigma_c \sim 10\text{--}220$ MPa) around an average of ~ 3.0 km ($\Delta\sigma_c \sim 61$ MPa).

Elastic models predict that tensional stresses should produce widespread normal faulting near where concentric faults are actually observed. This ubiquity suggests

that elastic bending actually produces these flexural signatures, since viscous deformation may not produce widespread fracturing. Viscous deformation may occur, for instance, at regions of Type 2 coronae lacking both fractures and topography amenable to elastic models. However, the limited resolution of the SAR imagery does not permit definitive characterization of all faults in general, and regional stresses or other processes that occur during coronae formation could form thrust or strike-slip faults. For instance, over half of the coronae with flexure, like Aramaiti, were also observed to host radial fracturing at least on small scales that partially overlaps with concentric fractures. Radial dike swarms could lower elastic thicknesses by heating and thus weakening the lithosphere at coronae like Verdandi and Fatua, but radial fracturing is also seen at coronae with $H_a > 20$ km like Ceres and Hepat.

5.5 Discussion

Roughly one third of the coronae with flexural signatures in our study area have extremely low (≤ 5 km) elastic thickness. Likewise, previous gravity studies identified many coronae where the data are consistent with similar values or even zero elastic thickness (e.g., Smrekar, Comstock, et al., 2003; Hoogenboom, Smrekar, et al., 2004; Hoogenboom, Houseman, and Martin, 2005). These results challenge our assumptions about how Venus operates.

Implications of low elastic thickness

The simplest interpretation of our analysis is that the lithosphere is thinner and the heat flow higher than expected, at least locally near these coronae if not globally on average. Interpreting the spatial distribution of impact craters, several authors proposed that Venus suffered an episode of catastrophic resurfacing accompanied by sharply increased heat flow (e.g., Schaber et al., 1992; Strom et al., 1994). Catastrophic resurfacing is usually dated to ~ 750 Myr ago, implying that Venus is currently in a quiescent period with low heat flow (e.g., McKinnon et al., 1997). A new proposal that near-Earth objects created the exposed craters, however, implies an average surface age as low as ~ 150 Myr (Bottke et al., 2016). So, catastrophic resurfacing could have occurred recently and produced elevated heat flow at present. On the other hand, catastrophic resurfacing is a non-unique interpretation of the cratering record (e.g., Phillips, Raubertas, et al., 1992; Bjornes et al., 2012) and geologic mapping (e.g., Guest and Stofan, 1999). The average surface age—at least of the uppermost few hundred meters—is still quite young if the radar-dark floors

of most (~80%) extant craters are evidence of post-impact volcanic modification (e.g. Wichman, 1999; Herrick and Rumpf, 2011; O'Rourke, Wolf, et al., 2014). Stagnant-lid convection is thus also compatible with recent magmatism that produces localized regions of high heat flow (e.g., O'Rourke and Korenaga, 2015), possibly alongside increasing temperature in the mantle that would elevate heat flow on average (Smrekar and Sotin, 2012). In general, a plume origin for coronae may predict more local heating than models featuring downwelling instabilities alone (e.g., Smrekar and Stofan, 1997).

Dry diabase rheology implies that the mechanical thickness of the lithosphere is only fractionally greater than its elastic thickness. But certain complications could reconcile moderate thermal gradients with thin elastic lithosphere. Anhydrous conditions in the crust and lithosphere are often presumed because of the high surface temperatures and lack of oceans (e.g., Kaula, 1995; Mackwell et al., 1998). However, planetary building blocks like carbonaceous chondrites and other meteorites have water contents >1% by weight. Solidification of a magma ocean immediately after accretion likely produces an early water ocean, but the interior can retain significant amounts of volatiles as well (e.g., Elkins-Tanton, 2011). Subsequent volcanic processing is unlikely to completely dry out the interior, especially given the incomplete degassing of the presumed inventory of radiogenic argon-40 (O'Rourke and Korenaga, 2015). Increased thickness is required to accommodate a certain amount of flexure if the plate is wet instead of dry (e.g, Mueller and Phillips, 1995) or possibly granitic rather than basaltic at tessera (e.g., Treiman, 2007). In this case, thin elastic lithosphere could actually correspond to mechanical thicknesses and heat flows that match global averages predicted by most models of thermal evolution.

Alternatives to low elastic thickness

Flexure could arise from deformation of a thick viscous lithosphere, rather than a thin elastic plate in which large fiber stresses are statically maintained. In this case, systematic variations in elastic thickness at coronae like Nishtigri and Ved-Ava may actually indicate different strain-rates operating on lithosphere with uniform thickness (>100 km). Additional observational constraints are required to apply viscous models to Venus, however, since lithospheric thickness is degenerate with strain rate (e.g., Johnson and Sandwell, 1994). In other words, many different elastic and viscous models representing a wide range of plate thicknesses would likely provide similar goodness-of-fit to stereo topography. Random differences between adjacent profiles, however, are probably still attributable to confounding

topography or localized volcanism.

Viscous deformation requires dynamic processes to produce and sustain flexural signatures. Additionally, the dimensionless Deborah number $De = \tau_m/\tau_d$ —the Maxwell relaxation time divided by the time scale of deformation—should not exceed unity (e.g., Fourel et al., 2014). If $\eta \sim 10^{23}$ – 10^{25} Pa s is lithospheric viscosity, then $\tau_m = \eta/E \sim 0.05$ – 5 Myr. We can estimate an upper limit for τ_d , which must not exceed the characteristic decay time required to yield the observed occurrence rate of flexural signatures (Johnson and Sandwell, 1994). We also assume that the production rate of coronae is roughly steady. Then, $F = 0.22$ suggests that $\tau_d \leq 33$ or 165 Myr for mean surface ages of ~ 150 or 750 Myr, respectively. Near this upper limit, $De \ll 1$ and viscous deformation indeed dominates. But elastic behavior is perhaps most important if coronae are younger on average than most surface features, meaning that their formation time is actually much shorter than the timescale for viscous relaxation.

High lithospheric thicknesses at coronae are also possible if flexural signatures actually result from other processes. For example, gravitational relaxation of surface topography produced during the late stages of coronae formation has been proposed to produce signatures resembling flexure (e.g., Stofan, Bindschadler, et al., 1991; Janes et al., 1992). Time scales for crustal flow exceed the average surface age if dry diabase rheology is appropriate (Mackwell et al., 1998), but may be $< 10^5$ yr if the lithosphere is wet (Smrekar and Solomon, 1992). Likewise, topographic signatures may simply reflect variations in crustal thickness after complete isostatic (Airy) compensation (e.g., Smrekar and Stofan, 2003). Improved gravity field measurements would allow us to discriminate between these hypotheses.

5.6 Conclusions

Possible signatures of lithospheric flexure have been identified at 22 out of 99 coronae in the study area where stereo topography is available. Cartesian and axisymmetric models of the bending of a thin, elastic plate provide good fits to these topographic profiles, yielding estimates of elastic thicknesses at these coronae ranging from ~ 1.5 – 37 km. Mechanical thicknesses and thermal gradients associated with values at the uppermost end of this range are comparable to those predicted by thermal evolution models that lack a recent (< 500 Myr ago) episode of catastrophic resurfacing. However, median values imply that surface heat flows—possibly associated with plumes—are locally as much as twice above Earth’s global average,

indicating that coronae are perhaps responsible for a large portion of the total heat budget. Alternatively, our assumptions of dry, diabase rheology and purely elastic behavior may require modification. Predicted tensional stresses should create normal faults that resemble the concentric fractures observed intersecting nearly all analyzed profiles. We find significant variability in the elastic thicknesses derived from different profiles at individual coronae, both with and without obvious spatial patterns. Type 2 coronae are relatively less likely to host flexural signatures than those of Type 1. Coronae with flexure have radii ~ 20 km greater on average than those without, although the distribution of elastic thicknesses versus coronae diameters shows no clear trend. Given the limited numbers in each subgroup, we also failed to identify correlations between elastic thickness and geologic setting or topography class. High-resolution topography for the entire planet would presumably permit flexural modeling for five times as many coronae, leading to robust statistical inferences.

*Chapter 6***THERMAL EVOLUTION OF VENUS WITH ARGON
DEGASSING****6.1 Abstract**

Decades-old measurements of atmospheric and elemental surface composition constrain the history of Venus. In this study, we search for a model featuring continuous evolution in the stagnant-lid regime that predicts the present-day atmospheric mass of radiogenic argon and satisfies the other available constraints. For comparison, we also consider the end-member scenario of a single catastrophic resurfacing event. Thermal evolution simulations are performed that track the mass transport of argon and potassium and include a simple model of upwelling mantle plumes. Sensitivity analyses and linear regression are used to quantify the range of initial conditions that will produce desired values for key model output parameters. Decompression melting of passively upwelling mantle causes considerable mantle processing and crustal growth during the early evolution of Venus. Mantle plumes have negligible effects on recent crustal production, but may be important to local surface features. For a wide range of initial conditions, continuous evolution in the stagnant-lid regime predicts the correct amount of argon degassing, along with the absence of a global magnetic field, crustal and lithosphere thicknesses matching modern estimates, and volcanism consistent with the cratering record. Argon degassing does not uniquely constrain mantle dynamics, but the success of simple stagnant-lid models diminishes the need to invoke dramatic changes like catastrophic resurfacing.

6.2 Introduction

Venus, like Earth, is an engine that converts heat into interesting phenomena. Given their comparable orbital parameters, masses, and radii, Venus likely also differentiated into a silicate mantle and an iron-rich core, although its moment of inertia is not actually known (Bills et al., 1987). Dichotomous surface conditions are the most obvious proof that the evolution of Venus and Earth sharply diverged at some point. Earth is habitable and even clement, but greenhouse gases have raised surface temperatures on Venus to roughly 740 K (e.g., Bullock and Grinspoon, 2001). Whereas mantle dynamics cause frequent surface recycling on Earth through plate tectonics, mantle convection on Venus currently occurs below a rigid lithosphere

that encompasses the entire planet (e.g., Kaula and Phillips, 1981; Solomatov and Moresi, 1996). In fact, all terrestrial planets in our Solar System besides Earth presently operate in this stagnant-lid regime of mantle convection (e.g., Schubert et al., 2001), which is perhaps natural because the viscosity of materials comprising terrestrial planets is strongly temperature-dependent (Solomatov, 1995). No consensus exists, however, as to whether Venus exhibited dramatically different internal dynamics in the past, complicating the interpretation of surface geology.

Some models attempt to couple the evolution of both the interior and atmosphere of Venus (e.g., Phillips, Bullock, et al., 2001; Noack et al., 2012; Driscoll and Bercovici, 2013; Gillmann and Tackley, 2014). Greenhouse warming of the atmosphere may cause periodic increases in surface temperature to ~ 1000 K, possibly sufficient to cause episodic transitions from the stagnant- to mobile-lid regimes by reducing the viscosity contrast across the lithosphere (Noack et al., 2012). High surface temperatures are also suggested to favor an episodic or stagnant-lid regime over plate tectonics for three reasons. First, a hot surface may eventually result in increasing mantle temperatures, causing convective stress to drop below the lithosphere yield stress on a ~ 1 Gyr timescale (Lenardic et al., 2008). Second, a non-Newtonian rheology based on damage theory predicts that high temperatures strengthen the lithosphere through a higher healing rate within ~ 100 Myr (Landuyt and Bercovici, 2009). Finally, high surface temperatures preclude the presence of surface water, which may be important to the generation of plate tectonics through lowering the brittle strength of lithosphere (e.g., Moresi and Solomatov, 1998; Korenaga, 2007).

Impact craters revealed by synthetic aperture radar images collected during NASA's Magellan mission provide major constraints on the evolution of Venus. The spatial coordinates of the ~ 1000 craters are indistinguishable from a random distribution. Only a few ($<10\%$) craters are obviously embayed by lava flows that breach their rims and cover their ejecta blankets. These two facts motivated the catastrophic resurfacing hypothesis, in which an episode of extreme volcanism lasting ~ 100 Myr covered the vast majority of the surface in km-thick flows (e.g., Schaber et al., 1992; Strom et al., 1994). According to studies of the likely impactor population and atmospheric screening, catastrophic resurfacing would have occurred between ~ 300 Ma and 1 Ga (e.g., McKinnon et al., 1997). Catastrophic resurfacing is also compatible with the so-called directional stratigraphy that categorizes morphologically similar terrains as globally synchronous units (e.g., Ivanov and Head, 2013). Theorists have invoked many mechanisms to explain catastrophic resurfacing, ranging from

episodic subduction caused by lithosphere thickening above a warming mantle (Turcotte, 1993; Fowler and O'Brien, 1996) to brittle mobilization of the lithosphere (Moresi and Solomatov, 1998) to lid overturn caused by low yield stress (Armann and Tackley, 2012; Gillmann and Tackley, 2014). Transitions from the thick- to thin-lid branches of stagnant-lid convection (Reese, Solomatov, and Moresi, 1999) or a cessation of plate tectonics (e.g., Phillips, 1998) have also been proposed. In any model, some recent volcanism is also required to explain the existence of young lava flows identified as high emissivity anomalies in Venus Express data (Smrekar, Stofan, et al., 2010) and sulfuric acid/water clouds, which would not persist without volcanic replenishment of SO₂ that is otherwise removed from the atmosphere within ~50 Myr (Fegley and Prinn, 1989; Bullock and Grinspoon, 2001).

Other evidence casts doubt on the idea of catastrophic resurfacing. Alternative stratigraphic studies suggest that local processes operating gradually throughout geologic time produced the surface features on Venus (Guest and Stofan, 1999). New mapping, for example, reveals that ribbon tesserae terrain records a geologic history that predates the formation of many other features attributed to catastrophic resurfacing (Hansen and Lopez, 2010). Non-catastrophic processes can also explain every characteristic of the cratering record. Localized resurfacing events can produce a random-looking distribution of craters and a low number of obviously embayed craters (Phillips, Raubertas, et al., 1992; Bjonnes et al., 2012; O'Rourke, Wolf, et al., 2014). New studies argue that post-impact lava flows have partially filled the craters with radar-dark floors, which comprise ~80% of the total population (Wichman, 1999; Herrick and Sharpton, 2000; Herrick and Rumpf, 2011). Statistical modeling demonstrates that localized resurfacing events consisting of thin, morphologically indistinguishable flows can explain the number and spatial distribution of these dark-floored craters (O'Rourke, Wolf, et al., 2014). A minor amount of regionally concentrated volcanism can explain the relatively few, clustered craters that are obviously embayed in Magellan imagery.

Besides impact craters, the thicknesses of the crust and lithosphere of Venus provide important constraints on models of its history. Using gravity and topography data to construct a map of crustal thicknesses, however, requires an estimate of the mean crustal thickness, which is subject to large uncertainty. James et al. (2013) calculated the mean thickness of the crust as ~8 to 25 km, with an upper limit of ~45 km, using a two-layered crustal thickness inversion. Previous estimates of the present-day crustal thickness range from ~20 to 60 km (e.g., Smrekar, 1994; Simons et al.,

1997; Nimmo and McKenzie, 1998). The observed topography may provide coarse upper bounds for crustal thickness because it would significantly relax if the crust were thick enough to cause lateral flow (Nimmo and Stevenson, 2001) or to undergo the phase transition from (metamorphosed) basalt to eclogite (e.g., Namiki and Solomon, 1993). Constraints on the thickness of the mantle lithosphere of Venus are likewise loose. Some authors favor a relatively thick lithosphere, usually ~200 to 400 km (e.g., Turcotte, 1993; Solomatov and Moresi, 1996), but data permit values as high as ~600 km (Orth and Solomatov, 2011). Thinner (~100 km) lithosphere allows a larger magnitude of melt generation to explain recent resurfacing (e.g., Schubert, 1994; Smrekar, 1994; Simons et al., 1997; Nimmo and McKenzie, 1998).

Observations suggest that the core of Venus is likely cooling, but not convecting with sufficient vigor to produce a dynamo. Features in gravity field and topography data that are associated with large volcanic rises, high radar emissivity anomalies, and stratigraphically young flows indicate the presence of several plumes upwelling from the lower mantle (Stofan, Smrekar, Bindschandler, et al., 1995; Smrekar, Stofan, et al., 2010; Smrekar and Sotin, 2012). The existence of plumes might imply, at minimum, a positive heat flux across the core/mantle boundary (e.g., Weizman et al., 2001). However, Venus today has no global magnetic field (Phillips and Russell, 1987). Paleomagnetic evidence indicates that Earth's dynamo, in contrast, has persisted for more than 3.4 Gyr (Tarduno, Cottrell, Watkeys, et al., 2010). Perhaps Venus lacks an inner core and thus compositional convection or, less likely, the core is completely frozen solid (Stevenson, 1983; Stevenson, 2003). Stagnant-lid convection is inefficient compared to plate tectonics, so the mantle will tend to insulate the core and limit cooling (e.g., Driscoll and Bercovici, 2014). Recent theoretical and experimental work indicates that the thermal conductivity of iron alloys at core conditions is possibly very high, meaning that driving a dynamo with thermal convection alone is quite difficult (e.g., Pozzo et al., 2012; Gomi et al., 2013). Significant cooling still is required even if conventionally low values for thermal conductivity are actually correct (e.g., Zhang et al., 2015). Another possibility is that the core became compositionally stratified and thus convectively stable during accretion, since more light elements tend to enter core material as pressure/temperature conditions increase (e.g., Rubie, Jacobson, et al., 2015).

Degassing of noble-gas elements has long been incorporated into thermal evolution models for Earth (e.g., Sleep, 1979; Tajika and Matsui, 1993), but few studies have applied the same techniques to Venus. Argon-40, in particular, is produced by the

decay of radioactive ^{40}K in the interior of Venus and released to the atmosphere through volcanism. The present-day atmospheric abundance ^{40}Ar has been measured as 3.3 ± 1.1 ppb relative to the mass of Venus or $1.61 \pm 0.54 \times 10^{16}$ kg (Zahn et al., 1983). This datum has been used to test the plausibility of ad hoc crustal production histories for Venus (Namiki and Solomon, 1998) and to place more general constraints on crustal thickness and the evolution of Venus (Kaula, 1999). A 2D cylindrical model with strongly temperature- and pressure-dependent viscosity confirmed that a substantial fraction of argon could degas even without plate tectonics (Xie and Tackley, 2004). Different modes of mantle convection may cause varying amounts of volcanism and thus degassing (e.g., O'Neill et al., 2014). One experimental study potentially diminishes the utility of ^{40}Ar degassing as a constraint on planetary evolution, however, claiming that argon may be more compatible with basaltic melts than olivine and that argon diffusion takes place very slowly (Watson et al., 2007). But a more recent investigation with a different experimental approach suggests that the results of Watson et al. (2007) may not properly represent bulk crystalline properties, thus supporting the usual assumptions that argon is incompatible and that diffusion can occur quickly at high temperatures (Cassata et al., 2011).

The purpose of this study is to evaluate whether models of the evolution of Venus can predict the present-day atmospheric mass of radiogenic argon while satisfying other available constraints. We use parameterized models of stagnant-lid convection, which have long been applied to the terrestrial planets in our Solar System (e.g., Stevenson, 1983). A scaling law of stagnant-lid convection that takes into account complications from mantle processing and crustal formation, however, was only developed recently (Korenaga, 2009). This formulation has been applied to Mars (Fraeman and Korenaga, 2010) and, with modification, to massive terrestrial planets (O'Rourke and Korenaga, 2012). Our new contribution in this study is the self-consistent incorporation of models for both argon degassing and mantle plumes.

6.3 Quantifying argon degassing

In this section, we discuss the fundamental assumptions underlying models of argon degassing during the thermochemical evolution of Venus. The initial abundances of ^{40}Ar in the atmosphere and interior are usually considered negligible (e.g., Namiki and Solomon, 1998; Kaula, 1999). Thus, radioactive decay of ^{40}K produced all of the ^{40}Ar that is observed today. For a closed system, we can calculate the abundance

of ^{40}Ar as a function of time:

$$[^{40}\text{Ar}(t)] = \frac{\lambda_{Ar}}{\lambda_{tot}} [^{40}\text{K}(0)] (1 - e^{-\lambda_{tot}t}), \quad (6.1)$$

where $\lambda_{tot} = \lambda_{Ar} + \lambda_{Ca}$ is the decay constant for ^{40}K , with $\lambda_{Ar} = 0.0581 \text{ Gyr}^{-1}$ and $\lambda_{Ca} = 0.4962 \text{ Gyr}^{-1}$ (Kaula, 1999). The abundance of ^{40}K obeys:

$$[^{40}\text{K}(t_p)] = [^{40}\text{K}(0)] e^{-\lambda_{tot}t_p}, \quad (6.2)$$

where $t_p = 4.5 \text{ Gyr}$ has elapsed since accretion. We assume $^{40}\text{K}/\text{K} = 1.165 \times 10^{-4}$ (Kaula, 1999).

The present-day abundances of radioactive isotopes on both Venus and Earth are only loosely constrained. Data from four Venera and Vega lander sites on Venus indicate $\text{K}/\text{U} = 7220 \pm 1220$ (Kaula, 1999). Elemental abundances were measured with very poor precision on Venus relative to available data from Earth and Mars. Furthermore, these landers only visited the lowland volcanic plains, which themselves exhibit chemical heterogeneity, leaving many geologic terrains on Venus unexplored (Treiman, 2007). In any case, estimated values of Earth's K/U are much higher, e.g., $\text{K}/\text{U} = 13,800 \pm 1,300$ in Arevalo et al. (2009). We might expect a relatively low K/U for Venus because potassium is volatile and Venus is closer to the Sun than Earth, but simulations of planetary formation and migration suggest that Venus and Earth might have accreted with similar inventories of volatile elements (e.g., Rubie, Jacobson, et al., 2015). So, they may actually have similar K/U . Kaula (1999) assumed that $[\text{U}] = 21 \text{ ppb}$ for Venus, corresponding to the conventional geochemical model of Earth (e.g., McDonough and Sun, 1995). However, even for Earth, this value has nontrivial uncertainty. A plausible lower bound for Earth's mantle is $[\text{U}] = 13 \text{ ppb}$ (Lyubetskaya and Korenaga, 2007a). Kaula (1999) calculated that $24 \pm 10\%$ of the available ^{40}Ar resides in the atmosphere if $\text{K}/\text{U} = 7220$ and $[\text{U}] = 21 \text{ ppb}$. As shown in Figure 6.1, however, Venus may have degassed as much as $\sim 50\%$ if $[\text{U}] = 13 \text{ ppb}$. Alternatively, if $[\text{U}] = 24 \text{ ppb}$ and $\text{K}/\text{U} = 15,200$, which are near the upper limits of plausible values for Earth, then Venus may be only $\sim 10\%$ degassed.

Despite these uncertainties, we can model the effects of crustal production and degassing on the planetary budget of K , ^{40}K , and ^{40}Ar . Argon-40 partitioning is assumed to follow the usual formula for accumulated fractional melting (Shaw, 1970):

$$\frac{[^{40}\text{Ar}]_c}{[^{40}\text{Ar}]_{SM}} = \frac{1}{\phi} \left[1 - (1 - \phi)^{1/D} \right], \quad (6.3)$$

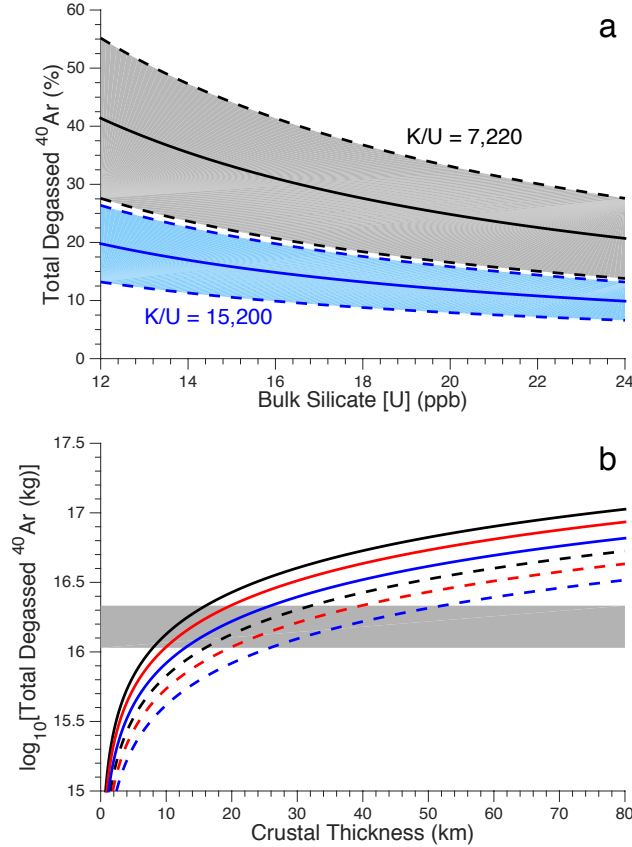


Figure 6.1: (a) Percentage of the total amount of ^{40}Ar that has been degassed from the interior to the atmosphere of Venus as a function of the bulk silicate $[U]$ at present. Black and blue lines represent calculations assuming $K/U = 7,220$ and $15,200$, respectively. Shaded regions are $1-\sigma$ uncertainty envelopes derived from the formal error on the measurement of the present-day amount of atmospheric ^{40}Ar . (b) Predictions of the present-day atmospheric mass of radiogenic ^{40}Ar as a function of crustal thickness produced in a single event with $\phi = 0.025$ and 0.05 (solid and dashed lines, respectively) and $[U(t_p)] = 21, 17,$ and 13 ppb (black, red, and blue lines, respectively). The measured value ($1-\sigma$ range) is shaded in grey (Zahn et al., 1983).

where $[^{40}\text{Ar}]_c$ and $[^{40}\text{Ar}]_{SM}$ are the abundances of ^{40}Ar in the newly generated crust and the source mantle, respectively. The melt fraction is ϕ and the bulk distribution coefficient is D . Because D is very small, we approximate $(1 - \phi)^{1/D} \approx 0$ (e.g., Kaula, 1999). Likewise, we assume $[K]_c/[K]_{SM} \approx [^{40}\text{K}]_c/[^{40}\text{K}]_{SM} \approx 1/\phi$. For a given crustal thickness h_c , the associated crustal volume V_c can be calculated with a geometrical relation (Fraeman and Korenaga, 2010):

$$V_c = \frac{4\pi}{3}[R_p^3 - (R_p - h_c)^3], \quad (6.4)$$

where R_p is the radius of Venus. The volume of mantle processed to make crust is simply $V_{proc} = V_c/\phi$.

Two additional assumptions allow us to calculate the amount of ^{40}Ar degassed as a result of an episode of crustal production. First, if all ^{40}Ar from the processed mantle is degassed, then we can calculate the mass of ^{40}Ar immediately added to the atmosphere:

$$M_i = [^{40}\text{Ar}(t_c)]_{SM} \left(\frac{\rho_m V_c}{\phi} \right), \quad (6.5)$$

where t_c is the time of crustal production and ρ_m is the density of the mantle. Next, we assume that argon diffusion through the crust is effectively instantaneous. This is reasonable because high surface temperatures on Venus should allow argon to escape feldspar and olivine grains within ~ 1 Myr and then travel quickly through grain boundaries to the surface (Namiki and Solomon, 1998; Kaula, 1999). The mass of ^{40}Ar generated by radioactive decay in the crust and then released by diffusion until the present is therefore:

$$M_d = \rho_m V_c [^{40}\text{K}(t_c)]_c \left(\frac{\lambda_{Ar}}{\lambda_{tot}} \right) [1 - e^{-\lambda_{tot}(t_p - t_c)}]. \quad (6.6)$$

The total mass of atmospheric ^{40}Ar expected at present is simply $M_{atm,^{40}\text{Ar}} = M_i + M_d$. Atmospheric escape of argon, unlike radiogenic helium, is assumed to be negligible. As a simple problem, we calculate the unrealistic, end-member example of a single episode of crustal formation from partial melting of the primitive mantle (PM). In this case,

$$M_{atm,^{40}\text{Ar}} = [^{40}\text{K}(0)]_{PM} \left(\frac{\rho_m V_c}{\phi} \right) \left(\frac{\lambda_{Ar}}{\lambda_{tot}} \right) (1 - e^{-\lambda_{tot} t_p}), \quad (6.7)$$

which is independent of t_c . Figure 6.1 illustrates that the production of ~ 10 to 50 km of crust in a single event could explain the observed atmospheric mass of radiogenic argon for plausible values of ϕ and $[U(t_p)]$. However, realistic models must consider how crustal production occurs throughout geologic time.

6.4 Theoretical formulation

The thermal and chemical evolution of Venus may be simulated with a one-dimensional parameterized model using scaling laws built on numerical models (Korenaga, 2009). Assuming that Venus is initially differentiated into the primitive mantle and the core, we use the thermal and chemical structure shown in Fig. 6.2. The stagnant lid is a thermal boundary layer consisting of the mantle lithosphere

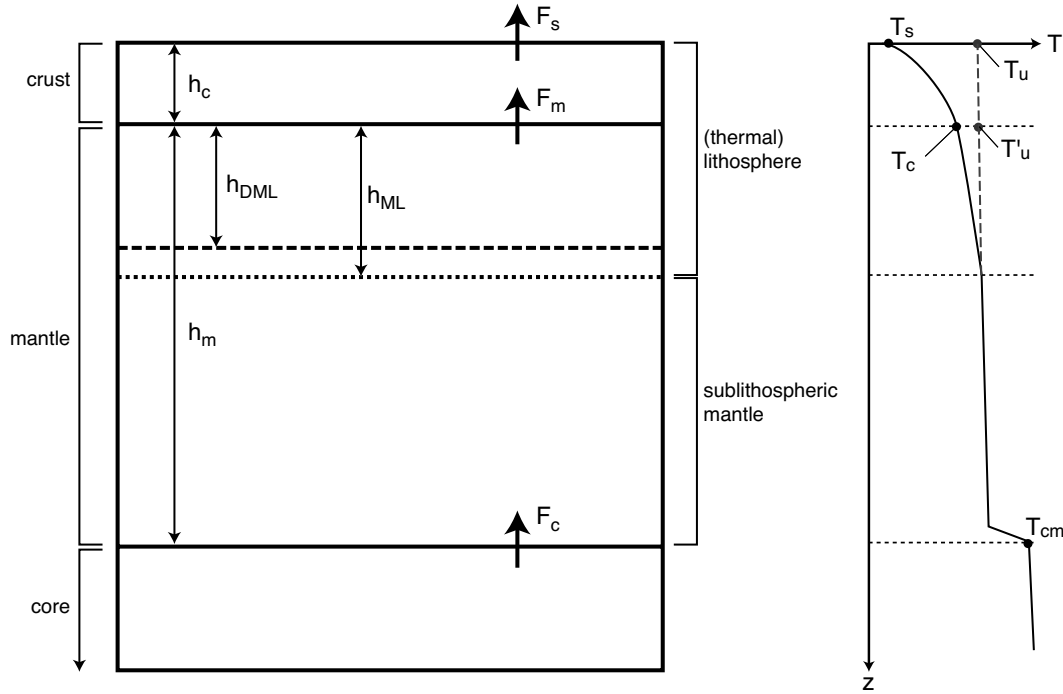


Figure 6.2: Cartoon showing the assumed thermal (right) and chemical (left) structure of Venus, reproduced from Fraeman and Korenaga (2010) and O'Rourke and Korenaga (2012). Key model parameters are illustrated.

(ML) and the chemically distinct crust. The depleted mantle lithosphere (DML) is the upper region of the primitive mantle (PM) that has been processed by partial melting to form crust, which is always thinner than the ML. The convecting mantle that underlies the stagnant lid becomes more depleted than the PM over time, as the DML could delaminate if cooled enough to overcome its chemical buoyancy and become mixed with the convecting mantle. The convecting mantle is thus referred to as the source mantle (SM). The evolution of these layers is simulated using the formulation from O'Rourke and Korenaga (2012) with some modifications to track mantle plumes and mass transport of argon and potassium. To be self-contained, the entire procedure is briefly summarized below.

Model description

The two governing equations are the energy balances for the core and the mantle. For the core:

$$[4\pi R_i^2 \rho_c (L_c + E_g) \frac{dR_i}{dT_{cm}} - \frac{4}{3}\pi R_c^3 \eta_c \rho_c C_c] \frac{dT_{cm}}{dt} = 4\pi R_c^2 F_c, \quad (6.8)$$

where R_i and R_c are the radii of the inner and entire core, respectively; E_g is the gravitational energy liberated per unit mass of the inner core; L_c is the latent heat of solidification associated with the inner core; T_{cm} is the temperature at the core/mantle boundary; η_c is the ratio of T_{cm} , the temperature at the core side of the core/mantle boundary, to the average core temperature; C_c is the specific heat of the core; ρ_c is the density of the core; and F_c is the heat flux out of the core. We use the method of Stevenson (1983) to parametrize core cooling, including the calculation of F_c , which assumes that the liquid outer core is chemically homogenous. We calculate the liquidus with the concentration of light elements in the core fixed to 0.1 by analogy to Earth. However, we use the viscosity given below by Eq. 6.11 to calculate the thickness of the lower boundary layer in the mantle. Stevenson (1983) used a much lower viscosity, which yields a thin boundary layer and a very small (<15 K) core/mantle temperature contrast. For the mantle (Hauck and Phillips, 2002):

$$\frac{4}{3}(R_m^3 - R_c^3) \left(H_m - \eta_m \rho_m C_m \frac{dT_u}{dt} \right) - \rho_m f_m L_m = 4\pi(R_m^2 F_m - R_c^2 F_c), \quad (6.9)$$

where R_m is the radius of the mantle; H_m is the volumetric heat production of the mantle; η_m is the ratio of the average temperature of the mantle to T_u , the potential temperature of the mantle; ρ_m is the density of the mantle; C_m is the specific heat of the mantle; f_m is volumetric melt production (explained below) with associated latent heat release, L_m ; and F_m is the heat flux across the mantle/crust boundary.

We consider heat production from the radioactive decay of ^{40}K , ^{235}U , ^{238}U , and ^{232}Th . Volumetric radiogenic heating may be calculated (Korenaga, 2006):

$$H_m(t) = \rho_m \sum_n c_{n,0} P_n(0) e^{-\lambda_n t}, \quad (6.10)$$

where, for each isotope, $c_{n,0}$ is the initial abundance, $P_n(0)$ is the initial specific heat production, and λ_n is the decay constant. Constants used to calculate radiogenic heat production are taken from Kaula (1999) and Korenaga (2006). Initial isotopic abundances are calculated from the present-day $[\text{U}]_{PM}$ and K/U , assuming that the following ratios are valid at the present for the primitive mantle (Korenaga, 2006): $^{40}\text{K}/\text{K} = 1.165 \times 10^{-4}$, $^{238}\text{U}/\text{U} = 0.9927$, $^{235}\text{U}/\text{U} = 0.0072$, and $^{232}\text{Th}/\text{U} = 4$.

Mantle viscosity is parametrized assuming a Newtonian rheology (Fraeman and Korenaga, 2010):

$$\eta(T_u, C_{SM}^W) = A \exp \left[\frac{E}{RT_u} + (1 - C_{SM}^W) \log \Delta \eta_w \right], \quad (6.11)$$

where R is the universal gas constant, A is a preexponential constant calculated assuming a reference viscosity η_0 at a temperature $T_u^* = 1573$ K, and E is the activation energy. We use values of E appropriate to the rheology of the upper mantle, such as ~ 300 kJ mol $^{-1}$ for dry olivine (Karato and Wu, 1993). Near the core/mantle boundary, E may increase to ~ 520 kJ mol $^{-1}$, but absolute temperature rises as well (Yamazaki and Karato, 2001). Melting may cause dehydration of the mantle over time. We parametrize the resulting increase in viscosity using $\Delta\eta_w$, the viscosity contrast between dry and wet mantle, and C_{SM}^W , the normalized water concentration within the mantle, which has an initial value of one and decreases towards zero (Fraeman and Korenaga, 2010; O'Rourke and Korenaga, 2012).

With the above viscosity formulation, two non-dimensional parameters characterize thermal convection in the stagnant-lid regime (Solomatov, 1995). First, the internal Rayleigh number quantifies potential convective vigor (Fraeman and Korenaga, 2010):

$$Ra_i = \frac{\alpha \rho_m g (T'_u - T_c) h_m^3}{\kappa \eta(T_u, C_{SM}^W)}, \quad (6.12)$$

where α is the coefficient of thermal expansion; T'_u and T_c are the mantle potential temperature defined at the top of the mantle and the temperature at the bottom of the crust (called the ‘‘Moho’’ temperature), respectively; h_m is the thickness of the mantle; and κ is thermal diffusivity. Second, we use the Frank-Kamenetskii parameter (Solomatov, 1995; Fraeman and Korenaga, 2010):

$$\theta = \frac{E(T'_u - T_c)}{RT_u^2}. \quad (6.13)$$

With these two parameters, we calculate the average convective velocity of passive upwellings beneath the stagnant lid (Solomatov and Moresi, 2000):

$$u = 0.38 \frac{\kappa}{h_m} \left(\frac{Ra_i}{\theta} \right)^{1/2}. \quad (6.14)$$

The Nusselt number is a non-dimensional measure of convective heat flux. A simple scaling exists for stagnant-lid convection with purely temperature-dependent viscosity (Solomatov and Moresi, 2000), but including the effects of dehydration stiffening and compositional buoyancy requires the Nusselt number to be calculated with the local stability analysis at each time step, which precludes an analytic expression. The symbolic functionality is (Korenaga, 2009):

$$Nu = f(Ra, E, T_u, T_c, h_{DML}, h_m, \Delta\eta_m, \Delta\rho), \quad (6.15)$$

where h_{DML} is the thickness of the depleted mantle lithosphere and $\Delta\eta_m$ and $\Delta\rho$ respectively represent the viscosity and density contrasts between the depleted mantle and the source mantle. Finally, the thickness of the thermal boundary layer in the mantle, termed the mantle lithosphere, is calculated (Fraeman and Korenaga, 2010):

$$h_{ML} = \frac{h_m}{Nu}. \quad (6.16)$$

During stagnant-lid convection, passively upwelling mantle rock partially melts as its pressure decreases. As in Fraeman and Korenaga (2010) and O'Rourke and Korenaga (2012), we calculate the initial pressure of melting (Korenaga, 2002):

$$P_i = \frac{T_u - 1423}{1.20 \times 10^{-7} - (dT/dP)_S}, \quad (6.17)$$

where $(dT/dP)_S$ is the adiabatic mantle gradient, assuming that the Venusian mantle follows the solidus of dry peridotite. Melting stops at the base of the mantle lithosphere, with the final pressure of melting calculated as:

$$P_f = \rho_m g (h_c + h_{ML}), \quad (6.18)$$

where we assume for simplicity that ρ_m is the density of the lithosphere. As long as $P_i > P_f$, there is a melting zone with thickness d_m and average melt fraction equal to

$$\phi = \frac{P_i - P_f}{2} \left(\frac{d\phi}{dP} \right)_S, \quad (6.19)$$

where $(d\phi/dP)_S$ is the melt productivity by adiabatic decompression. Finally, we calculate the volumetric melt production from pressure release melting (Fraeman and Korenaga, 2010):

$$f_m = \frac{2d_m u \phi}{h_m} 4\pi R_m^2, \quad (6.20)$$

where u is calculated in Eq. 6.14 and the numerical coefficients arise from the assumption that the passively upwelling mantle is cylindrical.

Upwelling mantle plumes

Upwelling plumes from the core/mantle boundary may transport heat to the top of the mantle if there exists a thermal boundary layer at the bottom of the mantle. Smrekar and Sotin (2012) argued that the temperature difference, ΔT_{cm} , must exceed the viscous temperature scale, $\Delta T_\eta = |1/(\partial \ln \eta / \partial T)|$, to produce plumes with realistically large buoyancy fluxes. From Eq. 6.11, $\Delta T_\eta = RT_u^2/E \sim 80$ K for $T_u = 1700$ K and $E = 300$ kJ mol⁻¹. However, we assume that plumes can transport

some heat flux as long as $\Delta T_{cm} > 0$. The maximum volume of material available to form plumes is $V_p = 4\pi R_c^2 \delta_c$, where δ_c is the thickness of the thermal boundary layer on the mantle side of the core/mantle boundary and R_c is the radius of the core. Material in the thermal boundary layer is replenished on time scale $\tau = \delta_c^2/\kappa$, where κ is thermal diffusivity. The maximum volume of plume material that can be delivered to the lithosphere in time Δt is therefore (Weizman et al., 2001):

$$S_{p,max} = \Delta t \left(\frac{V_p}{\tau} \right) = \Delta t \left(\frac{4\pi R_c^2 \kappa}{\delta_c} \right). \quad (6.21)$$

Only a fraction of the boundary layer will actually form plumes. Thus, the rate of heat delivery by plumes may be expressed as (Weizman et al., 2001):

$$F_p = S_p \left(\frac{\rho_m C_m \Delta T_p}{4\pi (R_p - h_c)^2} \right), \quad (6.22)$$

where ΔT_p is the plume temperature anomaly, which we assume is equal to ΔT_{cm} , the total temperature difference across the core/mantle boundary, and R_p is the radius of Venus. Assuming that $R_p \gg h_c$, we may use Eqs. 6.21 and 6.22 to write an equation for the maximum heat flux from mantle plumes:

$$F_{p,max} = \frac{k \Delta T_{cm}}{\delta_c} \left(\frac{R_c}{R_p} \right)^2 = F_c \left(\frac{R_c}{R_p} \right)^2. \quad (6.23)$$

Thus, as expected, the heat flux from mantle plumes does not exceed the heat flux from the core/mantle boundary. We assume that the heat flux from plume upwelling is some fraction of the core heat flux, i.e. $F_p = f(R_c/R_p)^2 F_c$, where $0 \leq f < 1$. Thus, we may calculate:

$$S_p = f F_c \left(\frac{R_c}{R_p} \right)^2 \left[\frac{4\pi (R_p - h_c)^2}{\rho_m C_m \Delta T_p} \right]. \quad (6.24)$$

We suppress plume magmatism for the first 0.5 Gyr of each simulation to avoid unrealistically large values from the ‘‘hot start’’ of the core. Choosing $f \leq 0.5$ compensates for the likely overestimation of ΔT_p in this formulation and the decrease in excess temperature that occurs as plumes rise through the mantle (Leng and Zhong, 2008).

Internal heating and surface cooling drive mantle convection in the absence of mantle plumes. In this case, the mantle heat flux is the heat conducted through the upper thermal boundary layer (Fraeman and Korenaga, 2010):

$$F'_m = k \frac{Nu(T'_u - T_c)}{h_m}. \quad (6.25)$$

Mantle plumes provide an additional heat flux at the base of the upper boundary layer. We assume that plumes do not affect its overall structure since the heat flux from mantle plumes is relatively small. Thus, the total mantle heat flux is calculated as $F_m = F'_m + F_p$ (Weizman et al., 2001).

We assume that the upwelling plume reaches the base of the lithosphere within the time step of duration Δt and undergoes partial melting. The initial pressure of plume melting, $P_{i,p}$, is calculated using Eq. 6.17 with the substitution of $T_{u,p} = T_u + \Delta T_{cm}$, which is the potential temperature of the mantle plumes, i.e., the temperature that they would have if raised from the core/mantle boundary to the surface along an adiabatic temperature gradient. The final pressure of melting and the average melt fraction in the melting region are calculated using Eqs. 6.18 and 6.19. Finally, the total melt productivity of the mantle plumes is simply $f_p = \phi_p S_p$, assuming that the entire plume passes through the region of melting.

Mass transport of argon and potassium

We model argon degassing and the mass transport of potassium using a variation of the method that Fraeman and Korenaga (2010) used to track the dehydration of the mantle. The amount of mantle that has been melted during a time interval Δt is (Fraeman and Korenaga, 2010):

$$\Delta V_{proc} = \Delta t \left(\frac{f_m}{\phi} + S_p \right). \quad (6.26)$$

The associated increase in crustal volume is $\Delta V_c = (f_m + f_p)\Delta t$. By mass balance, ignoring small density differences, the change in the volume of the DML is $\Delta V_{DML} = \Delta V_{proc} - \Delta V_c$. Assuming that $^{40}\text{K}/\text{K}$ is negligibly small, the mass of potassium in the PM is calculated as

$$M_{PM,K} = \rho_m V_{PM} [\text{K}(0)]_{PM}, \quad (6.27)$$

where the volume of the PM, V_{PM} , is constant. The volume of the convecting SM is simply $V_{SM}(t) = V_{PM} - V_{DML}(t) - V_c(t)$. So, the crustal mass of potassium may be tracked as

$$M_{c,K}(t) = M_{c,K}(t - \Delta t) + \rho_m \Delta V_{proc} [\text{K}(t)]_{SM}, \quad (6.28)$$

where the abundance of potassium in the convecting SM, $[\text{K}(t)]_{SM}$, is calculated as

$$[\text{K}(t)]_{SM} = \frac{M_{PM,K} - M_{c,K}(t)}{\rho_m V_{SM}(t)}. \quad (6.29)$$

Finally, the crustal abundances of K and ^{40}K are their crustal masses divided by $\rho_c V_c(t)$, where we assume that $\rho_c \approx \rho_m$ for simplicity.

Tracking the transport of ^{40}K is more complicated because of radioactive decay. The mass in the PM decreases with time as

$$M_{PM,^{40}\text{K}}(t) = \rho_m V_{PM} [^{40}\text{K}(0)]_{PM} e^{-\lambda_{tot} t}. \quad (6.30)$$

The crustal mass of ^{40}K is thus calculated as

$$M_{c,^{40}\text{K}}(t) = M_{c,^{40}\text{K}}(t - \Delta t) e^{-\lambda_{tot} \Delta t} + \rho_m \Delta V_{proc} [^{40}\text{K}(t)]_{SM}, \quad (6.31)$$

where the abundance of ^{40}K in the SM is simply

$$[^{40}\text{K}(t)]_{SM} = \frac{M_{PM,^{40}\text{K}}(t) - M_{c,^{40}\text{K}}(t)}{\rho_m V_{SM}(t)}. \quad (6.32)$$

We assume that all ^{40}Ar partitioned into or generated within the crust is instantaneously released to the atmosphere. Thus, we can track the atmospheric mass of ^{40}Ar

$$\begin{aligned} M_{atm,^{40}\text{Ar}}(t) &= M_{atm,^{40}\text{Ar}}(t - \Delta t) + \rho_m \Delta V_{proc} [^{40}\text{Ar}(t)]_{SM} \\ &\quad + \rho_c V_c(t) [^{40}\text{K}(t)]_c \left(\frac{\lambda_{tot}}{\lambda_{Ar}} \right) (1 - e^{-\lambda_{tot} \Delta t}). \end{aligned} \quad (6.33)$$

The mass of ^{40}Ar in the PM and its abundance in the SM, respectively, are calculated as

$$M_{PM,^{40}\text{Ar}}(t) = M_{PM,^{40}\text{K}} \left(\frac{\lambda_{tot}}{\lambda_{Ar}} \right) (1 - e^{-\lambda_{tot} t}) \quad (6.34)$$

and

$$[^{40}\text{Ar}(t)]_{SM} = \frac{M_{PM,^{40}\text{Ar}}(t) - M_{atm,^{40}\text{Ar}}(t)}{\rho_m V_{SM}(t)}. \quad (6.35)$$

Incorporating incomplete partitioning of argon or slow diffusion would require more complicated equations. Eqs. 6.34 and 6.35 would only give upper and lower limits for $M_{atm,^{40}\text{Ar}}(t)$ and $[^{40}\text{Ar}(t)]_{SM}$, respectively. Additionally, if crustal recycling occurs faster than argon diffusion, then less degassing would be expected for a given amount of mantle processing.

6.5 Numerical models

The parametrized model described above was used to calculate the thermal and chemical evolution of Venus in the stagnant-lid regime. All permutations of the following sets of parameters and initial conditions were used: activation energy, $E =$

Parameter	Definition	Value	Units	Ref.
<i>Constant</i>				
k	Thermal conductivity	4.0	$\text{W m}^{-1} \text{K}^{-1}$	[1]
κ	Thermal diffusivity	10^{-6}	$\text{m}^2 \text{s}^{-1}$	[1]
α	Thermal expansivity	2×10^{-6}	K^{-1}	[1]
g	Gravitational acceleration at surface	8.87	m s^{-2}	[3]
T_s	Surface temperature	730	K	[1]
R_p	Radius of Venus	6050	km	[3]
R_c	Core radius	3110	km	[4]
ρ_m	Mantle density	3551	kg m^{-3}	[1]
ρ_c	Core density	12500	kg m^{-3}	[1]
P_{cm}	Pressure at core/mantle boundary	130	GPa	[1]
P_c	Pressure at the center of Venus	290	GPa	[1]
C_m	Specific heat of the mantle	1200	$\text{J kg}^{-1} \text{K}^{-1}$	[4]
C_c	Specific heat of the core	850	$\text{J kg}^{-1} \text{K}^{-1}$	[3]
η_m	Ratio of average and potential T for the mantle	1.3	-	[1]
η_c	Ratio of average and potential T for the core	1.2	-	[1]
L_m	Latent heat of mantle melting	6.0×10^5	J kg^{-1}	[5]
$(L_c + E_g)$	Heat release from inner core formation	5.0×10^5	J kg^{-1}	[5]
$(d\phi/dP)_S$	Melt productivity from adiabatic decompression	1.20×10^{-8}	Pa^{-1}	[6]
$(dT/dP)_S$	Adiabatic temperature gradient in the mantle	1.54×10^{-8}	K Pa^{-1}	[6]
<i>Variable</i>				
f	Fraction of core heat flux carried by plumes		-	
E	Activation energy		kJ mol^{-1}	
η_0	Reference viscosity		Pa s	
ϕ	Melt fraction		-	
V_{proc}/V_{SM}	Fraction of source mantle processed by melting		-	
$M_{atm,^{40}\text{Ar}}$	Atmospheric mass of radiogenic argon		kg	
$[\text{K}]_c$	Crustal abundance of potassium		w.t. %	
ΔT_{cm}	Temperature contrast across core/mantle boundary		K	
$\Delta h_{c,0.5}$	Crustal production during the last 0.5 Gyr		km	

Table 6.1: List of key model parameters. References: [1] Stevenson (1983), [2] Korenaga (2006), [3] Noack et al. (2012), [4] Spohn (1991), [5] Fraeman and Korenaga (2010), and [6] Korenaga (2002). Variables are chosen or calculated as described in the text.

300, 350, and 400 kJ mol^{-1} ; present-day $\text{K/U} = 7220, 10510, \text{ and } 13800$; present-day uranium abundance, $[\text{U}(t_p)]_{PM} = 13, 15, 17, 19, \text{ and } 21$ ppb; initial mantle potential temperature, $T_u(0) = 1500, 1600, 1700, 1800, \text{ and } 1900$ K; initial core/mantle boundary temperature, $T_{cm}(0) = 4000, 4200, \text{ and } 4400$ K; and reference viscosity, $\log_{10}(\eta_0) = 19, 19.5, 20 \text{ and } 20.5$. The parameter governing how the progressive dehydration of the mantle increases its viscosity is set to $\Delta\eta_w = 100$. We also assumed that compositional buoyancy of the DML, $d\rho/d\phi = 120 \text{ kg m}^{-3}$, which controls $\Delta\rho$ in Eq. 6.15 (Fraeman and Korenaga, 2010; O'Rourke and Korenaga, 2012). Values for fixed constants and definitions of other key parameters are listed in Table 6.1. The simulations were numerically integrated with the Euler method

for 4.5 Gyr with a time step of 1 Myr.

The parameterization of mantle plume upwelling may affect the calculated history of crustal production and argon degassing. We set $f = 0.25$ for most simulations. But we also performed a sensitivity analysis with another 50 simulations to test the importance of the large uncertainty in this parameter. Fixing $E = 300 \text{ kJ mol}^{-1}$, $K/U = 7220$, $[U(t_p)]_{PM} = 17 \text{ ppb}$, $T_u(0) = 1900 \text{ K}$, $T_{cm}(0) = 4200 \text{ K}$, and $\log_{10}(\eta_0) = 20.5$, we varied f within the plausible range of 0.01 to 0.5 in increments of 0.01. For each simulation, we focus on $M_{atm,^{40}\text{Ar}}(t_p)$, $h_c(t_p)$, and $\Delta h_{c,0.5}$, the thickness of crust produced in the last 0.5 Gyr.

Limited constraints were placed on the simulation results. In particular, we only accepted simulations with realistic crustal thicknesses and positive surface heat flux, i.e., $1 \text{ km} \leq h_c(t_p) \leq 75 \text{ km}$ and $F_s(t_p) > 0 \text{ mW m}^{-2}$. Out of 2700 total, 1310 failed these criteria because they featured extremely high or low values of K/U , $[U(t_p)]_{PM}$, $T_u(0)$, and/or $T_{cm}(0)$. With $K/U = 7220$, present-day $[U]_{PM} = 21$ and 13 ppb are equivalent to initially 7.07×10^{-8} and $4.38 \times 10^{-8} \text{ W m}^{-3}$ of volumetric radiogenic heating, respectively. Important model outputs included time series and present-day values for the parameters illustrated in Fig. 6.2, as well as the present-day atmospheric mass of radiogenic argon and the modern crustal abundance of potassium.

6.6 Results

Sample thermal and chemical history

Simulations conform to observational constraints on the evolution of Venus for certain combinations of initial conditions. Figure 6.3 shows the results of one representative example generated using $f = 0.25$, $E = 300 \text{ kJ mol}^{-1}$, $K/U = 7220$, $[U(t_p)]_{PM} = 17 \text{ ppb}$, $T_u(0) = 1900 \text{ K}$, $T_{cm}(0) = 4200 \text{ K}$, and $\log_{10}(\eta_0) = 20.5$. Core cooling is most intense as high temperatures from the “hot start” in the core are lost in the first ~ 1 Gyr. Since the mantle potential temperature actually increases for ~ 1.5 Gyr, core cooling quickly declines until ~ 2.2 Gyr. No inner core growth occurs within 4.5 Gyr, and the modern core only loses heat by conduction. That is, the total heat flux of 2.3 TW out of the core at present is probably insufficient to drive a dynamo by thermal convection alone (e.g., Pozzo et al., 2012; Gomi et al., 2013). This simulation satisfies the most basic criterion for the existence of mantle plumes: $F_{cm}(t_p) > 0 \text{ mW m}^{-2}$ (e.g., Weizman et al., 2001). The temperature contrast across the core/mantle boundary is $\Delta T_{cm}(t_p) \sim 60 \text{ K}$, roughly 40% less than

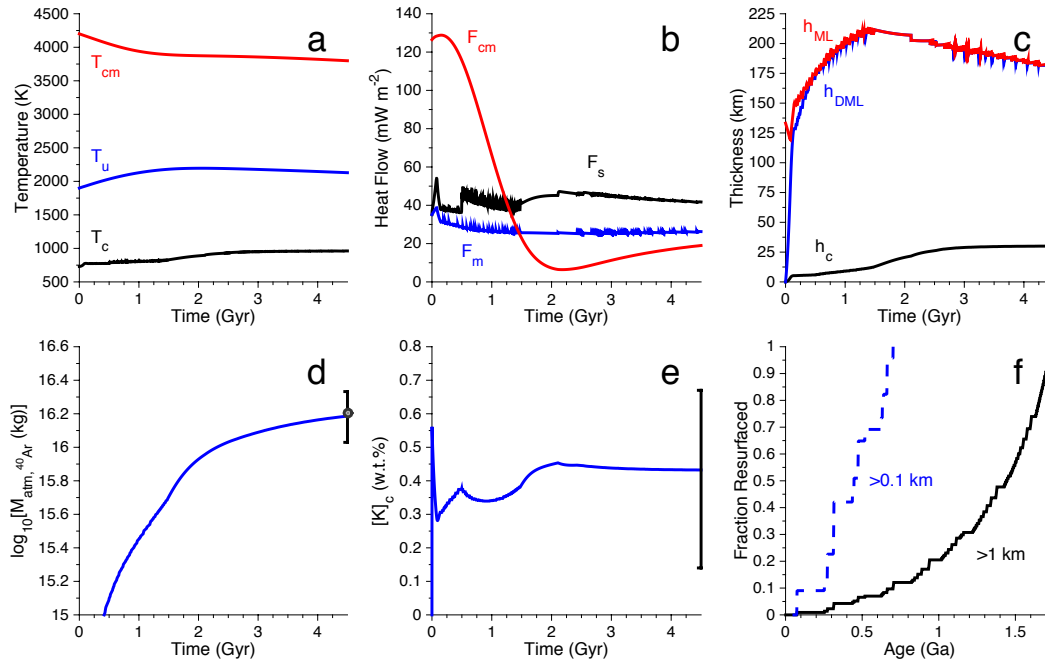


Figure 6.3: Calculated thermal and chemical history for Venus with $f = 0.25$, $E = 300 \text{ kJ mol}^{-1}$, $K/U = 7220$, $[U(t_p)]_{PM} = 17 \text{ ppb}$, $T_u(0) = 1900 \text{ K}$, $T_{cm}(0) = 4200 \text{ K}$, and $\log_{10}(\eta_0) = 20.5$. (a) Core/mantle boundary, mantle potential, and Moho temperatures (red, blue, and black, respectively). (b) Core, mantle, and surface heat fluxes (red, blue, and black). The moving average of the surface heat flux is plotted with a 5 Myr span because basal melting of the crust may cause large discontinuities. (c) Crustal thickness (black), and thicknesses of the depleted mantle lithosphere (blue) and mantle lithosphere (red), which are nearly identical after $\sim 100 \text{ Myr}$. (d) Atmospheric mass of radiogenic argon (blue) and present-day measurement (point with $1\text{-}\sigma$ error bars). (e) Crustal abundance of potassium (blue) and range of plausible values from Venera and Vega landers (black vertical bar). (f) Cumulative fraction of Venus that has been resurfaced, on average, to a depth of at least 0.1 km (blue, dashed) and 1 km (black, solid) as a function of time before present, assuming that the amounts of intrusive and extrusive volcanism are equal.

the viscous temperature scale (Smrekar and Sotin, 2012). Plumes are still plausible in this simulation because our formulation of core heat flux assumes that the lower thermal boundary layer has already been thinned by the ejection of plumes, e.g., to a present-day $\sim 13 \text{ km}$ (Stevenson, 1983). Including radiogenic heating in the core or increasing the viscosity of the lower mantle would both tend to increase the core/mantle temperature contrast.

Crustal and lithosphere thicknesses calculated for the present are both within plausible ranges (e.g., Nimmo and McKenzie, 1998; James et al., 2013). The average

crustal thickness calculated for the present is ~ 30 km. This simulation also predicts an atmospheric mass of radiogenic argon within $0.14\text{-}\sigma$ of the measured, present-day value. The average crustal abundance of potassium is also near the mean value of existing measurements (e.g., Kaula, 1999). The initial spike visible in panel e occurs because ϕ is relatively large during the early epoch of rapid cooling. Mantle melting has cumulatively processed most of the source mantle, i.e., $V_{proc}(t_p) \approx 0.82V_{SM}(t_p)$. Roughly 60% of the total inventory of heat-producing elements is sequestered in the crust at the end of the simulation. So, the volumetric heating of the source mantle at present is only $\sim 40\%$ of what would be produced in the undifferentiated primitive mantle. The normalized water concentration in the mantle is $C_{SM}^W \sim 0.45$ at the end of the simulation, meaning that the dehydration term in Eq. 6.11 is only $\sim 6\%$ of the other term inside the exponential. Thus, Venus can retain a significant portion of its initial interior inventory of volatiles for over 4.5 Gyr.

Rough estimates of the surface age of Venus are shown in panel f of Fig. 6.3. Because the one-dimensional model only returns a global average, we must calculate the time since a certain amount of crustal production occurred to estimate the fraction of the surface of Venus that has been resurfaced. For example, say a global average of 1 km of magmatism is required for complete resurfacing. Then, 50% of the surface would have an age of ≤ 1.5 Ga if 0.5 km of crust were produced from 3 Gyr to the present, assuming that all magmatism is extrusive. To calculate estimated ages in Fig. 6.3, we assume that only 50% of crustal production causes resurfacing because some volcanism is likely intrusive. Thinner volcanic flows could cover a much larger fraction of the surface. In this simulation, an average of ~ 132 m of crust was produced during the last ~ 500 Myr. Surface features like mountains or tall rims of large craters with ages > 1.75 Ga can remain unburied and thus visible in surface imagery. Studies of the cratering record likewise indicate that thin, post-impact flows have partially filled most craters, but much of the surface is possibly ancient nevertheless (e.g., Herrick and Rumpf, 2011; O'Rourke, Wolf, et al., 2014).

Sensitivity analyses

Figure 6.4 shows the output of 1390 simulations of the evolution of Venus. Present-day values of important parameters are plotted against present-day crustal thickness. Because we conducted a grid search of a large parameter space, only 943 and 377 simulations produced the observed amount of radiogenic argon within 2- and $1\text{-}\sigma$, respectively. Of the 377, 233 simulations also predict crustal production during the latest 500 Myr, of which $\sim 94\%$ also have $F_{cm}(t_p) > 0 \text{ mW m}^{-2}$. The median

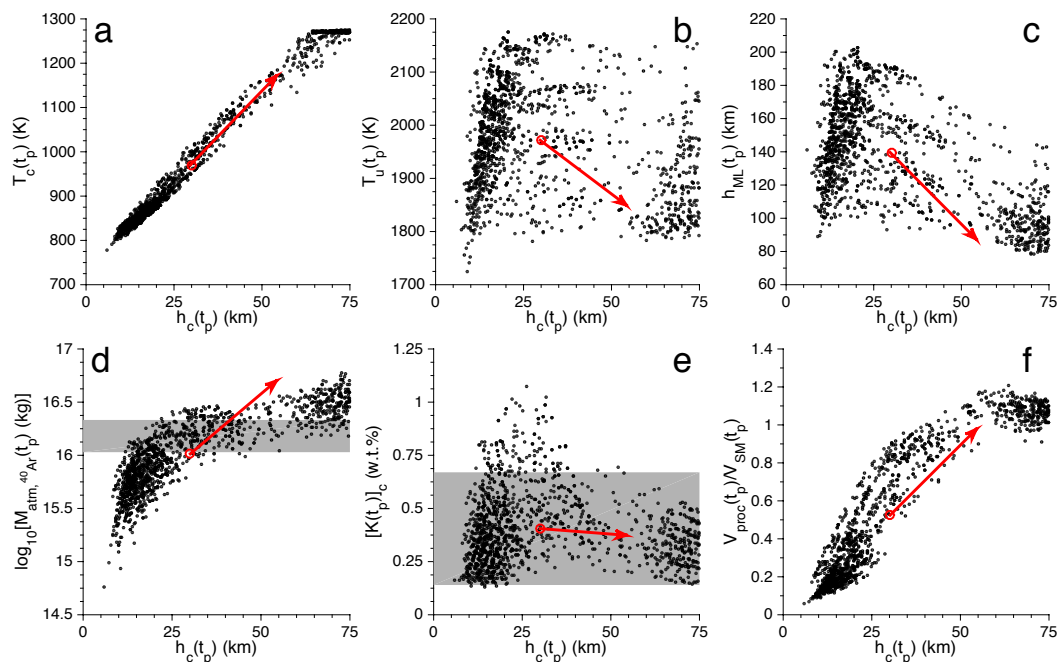


Figure 6.4: Summary of the results of 1390 simulations of the thermal and chemical evolution of Venus. Panels compare current crustal thickness to present-day values of (a) Moho temperature, (b) mantle potential temperature, (c) mantle lithosphere thickness, (d) atmospheric mass of radiogenic argon, (e) crustal abundance of potassium, and (f) fraction of the source mantle that has been processed by partial melting. The red arrows are projections of the first principal component basis vector emanating from points representing the averaged simulation results. This vector indicates the axis accounting for the majority of the variance in the dataset, as explained in the text. The present-day atmospheric mass of radiogenic argon ($1-\sigma$ interval) and the range of measured crustal abundances of potassium are shown as shaded gray regions in (d) and (e), respectively.

and maximum core/mantle temperature contrasts are 87 K and 284 K, respectively, for simulations that satisfy the argon constraint within $1-\sigma$ and predict present-day core cooling. Simulations that have present-day crustal thicknesses up to 75 km can predict the observed amount of argon degassing within $1-\sigma$. But all but three simulations with $h_c(t_p) > 50$ km fail to predict recent resurfacing and core cooling. Decreasing the assumed efficiency of argon degassing on Venus could proportionally increase this limit on the amount of crustal production that can occur throughout geologic time.

To further examine the first-order correlations between the simulation results, we calculate and project the first principal component basis vector, which is the axis representing the majority (51.85%) of the variance in the output dataset (e.g., O'Rourke

and Korenaga, 2012). Coefficients in the basis vector, listed under Π_1 in Table 6.2, could range from -1 to 1 in principle. Large absolute values indicate coefficients that are important to explaining the variance in the dataset. If two parameters have opposite or identical signs, then they are anticorrelated or correlated, respectively. Arrows representing projections of the basis vector are also plotted in Fig. 6.4. Basis vectors have no preferred polarity, so the signs of the values and directions of the arrows could all be reversed with no loss of information.

Crustal production is the dominant factor controlling variance in the simulation results. Three of the largest coefficients in the basis vector are associated with T_c (0.34), h_c (0.32), and V_{proc}/V_{SM} (0.32). Visual inspection of Fig. 6.4 confirms that thick crust is typically hot, and producing thick crust requires a high degree of mantle processing. Other correlations between parameters in the basis vector have physical explanations. The thicknesses of both the ML and the DML are strongly anticorrelated with crustal thickness (coefficients of -0.33) because the relatively hot mantle that produces thick crust tends to destabilize the DML. Increasing $V_{proc}(t_p)$ promotes additional ^{40}Ar degassing and a larger absolute mass of K tends to partition into the crust, although $[\text{K}(t_p)]_c$ may actually decrease as crustal volume increases. Note that the mantle still retains volatiles with $V_{proc} > V_{SM}$ because it is assumed to homogenize between each episode of melting.

A linear function of initial conditions provides a quick, simple way to roughly estimate present-day model parameters (e.g., O'Rourke and Korenaga, 2012). The general formula is

$$P_i(t_p) = C_{i,0} + C_{i,1}T_{u,n}(0) + C_{i,2}T_{cm,n}(0) + C_{i,3}[\log_{10}(\eta_0)]_n \quad (6.36) \\ + C_{i,4}[U(t_p)]_{PM,n} + C_{i,5}(\text{K/U})_n + C_{i,6}E_n,$$

where P_i is the present-day value of the i th output parameter; constants $C_{i,0}$ through $C_{i,4}$ are calculated using the least squares method for each P_i ; and each subscript n indicates that the input parameters are mean-subtracted and normalized by their standard deviations, while the output parameters remain dimensional. Table 6.2 contains the calculated best-fit coefficients and the correlation coefficients between predicted values and model output, where numbers close to 1 indicate a good fit. The utilized values for the average and standard deviation of the input parameters are also listed.

Values of $C_{i,1}$ through $C_{i,6}$ indicate which initial conditions are most important to the simulation results. For instance, η_0 mostly controls how hot the mantle is at

present, along with $[U]_{PM}$. Crustal thickness, in contrast, depends slightly more on the initial temperatures of the core and mantle, since most crustal production occurs in early epochs. Since the mantle insulates the core, the temperature of the core today depends largely on the initial interior temperatures and η_0 , which govern how quickly the mantle loses heat. Increasing E generally leads to an increased present-day Moho temperature and slightly thicker crust, but also to lower temperatures of the mantle and core that cause decreased mantle heat flux and lithosphere thickness.

Although many combinations of initial conditions produce too much or too little degassing, all values of individual initial conditions are represented in the suite of simulations with the correct amount of argon degassing and recent volcanism. Any choice of $[U(t_p)]_{PM}$, for example, is permissible if other parameters are suitably adjusted. Each initial condition except E is of roughly equal importance. Increased mantle viscosity inhibits argon degassing by decreasing convective velocities and thus melt production. High internal temperatures and radiogenic heating promote argon degassing, so Venus cannot have extreme values of all these initial conditions unless some of our fundamental assumptions about planetary evolution are incorrect.

The predictive power of the best-fit linear functions for most model parameters is quite good. Correlation coefficients for present-day values of F_s , F_m , h_{DML} , and h_{ML} are quite high even though they can exhibit variability over short time intervals during simulations. The best-fit function tends to fail near extreme values of some parameters. For example, while crustal thickness is well predicted in general, the best-fit function underestimates crustal thickness for $h_c < 10$ km by predicting unphysical, negative values. Likewise, the best-fit function for Moho temperature returns poor predictions for the coldest and hottest temperatures. As seen in Fig. 6.4, basal melting in the crust causes non-linearity for high Moho temperatures, whereas the large number of simulations with extremely cold initial conditions harms the fit for Moho temperatures close to the surface temperature. Linear functions for key model results can be used to quickly guess whether a given set of initial conditions will yield present-day parameters consistent with observational constraints. However, thermal evolution simulations are still required to confirm these approximate predictions.

The simulation shown in Fig. 6.3 was repeated 50 times with f varied between the extreme values of 0.01 and 0.5. For the nominal value of $f = 0.25$, $\Delta h_{c,0.5} = 132$ m is the globally averaged increase in crustal thickness during the last 0.5 Gyr. This value remains essentially unchanged as f is decreased to 0.01. However, setting f

P_i	Π_1	$C_{i,0}$	$C_{i,1}$	$C_{i,2}$	$C_{i,3}$	$C_{i,4}$	$C_{i,5}$	$C_{i,6}$	Units	Corr.
$T_c(t_p)$	0.34	969.76	73.35	74.76	-100.77	91.30	52.16	38.95	K	0.83
$T_u(t_p)$	-0.24	1971.73	23.35	22.83	71.27	38.58	18.75	-19.13	K	0.94
$T_{cm}(t_p)$	-0.19	3567.40	41.13	46.86	80.25	49.73	26.43	-21.32	K	0.98
$h_c(t_p)$	0.32	30.09	10.14	10.00	-12.30	12.23	7.07	5.13	km	0.82
$h_{DML}(t_p)$	-0.33	136.55	0.32	-1.40	27.47	1.83	0.22	-8.55	km	0.88
$h_{ML}(t_p)$	-0.33	139.61	1.46	-1.12	25.13	2.18	0.50	-6.77	km	0.87
$F_s(t_p)$	0.32	40.31	1.41	1.05	-3.88	3.41	1.51	1.16	mW m ⁻²	0.83
$F_m(t_p)$	-0.02	29.36	-1.72	-1.17	-0.44	-1.86	-1.03	-0.33	mW m ⁻²	0.83
$V_{proc}(t_p)/V_{SM}(t_p)$	0.32	0.52	0.22	0.14	-0.23	0.25	0.14	0.10	-	0.89
$M_{atm,^{40}Ar}(t_p)$	0.27	16.01	0.21	0.11	-0.21	0.25	0.22	0.08	log ₁₀ (kg)	0.98
$[K(t_p)]_c$	-0.03	0.41	0.03	-0.04	0.00	0.08	0.11	0.00	w.t.%	0.78

Table 6.2: First principal component basis vector (Π_1) and coefficients for the best-fit linear function relating present-day parameter values ($C_{i,0}$ through $C_{i,6}$). Correlation coefficients quantifying the correspondence between the actual and predicted output parameters are also included. To calculate the best-fit function, the input parameters were first mean-subtracted using their average values: $E = 337.27$ kJ mol⁻¹, $K/U = 10103$, $[U(t_p)]_{PM} = 16.14$ ppb, $T_u(0) = 1588.63$ K, $T_{cm}(0) = 4172.66$ K, and $\log_{10}(\eta_0) = 19.88$. They were then normalized by 41.03 kJ mol⁻¹, 2645, 2.70 ppb, 100.93 K, 167.42 K, and 0.55, respectively.

= 0.4 to 0.5 increases the heat flux from mantle plumes during the early evolution of Venus, causing efficient cooling of the mantle and limiting the recent increase in crustal thickness to $\Delta h_{c,0.5} = \sim 70$ m. However, high melt fractions during early evolution cause the total crustal production to increase by ~ 5 to 10 km. In contrast, $h_c(t_p) = 22$ km when $f = 0.01$, a decrease of 8 km from the nominal result. The total amount of argon degassing is less sensitive to changes in f , varying by $\sim 12\%$ (or $0.35\text{-}\sigma$) over the entire range of values. Mantle plumes that upwell relatively late in the evolution of Venus have little effect on the present-day atmospheric abundance of radiogenic argon because most mantle processing and sequestration of ⁴⁰K in the crust occurs early.

6.7 Discussion

Thermal evolution of Venus

Stagnant-lid convection is perhaps the expected regime of mantle dynamics for Venus. Introducing plate tectonics or additional mechanisms for surface recycling requires substantial justification, especially because the initialization of plate tectonics on Earth largely remains a mystery (e.g., Korenaga, 2013). Deviations from the stagnant-lid regime have been incorporated into models of the evolution of Venus to explain a putative global resurfacing event at ~ 500 Ma. However, if the requirement for a rapid, global resurfacing event is rejected in favor of more gradual resurfacing (e.g., Guest and Stofan, 1999; Hansen and Lopez, 2010; O'Rourke,

Wolf, et al., 2014), a model of stagnant-lid convection can reproduce significant features of present-day Venus to first order. In particular, both decompression melting of passively upwelling mantle and volcanism from mantle plumes can explain the young-looking surface of Venus. Melting of passive upwellings is relatively more important to recent crustal production and argon degassing, but mantle plumes may have important effects on local geology.

Thermal evolution models that satisfy the argon constraint are non-unique (e.g., O'Neill et al., 2014), just as the observed geological features and cratering statistics admit a range of possible evolutionary scenarios. For example, a single episode of mantle melting during a catastrophic resurfacing event releases the requisite mass of radiogenic argon for crustal thicknesses of ~10 to 50 km, within the estimated present-day range (e.g., James et al., 2013). Unlike simulations of stagnant-lid convection, the suitability of this simple model is not sensitive to the uncertainties in the chemical composition of Venus. Of course, a history with only one melting event is both extremely simplistic and highly unlikely, but it serves to demonstrate the important caveat that argon degassing alone does not unambiguously point towards a single path for the thermal evolution of Venus.

Many important issues await further study. We calculated approximate surface ages based on the global average of crustal thickness, but the fraction of melt production that causes resurfacing is uncertain. That is, the ratio of extrusive to intrusive volcanism depends on the poorly known density difference between melt and solid phases in the crust and lithosphere of Venus, which is probably a complicated function of composition and depth (e.g., Crisp, 1984; White et al., 2006; Reese, Solomatov, and Orth, 2007). A higher fraction of intrusive magmatism mandates a larger amount of recent melt production to explain the young-looking surface of Venus. The total crustal production cannot exceed ~65 km, however, without violating the argon constraint unless argon is actually compatible in basaltic magma and/or diffusion is slow (e.g., Watson et al., 2007). Intriguingly, Watson et al. (2007) invoked hydration of oceanic lithosphere to release ^{40}Ar into Earth's atmosphere, which seems to imply that ^{40}Ar in the atmosphere of Venus is evidence that stable, water oceans existed in the past. On the other hand, the interpretation of their data is controversial, and the behavior of ^{40}Ar might actually match conventional assumptions (e.g., Namiki and Solomon, 1998; Kaula, 1999; Cassata et al., 2011).

Our simulations generally predict that the core continuously cools. The calculated temperature differences across the core/mantle boundary are typically near the val-

ues considered sufficient to drive plumes with high ($\sim 10^3 \text{ kg s}^{-1}$) buoyancy fluxes (Smrekar and Sotin, 2012). Models of the evolution of the core could include additional complications to possibly better match observational evidence for mantle plumes. Our simulations do not include heat-producing elements like potassium or uranium in the core, although experimental evidence typically favors <80 ppm of potassium in Earth's core, corresponding to <0.5 TW of radiogenic heating (e.g., Corgne et al., 2007). More generally, we assume that the entire core is homogenous and convective. Future studies must also consider the possibly high thermal conductivity and compositional stratification that may develop during accretion (e.g., Pozzo et al., 2012; Rubie, Jacobson, et al., 2015). Unfortunately, the structure and composition of the core of Venus is essentially unconstrained. Introducing these additional complications will only increase the flexibility of our models, reinforcing our conclusion that continuous evolution in the stagnant-lid regime is consistent with available observations.

Comparison with other studies

Any one-dimensional, parameterized model suffers some shortcomings. We cannot address the relationship between gravity and topography on Venus, which is an important constraint on higher-dimensional models (e.g., Armann and Tackley, 2012). More importantly, our fundamental assumption is that scaling laws developed for steady-state convection yield reasonably good approximations for the properties of the convective system at each time step. When crustal formation occurs, for example, the associated loss of potassium and argon is assumed to instantly decrease their respective abundances in the entire convecting mantle. This approach has been validated for simple systems with uniform viscosity or purely temperature-dependent viscosity (e.g., Daly, 1980; Choblet and Sotin, 2000). But steady-state models are probably ill-suited to capturing transient events that likely occurred during the early evolution of Venus, like the crystallization of a magma ocean (e.g., Solomatov and Stevenson, 1993) and large impacts (e.g., Agnor et al., 1999). Furthermore, our models do not accommodate transitions in convective regimes or layered mantle convection, as has been proposed for Venus (e.g., Papuc and Davies, 2012; Ogawa and Yanagisawa, 2014).

Armann and Tackley (2012) argued that continuous evolution in the stagnant-lid regime tends to produce an unrealistically high rate of recent resurfacing. Our methods and conclusions differ in several respects. Their choice of radiogenic heating in the mantle corresponds to the canonical $[\text{U}(t_p)]_{PM} = 21 \text{ ppb}$ and K/U

= 7220, whereas we consider a wider range of possible values consistent with uncertainties on the composition of bulk silicate Earth (Lyubetskaya and Korenaga, 2007a). Moreover, Armann and Tackley (2012) include geochemically dubious concentrations of potassium in the core: 400 to 800 ppm, which produce ~ 3 to 6 TW of extra heating. Crustal recycling in their models prevents all heat-producing elements from partitioning into the crust, despite a relatively large amount of mantle processing. We do not include crustal recycling here, which is partially justified because crust thick enough to transition to eclogite and sink into the mantle tends to violate the argon constraint under the assumption of efficient degassing. Ultimately, we agree that roughly half of the total inventory of heat-producing elements is plausibly sequestered in the crust of Venus. Of course, we do not use the low values for yield stress that Armann and Tackley (2012) introduced to produce catastrophic resurfacing events.

Our different treatments of mantle melting are also responsible for our divergent results. Armann and Tackley (2012) predict that melt migration is the primary mode of heat transport, whereas our results suggest that conduction through the upper thermal boundary layer is relatively more important. In our models, partial melting of the mantle forms a depleted layer in the lithosphere that impedes further magmatism. Armann and Tackley (2012) make an “end-member assumption” that any melt produced in a zone with depth up to 600 km is instantaneously extruded onto the surface, justified by the likely fact that buoyant melt moves faster than the average convective velocity. Depleted material is thus left behind and may be efficiently recycled deep in the convecting mantle. Consequently, our models respond differently to changes in the reference viscosity. We find that higher mantle viscosity inhibits melt productivity by slowing material transport through the melting zone, but Armann and Tackley (2012) produce more melting with higher viscosity because mantle temperatures rise and the melting zone grows larger.

Parameterized models ultimately complement direct simulations of planetary evolution that include additional complications. Direct simulations are often sensitive to values of parameters that are poorly constrained by observations, such as reference viscosity, melt transport, and density differences between various mantle phases (e.g., Armann and Tackley, 2012; Ogawa and Yanagisawa, 2014). The computational expense of running a complete sensitivity analysis on direct simulations is potentially prohibitive. So, parameterized models remain valuable because they are relatively straightforward to understand and the effects of various assumptions are

easily explored. If direct simulations systematically disagree with predictions from parameterized models, then perhaps new theoretical scalings can be developed that will both help models match observations and increase our understanding of the underlying processes.

6.8 Conclusions

Multiple scenarios for the evolution of Venus may satisfy constraints imposed by surface geology and the present-day atmospheric mass of radiogenic argon. Periodic episodes of global resurfacing are a popular explanation for the young-looking surface of Venus. Indeed, a catastrophic resurfacing event at ~ 500 Ma would produce a crustal thickness and magnitude of argon degassing that match current estimates, even considering the large uncertainties on the chemical composition of Venus. Drastic departures from the stagnant-lid regime of mantle convection, however, would be required to produce short-duration global resurfacing events. Many mechanisms have been proposed, but continuous evolution with a stagnant lid remains the simplest scenario and the default regime of mantle convection, according to theory. Moreover, impact crater statistics and recent geologic mapping are also consistent with resurfacing from localized, non-catastrophic volcanism.

Self-consistent thermal evolution models of stagnant-lid convection can predict the correct amount of argon degassing. Because many important parameters are poorly constrained, sensitivity analyses are critical to determine the relationships between initial conditions and modeling results. Principal component analysis was used to identify the largest source of variations in the simulation output. A linear function of input parameters can predict many parameters of interest to reasonable accuracy. This provides a shortcut to finding the space of initial conditions that will produce, for example, acceptable amounts of argon degassing and crustal and lithosphere thicknesses that match geophysical models. Furthermore, the coefficients in the best-fit function help identify the initial conditions with the strongest control over simulation results. Simulations that satisfy the argon constraint also predict limited core cooling, which prevents dynamo action today but also causes mantle plume upwellings, providing a source of recent volcanism and an explanation for observed surface features on Venus.

BIBLIOGRAPHY

- Agnor, C. B., R. M. Canup, and H. F. Levison (1999). “On the Character and Consequences of Large Impacts in the Late Stage of Terrestrial Planet Formation”. *Icarus* 142.1, pp. 219–237. doi: 10.1006/icar.1999.6201.
- Arevalo, R., W. F. McDonough, and M. Luong (2009). “The K/U ratio of the silicate Earth: Insights into mantle composition, structure and thermal evolution”. *Earth and Planetary Science Letters* 278.3-4, pp. 361–369. doi: 10.1016/j.epsl.2008.12.023.
- Armann, M. and P. J. Tackley (2012). “Simulating the thermochemical magmatic and tectonic evolution of Venus’s mantle and lithosphere: Two-dimensional models”. *Journal of Geophysical Research* 117.E12, E12003. doi: 10.1029/2012JE004231.
- Badro, J., A. S. Côté, and J. P. Brodholt (2014). “A seismologically consistent compositional model of Earth’s core.” *Proceedings of the National Academy of Sciences* 111, pp. 2–5. doi: 10.1073/pnas.1316708111.
- Badro, J., J. Siebert, and F. Nimmo (2016). “An early geodynamo driven by exsolution of mantle components from Earth’s core”. *Nature* 536.7616, pp. 326–328. doi: 10.1038/nature18594.
- Barsukov, V. L. et al. (1986). “The geology and geomorphology of the Venus surface as revealed by the radar images obtained by Veneras 15 and 16”. *Journal of Geophysical Research: Solid Earth* 91.B4, pp. 378–398. doi: 10.1029/JB091iB04p00378.
- Basilevsky, A. T. and J. W. Head (1998). “The geologic history of Venus: A stratigraphic view”. *Journal of Geophysical Research: Planets* 103.E4, pp. 8531–8544. doi: 10.1029/98JE00487.
- Basilevsky, A. T. and J. W. Head (2000). “Geologic units on Venus: evidence for their global correlation”. *Planetary and Space Science* 48.1, pp. 75–111. doi: 10.1016/S0032-0633(99)00083-5.
- Basilevsky, A. T. and J. W. Head (2002). “Venus: Timing and rates of geologic activity”. *Geology* 30.11, p. 1015. doi: 10.1130/0091-7613(2002)030<1015:VTAROG>2.0.CO;2.
- Biggin, A. J., E. J. Piispa, et al. (2015). “Palaeomagnetic field intensity variations suggest Mesoproterozoic inner-core nucleation”. *Nature* 526.7572, pp. 245–248. doi: 10.1038/nature15523.
- Biggin, A. J., M. J. de Wit, et al. (2011). “Palaeomagnetism of Archaean rocks of the Onverwacht Group, Barberton Greenstone Belt (southern Africa): Evidence for a stable and potentially reversing geomagnetic field at ca. 3.5Ga”. *Earth and Planetary Science Letters* 302.3-4, pp. 314–328. doi: 10.1016/j.epsl.2010.12.024.

- Bills, B. G., R. L. Jones, and W. S. Kiefer (1987). "Venus gravity: A harmonic analysis". *Journal of Geophysical Research* 92.B10, pp. 10335–10351. DOI: 10.1029/JB092iB10p10335.
- Bjornnes, E. et al. (2012). "Equilibrium resurfacing of Venus: Results from new Monte Carlo modeling and implications for Venus surface histories". *Icarus* 217.2, pp. 451–461. DOI: 10.1016/j.icarus.2011.03.033.
- Bottke, W. F. et al. (2016). "On Asteroid Impacts, Crater Scaling Laws, and a Proposed Younger Surface Age for Venus". *Lunar and Planetary Science Conference*, p. 2036.
- Brown, C. D. and R. E. Grimm (1996). "Lithospheric rheology and flexure at Artemis Chasma, Venus". *Journal of Geophysical Research: Planets* 101.E5, pp. 12697–12708. DOI: 10.1029/96JE00834.
- Buffett, B. A., E. J. Garnero, and R. Jenaloz (2000). "Sediments at the Top of Earth's Core". *Science* 290.5495, pp. 1338–1342. DOI: 10.1126/science.290.5495.1338.
- Buffett, B. A. (2002). "Estimates of heat flow in the deep mantle based on the power requirements for the geodynamo". *Geophysical Research Letters* 29.12, p. 1566. DOI: 10.1029/2001GL014649.
- Bullock, M. and D. H. Grinspoon (2001). "The Recent Evolution of Climate on Venus". *Icarus* 150.1, pp. 19–37. DOI: 10.1006/icar.2000.6570.
- Byerlee, J. (1978). "Friction of rocks". *Pure and Applied Geophysics PAGEOPH* 116.4-5, pp. 615–626. DOI: 10.1007/BF00876528.
- Canup, R. M. (2008). "Accretion of the Earth." *Phil. Trans. R. Soc. A* 366.1883, pp. 4061–75. DOI: 10.1098/rsta.2008.0101.
- Canup, R. M. (2012). "Forming a Moon with an Earth-like composition via a giant impact." *Science* 338.6110, pp. 1052–5. DOI: 10.1126/science.1226073.
- Cassata, W. S., P. R. Renne, and D. L. Shuster (2011). "Argon diffusion in pyroxenes: Implications for thermochronometry and mantle degassing". *Earth and Planetary Science Letters* 304.3-4, pp. 407–416. DOI: 10.1016/j.epsl.2011.02.019.
- Chambers, J. E. (2004). "Planetary accretion in the inner Solar System". *Earth and Planetary Science Letters* 223.3-4, pp. 241–252. DOI: 10.1016/j.epsl.2004.04.031.
- Chib, S. and E. Greenberg (1995). "Understanding the Metropolis-Hastings algorithm". *Journal of the American Statistical Association* 49.4, pp. 327–335. DOI: 10.2307/2684568.
- Choblet, G. and C. Sotin (2000). "3D thermal convection with variable viscosity: Can transient cooling be described by a quasi-static scaling law?" *Physics of the Earth and Planetary Interiors* 119, pp. 321–336. DOI: 10.1016/S0031-9201(00)00136-9.

- Christensen, U. R. (2010). “Dynamo Scaling Laws and Applications to the Planets”. *Space Science Reviews* 152.1-4, pp. 565–590. DOI: 10.1007/s11214-009-9553-2.
- Christensen, U. R. (1985). “Thermal evolution models for the Earth”. *Journal of Geophysical Research* 90.B4, p. 2995. DOI: 10.1029/JB090iB04p02995.
- Collins, G. C. et al. (1999). “Evidence for rapid regional plains emplacement on Venus from the population of volcanically embayed impact craters”. *Journal of Geophysical Research* 104.E10, p. 24121. DOI: 10.1029/1999JE001041.
- Corgne, A. et al. (2007). “How much potassium is in the Earth’s core? New insights from partitioning experiments”. *Earth and Planetary Science Letters* 256.3-4, pp. 567–576. DOI: 10.1016/j.epsl.2007.02.012.
- Crisp, J. A. (1984). “Rates of magma emplacement and volcanic output”. *Journal of Volcanology and Geothermal Research* 20.3-4, pp. 177–211. DOI: 10.1016/0377-0273(84)90039-8.
- Crumpler, L. S. et al. (1997). “Volcanoes and Centers of Volcanism on Venus”. *Venus II*. Arizona Univ. Press, pp. 697–756.
- Ćuk, M. and S. T. Stewart (2012). “Making the Moon from a fast-spinning Earth: a giant impact followed by resonant despinning.” *Science* 338.6110, pp. 1047–52. DOI: 10.1126/science.1225542.
- Dahl, T. W. and D. J. Stevenson (2010). “Turbulent mixing of metal and silicate during planet accretion — And interpretation of the Hf–W chronometer”. *Earth and Planetary Science Letters* 295.1-2, pp. 177–186. DOI: 10.1016/j.epsl.2010.03.038.
- Daly, S. F. (1980). “Convection with decaying heat sources: constant viscosity”. *Geophysical Journal International* 61.3, pp. 519–547. DOI: 10.1111/j.1365-246X.1980.tb04831.x.
- Driscoll, P. and D. Bercovici (2013). “Divergent evolution of Earth and Venus: Influence of degassing, tectonics, and magnetic fields”. *Icarus* 226.2, pp. 1447–1464. DOI: 10.1016/j.icarus.2013.07.025.
- Driscoll, P. and D. Bercovici (2014). “On the thermal and magnetic histories of Earth and Venus: Influences of melting, radioactivity, and conductivity”. *Physics of the Earth and Planetary Interiors* 236, pp. 36–51. DOI: 10.1016/j.pepi.2014.08.004.
- Elkins-Tanton, L. T. (2011). “Formation of early water oceans on rocky planets”. *Astrophysics and Space Science* 332.2, pp. 359–364. DOI: 10.1007/s10509-010-0535-3.
- Farnetani, C. G. (1997). “Excess temperature of mantle plumes: The role of chemical stratification across D””. *Geophysical Research Letters* 24.13, pp. 1583–1586. DOI: 10.1029/97GL01548.

- Fegley, B. and R. Prinn (1989). “Estimation of the rate of volcanism on Venus from reaction rate measurements”. *Nature* 337, pp. 55–58.
- Fischer, R. A. et al. (2015). “High pressure metal–silicate partitioning of Ni, Co, V, Cr, Si, and O”. *Geochimica et Cosmochimica Acta* 167, pp. 177–194. DOI: 10.1016/j.gca.2015.06.026.
- Ford, P. G. and G. H. Pettengill (1992). “Venus topography and kilometer-scale slopes”. *Journal of Geophysical Research* 97.E8, p. 13103. DOI: 10.1029/92JE01085.
- Fourel, L., S. Goes, and G. Morra (2014). “The role of elasticity in slab bending”. *Geochemistry, Geophysics, Geosystems* 15.11, pp. 4507–4525. DOI: 10.1002/2014GC005535.
- Fowler, A. and S. O’Brien (1996). “A mechanism for episodic subduction on Venus”. *Journal of Geophysical Research* 101, pp. 4755–4763.
- Fraeman, A. A. and J. Korenaga (2010). “The influence of mantle melting on the evolution of Mars”. *Icarus* 210.1, pp. 43–57. DOI: 10.1016/j.icarus.2010.06.030.
- French, S. W. and B. Romanowicz (2015). “Broad plumes rooted at the base of the Earth’s mantle beneath major hotspots”. *Nature* 525.7567, pp. 95–99. DOI: 10.1038/nature14876.
- Gerya, T. V. (2014). “Plume-induced crustal convection: 3D thermomechanical model and implications for the origin of novae and coronae on Venus”. *Earth and Planetary Science Letters* 391, pp. 183–192. DOI: 10.1016/j.epsl.2014.02.005.
- Gillmann, C. and P. Tackley (2014). “Atmosphere/mantle coupling and feedbacks on Venus”. *Journal of Geophysical Research: Planets* 119.6, pp. 1189–1217. DOI: 10.1002/2013JE004505.
- Glaze, L. S. et al. (2002). “Insights into Corona Formation Through Statistical Analyses”. *Journal of Geophysical Research* 107.E12, p. 5135. DOI: 10.1029/2002JE001904.
- Gomi, H. et al. (2013). “The high conductivity of iron and thermal evolution of the Earth’s core”. *Physics of the Earth and Planetary Interiors* 224, pp. 88–103. DOI: 10.1016/j.pepi.2013.07.010.
- Grindrod, P. M. and T. Hoogenboom (2006). “Venus: The corona conundrum”. *Astronomy and Geophysics* 47.3, pp. 3.16–3.21. DOI: 10.1111/j.1468-4004.2006.47316.x.
- Gubbins, D. (1977). “Energetics of Earth’s Core”. *Journal of Geophysics-Zeitschrift Fur Geophysik* 43, pp. 453–464.
- Guest, J. and E. R. Stofan (1999). “A New View of the Stratigraphic History of Venus”. *Icarus* 139.1, pp. 55–66. DOI: 10.1006/icar.1999.6091.

- Hansen, V. and I. Lopez (2010). “Venus records a rich early history”. *Geology* 38.4, pp. 311–314. DOI: 10.1130/G30587.1.
- Hauck, S. A. and R. J. Phillips (2002). “Thermal and crustal evolution of Mars”. *Journal of Geophysical Research* 107.E7, pp. 1–19. DOI: 10.1029/2001JE001801.
- Hauck, S. A., R. J. Phillips, and M. H. Price (1998). “Venus: Crater distribution and plains resurfacing models”. *Journal of Geophysical Research* 103.E6, p. 13635. DOI: 10.1029/98JE00400.
- Head, J. W. et al. (1992). “Venus volcanism: Classification of volcanic features and structures, associations, and global distribution from Magellan data”. *Journal of Geophysical Research* 97.E8, p. 13153. DOI: 10.1029/92JE01273.
- Helffrich, G. (2014). “Outer core compositional layering and constraints on core liquid transport properties”. *Earth and Planetary Science Letters* 391, pp. 256–262. DOI: 10.1016/j.epsl.2014.01.039.
- Hernlund, J. and A. McNamara (2015). “The Core-Mantle Boundary Region”. *Treatise on Geophysics*. Elsevier B.V., pp. 461–519. DOI: 10.1016/B978-0-444-53802-4.00136-6.
- Herrick, R. R. and R. J. Phillips (1994). “Implications of a Global Survey of Venusian Impact Craters”. *Icarus* 111.2, pp. 387–416. DOI: 10.1006/icar.1994.1152.
- Herrick, R. R. and M. E. Rumpf (2011). “Postimpact modification by volcanic or tectonic processes as the rule, not the exception, for Venusian craters”. *Journal of Geophysical Research* 116.E2, E02004. DOI: 10.1029/2010JE003722.
- Herrick, R. R. and V. L. Sharpton (2000). “Implications from stereo-derived topography of Venusian impact craters”. *Journal of Geophysical Research* 105.E8, p. 20245. DOI: 10.1029/1999JE001225.
- Herrick, R. R., V. L. Sharpton, et al. (1997). “Morphology and Morphometry of Impact Craters”. *Venus II*. Arizona Univ. Press, pp. 1015–1046.
- Herrick, R. R., D. L. Stahlke, and V. L. Sharpton (2012). “Fine-scale Venusian topography from Magellan stereo data”. *Eos* 93.12, pp. 125–126. DOI: 10.1029/2012E0120002.
- Herzberg, C., K. Condie, and J. Korenaga (2010). “Thermal history of the Earth and its petrological expression”. *Earth and Planetary Science Letters* 292.1-2, pp. 79–88. DOI: 10.1016/j.epsl.2010.01.022.
- Hilst, R. D. van der, S. Widiyantoro, and E. R. Engdahl (1997). “Evidence for deep mantle circulation from global tomography”. *Nature* 386.6625, pp. 578–584. DOI: 10.1038/386578a0.
- Hoogenboom, T. and G. A. Houseman (2006). “Rayleigh-Taylor instability as a mechanism for corona formation on Venus”. *Icarus* 180.2, pp. 292–307. DOI: 10.1016/j.icarus.2005.11.001.

- Hoogenboom, T., G. A. Houseman, and P. Martin (2005). “Elastic thickness estimates for coronae associated with chasmata on Venus”. *Journal of Geophysical Research* 110.E9, E09003. doi: 10.1029/2004JE002394.
- Hoogenboom, T., S. E. Smrekar, et al. (2004). “Admittance survey of type 1 coronae on Venus”. *Journal of Geophysical Research* 109.E3, E03002. doi: 10.1029/2003JE002171.
- Ivanov, M. A. and J. W. Head (2011). “Global geological map of Venus”. *Planetary and Space Science* 59.13, pp. 1559–1600. doi: 10.1016/j.pss.2011.07.008.
- Ivanov, M. A. and J. W. Head (2013). “The history of volcanism on Venus”. *Planetary and Space Science* 84, pp. 66–92. doi: 10.1016/j.pss.2013.04.018.
- Izenberg, N. R., R. E. Arvidson, and R. J. Phillips (1994). “Impact crater degradation on venusian plains”. *Geophysical Research Letters* 21.4, pp. 289–292. doi: 10.1029/94GL00080.
- Jacobson, S. A. et al. (2015). “A Late Giant Impact Is Necessary To Create Earth’s Magnetic Field”. *Lunar and Planetary Science Conference*, p. 1882.
- James, P. B., M. T. Zuber, and R. J. Phillips (2013). “Crustal thickness and support of topography on Venus”. *Journal of Geophysical Research: Planets* 118.4, pp. 859–875. doi: 10.1029/2012JE004237.
- Janes, D. M. et al. (1992). “Geophysical models for the formation and evolution of coronae on Venus”. *Journal of Geophysical Research* 97.E10, p. 16055. doi: 10.1029/92JE01689.
- Jaupart, C., S. Labrosse, and J.-C. Mareschal (2007). “Temperatures, Heat and Energy in the Mantle of the Earth”. *Treatise on Geophysics*. Elsevier, pp. 253–303. doi: 10.1016/B978-044452748-6.00114-0.
- Johnson, C. L. and D. T. Sandwell (1994). “Lithospheric flexure on Venus”. *Geophysical Journal International* 119.2, pp. 627–647. doi: 10.1111/j.1365-246X.1994.tb00146.x.
- Karato, S. and P. Wu (1993). “Rheology of the Upper Mantle: A Synthesis”. *Science* 260.5109, pp. 771–8. doi: 10.1126/science.260.5109.771.
- Kaula, W. (1999). “Constraints on Venus Evolution from Radiogenic Argon”. *Icarus* 139.1, pp. 32–39. doi: 10.1006/icar.1999.6082.
- Kaula, W. (1995). “Venus Reconsidered”. *Science* 798.1989.
- Kaula, W. and R. Phillips (1981). “Quantitative Tests for Plate Tectonics on Venus”. *Geophysical Research Letters* 8.12, pp. 1187–1190.
- Koch, D. M. and M. Manga (1996). “Neutrally buoyant diapirs: A model for venus coronae”. *Geophysical Research Letters* 23.3, pp. 225–228. doi: 10.1029/95GL03776.

- Koker, N. de, G. Steinle-Neumann, and V. Vlcek (2012). “Electrical resistivity and thermal conductivity of liquid Fe alloys at high P and T, and heat flux in Earth’s core.” *Proceedings of the National Academy of Sciences* 109.11, pp. 4070–3. DOI: 10.1073/pnas.1111841109.
- Konôpková, Z. et al. (2016). “Direct measurement of thermal conductivity in solid iron at planetary core conditions”. *Nature* 534.7605, pp. 99–101. DOI: 10.1038/nature18009.
- Korenaga, J. (2006). “Archean geodynamics and the thermal evolution of Earth”. *Archean Geodynamics and Environments* 164, pp. 7–32. DOI: 10.1029/164gm03.
- Korenaga, J. (2011). “Thermal evolution with a hydrating mantle and the initiation of plate tectonics in the early Earth”. *Journal of Geophysical Research* 116.B12, B12403. DOI: 10.1029/2011JB008410.
- Korenaga, J. (2002). “Methods for resolving the origin of large igneous provinces from crustal seismology”. *Journal of Geophysical Research* 107.B9. DOI: 10.1029/2001JB001030.
- Korenaga, J. (2005). “Firm mantle plumes and the nature of the core–mantle boundary region”. *Earth and Planetary Science Letters* 232.1-2, pp. 29–37. DOI: 10.1016/j.epsl.2005.01.016.
- Korenaga, J. (2007). “Thermal cracking and the deep hydration of oceanic lithosphere: A key to the generation of plate tectonics?” *Journal of Geophysical Research* 112.B5, pp. 1–20. DOI: 10.1029/2006JB004502.
- Korenaga, J. (2008). “Urey ratio and the structure and evolution of Earth’s mantle”. *Reviews of Geophysics* 46.2, RG2007. DOI: 10.1029/2007RG000241.
- Korenaga, J. (2009). “Scaling of stagnant-lid convection with Arrhenius rheology and the effects of mantle melting”. *Geophysical Journal International* 179.1, pp. 154–170. DOI: 10.1111/j.1365-246X.2009.04272.x.
- Korenaga, J. (2010a). “On the Likelihood of Plate Tectonics on Super-Earths: Does Size Matter?” *The Astrophysical Journal Letters* 725.1, pp. L43–L46. DOI: 10.1088/2041-8205/725/1/L43.
- Korenaga, J. (2010b). “Scaling of plate tectonic convection with pseudoplastic rheology”. *Journal of Geophysical Research* 115.B11, pp. 1–24. DOI: 10.1029/2010JB007670.
- Korenaga, J. (2012). “Plate tectonics and planetary habitability: current status and future challenges”. *Annals of the New York Academy of Sciences* 1260, pp. 87–94. DOI: 10.1111/j.1749-6632.2011.06276.x.
- Korenaga, J. (2013). “Initiation and Evolution of Plate Tectonics on Earth: Theories and Observations”. *Annual Review of Earth and Planetary Sciences* 41.1, pp. 117–151. DOI: 10.1146/annurev-earth-050212-124208.

- Labrosse, S., J. W. Hernlund, and N. Coltice (2007). “A crystallizing dense magma ocean at the base of the Earth’s mantle.” *Nature* 450.7171, pp. 866–9. DOI: 10.1038/nature06355.
- Labrosse, S. (2015). “Thermal evolution of the core with a high thermal conductivity”. *Physics of the Earth and Planetary Interiors* 247, pp. 36–55. DOI: 10.1016/j.pepi.2015.02.002.
- Labrosse, S., J.-P. Poirier, and J.-L. Le Mouél (2001). “The age of the inner core”. *Earth and Planetary Science Letters* 190.3-4, pp. 111–123. DOI: 10.1016/S0012-821X(01)00387-9.
- Landuyt, W. and D. Bercovici (2009). “Variations in planetary convection via the effect of climate on damage”. *Earth and Planetary Science Letters* 277.1-2, pp. 29–37. DOI: 10.1016/j.epsl.2008.09.034.
- Lay, T., J. Hernlund, and B. A. Buffett (2008). “Core–mantle boundary heat flow”. *Nature Geoscience* 1.1, pp. 25–32. DOI: 10.1038/ngeo.2007.44.
- Lenardic, A., A. Jellinek, and L.-N. Moresi (2008). “A climate induced transition in the tectonic style of a terrestrial planet”. *Earth and Planetary Science Letters* 271.1-4, pp. 34–42. DOI: 10.1016/j.epsl.2008.03.031.
- Leng, W. and S. Zhong (2008). “Controls on plume heat flux and plume excess temperature”. *Journal of Geophysical Research: Solid Earth* 113.4, pp. 1–15. DOI: 10.1029/2007JB005155.
- Lyubetskaya, T. and J. Korenaga (2007a). “Chemical composition of Earth’s primitive mantle and its variance: 1. Method and results”. *Journal of Geophysical Research* 112.B3, B03211. DOI: 10.1029/2005JB004223.
- Lyubetskaya, T. and J. Korenaga (2007b). “Chemical composition of Earth’s primitive mantle and its variance: 2. Implications for global geodynamics”. *Journal of Geophysical Research* 112.B3, B03212. DOI: 10.1029/2005JB004224.
- Mackwell, S. J., M. E. Zimmerman, and D. L. Kohlstedt (1998). “High-temperature deformation of dry diabase with application to tectonics on Venus”. *Journal of Geophysical Research: Solid Earth* 103.B1, pp. 975–984. DOI: 10.1029/97JB02671.
- Markwardt, C. B. (2009). “Non-linear Least Squares Fitting in IDL with MPFIT”. arXiv: 0902.2850.
- McDonough, W. and S. Sun (1995). “The composition of the Earth”. *Chemical Geology* 120.3-4, pp. 223–253. DOI: 10.1016/0009-2541(94)00140-4.
- McDonough, W. F. (2001). “The composition of the Earth”. *Earthquake Thermodynamics and Phase Transformation in the Earth’s Interior*. Vol. 76. International Geophysics. Elsevier, pp. 3–23. DOI: 10.1016/S0074-6142(01)80077-2.

- McGovern, P. J., M. E. Rumpf, and J. R. Zimbelman (2013). “The influence of lithospheric flexure on magma ascent at large volcanoes on Venus”. *Journal of Geophysical Research: Planets* 118, pp. 2423–2437. DOI: 10.1002/2013JE004455.
- McKinnon, W. B. et al. (1997). “Cratering on Venus: Models and observations”. *Venus II*. Arizona Univ. Press, pp. 969–1014.
- McNutt, M. K. (1984). “Lithospheric flexure and thermal anomalies”. *Journal of Geophysical Research: Solid Earth* 89.B13, pp. 11180–11194. DOI: 10.1029/JB089iB13p11180.
- Moore, W. B. and A. G. Webb (2013). “Heat-pipe Earth”. *Nature* 501.7468, pp. 501–5. DOI: 10.1038/nature12473.
- Moresi, L. M. and V. Solomatov (1998). “Mantle convection with a brittle lithosphere: thoughts on the global tectonic styles of the Earth and Venus”. *Geophysical Journal International* 133.3, pp. 669–682. DOI: 10.1046/j.1365-246X.1998.00521.x.
- Mueller, S. and R. J. Phillips (1995). “On the reliability of lithospheric constraints derived from models of outer-rise flexure”. *Geophysical Journal International* 123.3, pp. 887–902. DOI: 10.1111/j.1365-246X.1995.tb06896.x.
- Nakagawa, T. and P. J. Tackley (2010). “Influence of initial CMB temperature and other parameters on the thermal evolution of Earth’s core resulting from thermochemical spherical mantle convection”. *Geochemistry Geophysics Geosystems* 11.6. DOI: 10.1029/2010GC003031.
- Namiki, N. and S. C. Solomon (1993). “The gabbro-eclogite phase transition and the elevation of mountain belts on Venus”. *Journal of Geophysical Research* 98.E8, p. 15025. DOI: 10.1029/93JE01626.
- Namiki, N. and S. C. Solomon (1998). “Volcanic degassing of argon and helium and the history of crustal production on Venus”. *Journal of Geophysical Research* 103.E2, p. 3655. DOI: 10.1029/97JE03032.
- Nimmo, F. (2015). “Energetics of the Core”. *Treatise on Geochemistry: Second Edition*. Vol. 1. Elsevier B.V., pp. 31–65. DOI: 10.1016/B978-044452748-6.00128-0.
- Nimmo, F. (2002). “Why does Venus lack a magnetic field?” *Geology* 30.11, p. 987. DOI: 10.1130/0091-7613(2002)030<0987:WDVLAM>2.0.CO;2.
- Nimmo, F. and D. McKenzie (1998). “Volcanism and tectonics on Venus”. *Annual Review of Earth and Planetary Sciences* 26, pp. 23–51.
- Nimmo, F. and D. J. Stevenson (2001). “Estimates of Martian crustal thickness from viscous relaxation of topography”. *Journal of Geophysical Research* 106.E3, pp. 5085–5098.

- Noack, L., D. Breuer, and T. Spohn (2012). “Coupling the atmosphere with interior dynamics: Implications for the resurfacing of Venus”. *Icarus* 217.2, pp. 484–498. DOI: 10.1016/j.icarus.2011.08.026.
- Nomura, R. et al. (2012). “Partitioning of potassium into the Earth’s core and implications for thermal history of the Earth”. *AGU Fall Meeting Abstracts* DI33A–2411.
- Ogawa, M. and T. Yanagisawa (2014). “Mantle evolution in Venus due to magmatism and phase transitions: From punctuated layered convection to whole-mantle convection”. *Journal of Geophysical Research: Planets* 119, pp. 867–883. DOI: 10.1002/2013JE004593.
- Ogihara, M., S. Ida, and A. Morbidelli (2007). “Accretion of terrestrial planets from oligarchs in a turbulent disk”. *Icarus* 188.2, pp. 522–534. DOI: 10.1016/j.icarus.2006.12.006.
- Ohta, K. et al. (2016). “Experimental determination of the electrical resistivity of iron at Earth’s core conditions”. *Nature* 534.7605, pp. 95–98. DOI: 10.1038/nature17957.
- Olson, P. et al. (2013). “Controls on geomagnetic reversals and core evolution by mantle convection in the Phanerozoic”. *Physics of the Earth and Planetary Interiors* 214, pp. 87–103. DOI: 10.1016/j.pepi.2012.10.003.
- O’Neill, C. et al. (2014). “Mantle Convection and Outgassing on Terrestrial Planets”. *Comparative Climatology of Terrestrial Planets*. Tucson: Univ. of Arizona Press, pp. 473–486. DOI: 10.2458/azu_uapress_9780816530595-ch19.
- O’Rourke, J. G. and J. Korenaga (2012). “Terrestrial planet evolution in the stagnant-lid regime: Size effects and the formation of self-destabilizing crust”. *Icarus* 221.2, pp. 1043–1060. DOI: 10.1016/j.icarus.2012.10.015.
- O’Rourke, J. G. and J. Korenaga (2015). “Thermal evolution of Venus with argon degassing”. *Icarus* 260, pp. 128–140. DOI: 10.1016/j.icarus.2015.07.009.
- O’Rourke, J. G. and D. J. Stevenson (2016). “Powering Earth’s dynamo with magnesium precipitation from the core”. *Nature* 529.7586, pp. 387–389. DOI: 10.1038/nature16495.
- O’Rourke, J. G., A. S. Wolf, and B. L. Ehlmann (2014). “Venus: Interpreting the spatial distribution of volcanically modified craters”. *Geophysical Research Letters* 41.23, pp. 8252–8260. DOI: 10.1002/2014GL062121.
- Orth, C. P. and V. S. Solomatov (2011). “The isostatic stagnant lid approximation and global variations in the Venusian lithospheric thickness”. *Geochemistry Geophysics Geosystems* 12.7, pp. 1–17. DOI: 10.1029/2011GC003582.
- Palme, H. and H. O’Neill (2013). “Cosmochemical Estimates of Mantle Composition”. *Treatise on Geochemistry: Second Edition*. 2nd ed. Vol. 3. Elsevier Ltd., pp. 1–39. DOI: 10.1016/B978-0-08-095975-7.00201-1.

- Papuc, A. M. and G. F. Davies (2012). “Transient mantle layering and the episodic behaviour of Venus due to the ‘basalt barrier’ mechanism”. *Icarus* 217.2, pp. 499–509. DOI: 10.1016/j.icarus.2011.09.024.
- Phillips, J. L. and C. T. Russell (1987). “Revised upper limit on the internal magnetic moment of Venus”. 92.6, pp. 2253–2263. DOI: 10.1016/0273-1177(87)90232-8.
- Phillips, R. J. (1998). “Geological Evolution of Venus: Rises, Plains, Plumes, and Plateaus”. *Science* 279.5356, pp. 1492–1497. DOI: 10.1126/science.279.5356.1492.
- Phillips, R. J., M. A. Bullock, and S. A. Hauck (2001). “Climate and Interior Coupled Evolution on Venus”. *Geophysical Research Letters* 28.9, pp. 1779–1782.
- Phillips, R. J. and V. L. Hansen (1994). “Tectonic and Magmatic Evolution of Venus”. *Annual Review of Earth and Planetary Sciences* 22.1, pp. 597–656. DOI: 10.1146/annurev.ea.22.050194.003121.
- Phillips, R. J., C. L. Johnson, et al. (1997). “Lithospheric mechanics and dynamics of Venus”. *Venus II*. Ed. by S. W. Bougher, D. M. Hunten, and R. J. Phillips. Tucson: Univ. of Ariz. Press, pp. 1163–1204.
- Phillips, R. J., R. F. Raubertas, et al. (1992). “Impact Craters and Venus Resurfacing History”. *Journal of Geophysical Research* 97.E10, p. 15923. DOI: 10.1029/92JE01696.
- Piskorz, D., L. T. Elkins-Tanton, and S. E. Smrekar (2014). “Coronae formation on Venus via extension and lithospheric instability”. *Journal of Geophysical Research: Planets* 119.12, pp. 2568–2582. DOI: 10.1002/2014JE004636.
- Poirier, J.-P. (1994). “Light elements in the Earth’s outer core: A critical review”. *Physics of the Earth and Planetary Interiors* 85.3-4, pp. 319–337. DOI: 10.1016/0031-9201(94)90120-1.
- Pozzo, M. et al. (2012). “Thermal and electrical conductivity of iron at Earth’s core conditions.” *Nature* 485.7398, pp. 355–8. DOI: 10.1038/nature11031.
- Reese, C. C., V. S. Solomatov, and C. P. Orth (2007). “Mechanisms for cessation of magmatic resurfacing on Venus”. *Journal of Geophysical Research* 112.E4, pp. 1–12. DOI: 10.1029/2006JE002782.
- Reese, C., V. Solomatov, and L. Moresi (1999). “Non-Newtonian Stagnant Lid Convection and Magmatic Resurfacing on Venus”. *Icarus* 80, pp. 67–80.
- Romeo, I. (2013). “Monte Carlo models of the interaction between impact cratering and volcanic resurfacing on Venus: The effect of the Beta-Atla-Themis anomaly”. *Planetary and Space Science* 87, pp. 157–172. DOI: 10.1016/j.pss.2013.07.010.

- Rose, I. R. and J. Korenaga (2011). “Mantle rheology and the scaling of bending dissipation in plate tectonics”. *Journal of Geophysical Research* 116.B6, B06404. DOI: 10.1029/2010JB008004.
- Rubie, D. C., D. J. Frost, et al. (2011). “Heterogeneous accretion, composition and core–mantle differentiation of the Earth”. *Earth and Planetary Science Letters* 301.1-2, pp. 31–42. DOI: 10.1016/j.epsl.2010.11.030.
- Rubie, D. C., S. Jacobson, et al. (2015). “Accretion and differentiation of the terrestrial planets with implications for the compositions of early-formed Solar System bodies and accretion of water”. *Icarus* 248, pp. 89–108. DOI: 10.1016/j.icarus.2014.10.015.
- Sandwell, D. T. and G. Schubert (1992). “Flexural ridges, trenches, and outer rises around coronae on Venus”. *Journal of Geophysical Research* 97.E10, p. 16069. DOI: 10.1029/92JE01274.
- Saunders, R. S. et al. (1992). “Magellan mission summary”. *Journal of Geophysical Research* 97.E8, p. 13067. DOI: 10.1029/92JE01397.
- Schaber, G. G. et al. (1992). “Geology and distribution of impact craters on Venus: What are they telling us?” *Journal of Geophysical Research* 97.E8, p. 13257. DOI: 10.1029/92JE01246.
- Schubert, G. (1994). “Gravity over Coronae and Chasmata on Venus”. *Icarus* 112.1, pp. 130–146. DOI: 10.1006/icar.1994.1174.
- Schubert, G., D. L. Turcotte, and P. Olson (2001). *Mantle Convection in the Earth and Planets*. New York: Cambridge University Press.
- Schultz, P. H. and P. D. Spudis (1983). “Beginning and end of lunar mare volcanism”. *Nature* 302.5905, pp. 233–236. DOI: 10.1038/302233a0.
- Scott, D. and C. Tout (1989). “Nearest neighbour analysis of random distributions on a sphere”. *Monthly Notices of the Royal Astronomical Society* 241, pp. 109–117.
- Seagle, C. T. et al. (2013). “Electrical and thermal transport properties of iron and iron-silicon alloy at high pressure”. *Geophysical Research Letters* 40.20, pp. 5377–5381. DOI: 10.1002/2013GL057930.
- Shaw, D. M. (1970). “Trace element fractionation during anatexis”. *Geochimica et Cosmochimica Acta* 34, pp. 237–243. DOI: 10.1016/0016-7037(70)90009-8.
- Shi, C. Y. et al. (2013). “Formation of an interconnected network of iron melt at Earth’s lower mantle conditions”. *Nature Geoscience* 6.11, pp. 971–975. DOI: 10.1038/ngeo1956.
- Siebert, J. et al. (2013). “Terrestrial accretion under oxidizing conditions.” *Science* 339.6124, pp. 1194–7. DOI: 10.1126/science.1227923.

- Simons, M., S. C. Solomon, and B. H. Hager (1997). "Localization of gravity and topography: constraints on the tectonics and mantle dynamics of Venus". *Geophysical Journal International* 131.1, pp. 24–44. doi: 10.1111/j.1365-246X.1997.tb00593.x.
- Sivia, D. S. (1996). *Data Analysis: A Bayesian Tutorial*. Second. New York: Oxford University Press.
- Sleep, N. H. (1979). "Thermal History and Degassing of the Earth: Some Simple Calculations". *The Journal of Geology* 87, pp. 671–686. doi: 10.1086/628459.
- Smirnov, A. V. et al. (2016). "Palaeointensity, core thermal conductivity and the unknown age of the inner core". *Geophysical Journal International* 205.2, pp. 1190–1195. doi: 10.1093/gji/ggw080.
- Smrekar, S. (1994). "Evidence for Active Hotspots on Venus from Analysis of Magellan Gravity Data". *Icarus* 112.1, pp. 2–26. doi: 10.1006/icar.1994.1166.
- Smrekar, S. E., R. Comstock, and F. S. Anderson (2003). "A gravity survey of Type 2 coronae on Venus". *Journal of Geophysical Research* 108.E8, p. 5090. doi: 10.1029/2002JE001935.
- Smrekar, S. E. and S. C. Solomon (1992). "Gravitational spreading of high terrain in Ishtar Terra, Venus". *Journal of Geophysical Research: Planets* 97.E10, pp. 16121–16148. doi: 10.1029/92JE01315.
- Smrekar, S. E. and C. Sotin (2012). "Constraints on mantle plumes on Venus: Implications for volatile history". *Icarus* 217.2, pp. 510–523. doi: 10.1016/j.icarus.2011.09.011.
- Smrekar, S. E. and E. R. Stofan (1997). "Corona Formation and Heat Loss on Venus by Coupled Upwelling and Delamination". *Science* 277.5330, pp. 1289–1294. doi: 10.1126/science.277.5330.1289.
- Smrekar, S. E. and E. R. Stofan (2003). "Effects of lithospheric properties on the formation of Type 2 coronae on Venus". *Journal of Geophysical Research* 108.E8, p. 5091. doi: 10.1029/2002JE001930.
- Smrekar, S. E., E. R. Stofan, et al. (2010). "Recent Hotspot Volcanism on Venus from VIRTIS Emissivity Data". *Science* 328.5978, pp. 605–608. doi: 10.1126/science.1186785.
- Solomatov, V. S. (1995). "Scaling of temperature- and stress-dependent viscosity convection". *Physics of Fluids* 7.2, p. 266. doi: 10.1063/1.868624.
- Solomatov, V. S. (1996). "Can hotter mantle have a larger viscosity?" *Geophysical Research Letters* 23.9, pp. 937–940. doi: 10.1029/96GL00724.
- Solomatov, V. S. and L.-N. Moresi (1996). "Stagnant lid convection on Venus". *Journal of Geophysical Research* 101.E2, pp. 4737–4753. doi: 10.1029/95JE03361.

- Solomatov, V. S. and L.-N. Moresi (2000). “Scaling of time-dependent stagnant lid convection: Application to small-scale convection on Earth and other terrestrial planets”. *Journal of Geophysical Research* 105.B9, pp. 21795–21817. DOI: 10.1029/2000JB900197.
- Solomatov, V. S. and D. J. Stevenson (1993). “Nonfractional crystallization of a terrestrial magma ocean”. *Journal of Geophysical Research* 98.E3, pp. 5391–5406. DOI: 10.1029/92JE02579.
- Solomatov, V. (2007). “Magma Oceans and Primordial Mantle Differentiation”. *Treatise on Geophysics*. Ed. by G. Schubert. Elsevier, pp. 91–119. DOI: 10.1016/B978-044452748-6.00141-3.
- Solomon, S. C. and J. W. Head (1990). “Lithospheric flexure beneath the Freyja Montes Foredeep, Venus: Constraints on lithospheric thermal gradient and heat flow”. *Geophysical Research Letters* 17.9, pp. 1393–1396. DOI: 10.1029/GL017i009p01393.
- Spohn, T. (1991). “Mantle differentiation and thermal evolution of Mars, Mercury, and Venus”. *Icarus* 90.2, pp. 222–236. DOI: 10.1016/0019-1035(91)90103-Z.
- Squyres, S. W. et al. (1993). “The spatial distribution of coronae and related features on Venus”. *Geophysical Research Letters* 20.24, pp. 2965–2968. DOI: 10.1029/93GL00866.
- Stelzer, Z. and A. Jackson (2013). “Extracting scaling laws from numerical dynamo models”. *Geophysical Journal International* 193.3, pp. 1265–1276. DOI: 10.1093/gji/ggt083.
- Stevenson, D. J. (1983). “Anomalous bulk viscosity of two-phase fluids and implications for planetary interiors”. *Journal of Geophysical Research* 88.B3, p. 2445. DOI: 10.1029/JB088iB03p02445.
- Stevenson, D. J. (1987). “Limits on lateral density and velocity variations in the Earth’s outer core”. *Geophysical Journal International* 88.1, pp. 311–319. DOI: 10.1111/j.1365-246X.1987.tb01383.x.
- Stevenson, D. J. (2003). “Planetary magnetic fields”. *Earth and Planetary Science Letters* 208.1-2, pp. 1–11. DOI: 10.1016/S0012-821X(02)01126-3.
- Stevenson, D. J., T. Spohn, and G. Schubert (1983). “Magnetism and thermal evolution of the terrestrial planets”. *Icarus* 54.3, pp. 466–489. DOI: 10.1016/0019-1035(83)90241-5.
- Stofan, E. R., D. L. Bindschadler, et al. (1991). “Corona Structures on Venus - Models of Origin”. *Journal of Geophysical Research: Planets* 96.E4, pp. 20933–20946. DOI: 10.1029/91JE02218.
- Stofan, E., A. Brian, and J. Guest (2005). “Resurfacing styles and rates on Venus: assessment of 18 venusian quadrangles”. *Icarus* 173.2, pp. 312–321. DOI: 10.1016/j.icarus.2004.08.004.

- Stofan, E. R., V. L. Sharpton, et al. (1992). “Global distribution and characteristics of coronae and related features on Venus: Implications for origin and relation to mantle processes”. *Journal of Geophysical Research* 97.E8, p. 13347. doi: 10.1029/92JE01314.
- Stofan, E. R., S. E. Smrekar, D. L. Bindschandler, et al. (1995). “Large Topographic Rises on Venus: Implications for Mantle Upwelling”. *Journal of Geophysical Research* 100.95, pp. 317–327. doi: 10.1029/95JE01834.
- Stofan, E. R., S. E. Smrekar, S. W. Tapper, et al. (2001). “Preliminary analysis of an expanded corona database for Venus”. *Geophysical Research Letters* 28.22, pp. 4267–4270. doi: 10.1029/2001GL013307.
- Strom, R., G. Schaber, and D. Dawson (1994). “The global resurfacing of Venus”. *Journal of Geophysical Research* 99.E5, pp. 10899–10926. doi: 10.1029/94JE00388.
- Tackley, P. J. and D. J. Stevenson (1991). “The production of small venusian coronae by Rayleigh–Taylor instabilities in the uppermost mantle”. *Eos Trans. Am. Geophys. Union* 72, p. 287.
- Tajika, E. and T. Matsui (1993). “Evolution of Seafloor Spreading Rate Based on 40-Ar Degassing History”. *Geophysical Research Letters* 20.9, pp. 851–854. doi: 10.1029/93GL00731.
- Takafuji, N. et al. (2005). “Solubilities of O and Si in liquid iron in equilibrium with (Mg,Fe)SiO₃ perovskite and the light elements in the core”. *Geophysical Research Letters* 32.6, p. L06313. doi: 10.1029/2005GL022773.
- Tang, X. et al. (2014). “The thermal conductivity of Earth’s lower mantle”. *Geophysical Research Letters* 41.8, pp. 2746–2752. doi: 10.1002/2014GL059385.
- Tarduno, J. A., R. D. Cottrell, W. J. Davis, et al. (2015). “A Hadean to Paleoproterozoic geodynamo recorded by single zircon crystals”. *Science* 349.6247, pp. 521–524. doi: 10.1126/science.aaa9114.
- Tarduno, J. A., R. D. Cottrell, M. K. Watkeys, et al. (2010). “Geodynamo, solar wind, and magnetopause 3.4 to 3.45 billion years ago.” *Science* 327.5970, pp. 1238–40. doi: 10.1126/science.1183445.
- Treiman, A. H. (2007). “Geochemistry of Venus’ Surface: Current Limitations as Future Opportunities”. *Exploring Venus as a Terrestrial Planet*. Ed. by L. W. Esposito, E. R. Stofan, and T. E. Cravens. Washington, DC: American Geophysical Union, pp. 7–22.
- Turcotte, D. L. (1993). “An Episodic Hypothesis for Venusian Tectonics”. *Journal of Geophysical Research* 98.E9, pp. 17061–17068. doi: 10.1029/93JE01775.
- Turcotte, D. L. and G. Schubert (2002). *Geodynamics*. New York: Cambridge University Press.

- Wade, J. and B. J. Wood (2005). "Core formation and the oxidation state of the Earth". *Earth and Planetary Science Letters* 236.1-2, pp. 78–95. DOI: 10.1016/j.epsl.2005.05.017.
- Wahl, S. M. and B. Militzer (2015). "High-temperature miscibility of iron and rock during terrestrial planet formation". *Earth and Planetary Science Letters* 410, pp. 25–33. DOI: 10.1016/j.epsl.2014.11.014.
- Watson, E. B., J. B. Thomas, and D. J. Cherniak (2007). "40Ar retention in the terrestrial planets." *Nature* 449.7160, pp. 299–304. DOI: 10.1038/nature06144.
- Weiss, B. P. et al. (2015). "Pervasive remagnetization of detrital zircon host rocks in the Jack Hills, Western Australia and implications for records of the early geodynamo". *Earth and Planetary Science Letters* 430, pp. 115–128. DOI: 10.1016/j.epsl.2015.07.067.
- Weizman, A. et al. (2001). "Modeling the Volcanism on Mars". *Icarus* 150.2, pp. 195–205. DOI: 10.1006/icar.2000.6572.
- White, S. M., J. A. Crisp, and F. J. Spera (2006). "Long-term volumetric eruption rates and magma budgets". *Geochemistry Geophysics Geosystems* 7.3, Q03010. DOI: 10.1029/2005GC001002.
- Wichman, R. W. (1999). "Internal crater modification on Venus: Recognizing crater-centered volcanism by changes in floor morphometry and floor brightness". *Journal of Geophysical Research* 104.E9, pp. 21957–21977. DOI: 10.1029/1997JE000428.
- Wolf, D. (1984). "On the relation between two-dimensional and axisymmetric loads in plate flexure problem". *Journal of Geophysics* 54, pp. 232–235. DOI: 10.18419/opus-7120.
- Wood, B. J., M. J. Walter, and J. Wade (2006). "Accretion of the Earth and segregation of its core." *Nature* 441.7095, pp. 825–33. DOI: 10.1038/nature04763.
- Xie, S. and P. J. Tackley (2004). "Evolution of helium and argon isotopes in a convecting mantle". *Physics of the Earth and Planetary Interiors* 146.3-4, pp. 417–439. DOI: 10.1016/j.pepi.2004.04.003.
- Yamazaki, D. and S.-i. Karato (2001). "Some mineral physics constraints on the rheology and geothermal structure of Earth's lower mantle". *American Mineralogist* 86.4, pp. 385–391. DOI: 10.2138/am-2001-0401.
- Zahn, U. von et al. (1983). "Composition of the Venus atmosphere". *Venus*. Ed. by D. M. Hunten et al. Tucson: Univ. of Arizona Press, pp. 299–430.
- Zhang, P., R. E. Cohen, and K. Haule (2015). "Effects of electron correlations on transport properties of iron at Earth's core conditions". *Nature* 517.7536, pp. 605–607. DOI: 10.1038/nature14090.